Advanced techniques for Fourier-transform absorption spectroscopy

Santeri Larnimaa

University of Helsinki
Faculty of Science
Department of Chemistry
A.I. Virtasen aukio 1 (P.O. Box 55)
FI-00014 University of Helsinki
Finland

Doctoral dissertation, to be presented for public discussion with the permission of the Faculty of Science of the University of Helsinki, in Auditorium A129, Department of Chemistry (A.I. Virtasen aukio 1, Helsinki), on the 7th of August, 2025 at 12 o'clock.

Advanced techniques for Fourier-transform absorption spectroscopy

Santeri Larnimaa

University of Helsinki
Faculty of Science
Department of Chemistry
A.I. Virtasen aukio 1 (P.O. Box 55)
FI-00014 University of Helsinki
Finland

Doctoral dissertation, to be presented for public discussion with the permission of the Faculty of Science of the University of Helsinki, in Auditorium A129, Department of Chemistry (A.I. Virtasen aukio 1, Helsinki), on the 7th of August, 2025 at 12 o'clock.

Advanced techniques for Fourier-transform absorption spectroscopy

Santeri Larnimaa

University of Helsinki
Faculty of Science
Department of Chemistry
A.I. Virtasen aukio 1 (P.O. Box 55)
FI-00014 University of Helsinki
Finland

Doctoral dissertation, to be presented for public discussion with the permission of the Faculty of Science of the University of Helsinki, in Auditorium A129, Department of Chemistry (A.I. Virtasen aukio 1, Helsinki), on the 7th of August, 2025 at 12 o'clock.

Supervisors

Prof. Markku Vainio
Department of Chemistry
University of Helsinki
Helsinki, Finland

Dr. Markus Metsälä
Department of Chemistry
University of Helsinki
Helsinki, Finland

Reviewers

Prof. Aleksandra Foltynowicz Matyba
Department of Physics
Umeå University
Umeå, Sweden

Prof. Matti Kaivola
Department of Applied Physics
Aalto University
Espoo, Finland

Opponent

Prof. Takuro Ideguchi
Institute for Photon Science and Technology, and Department of Physics
Graduate School of Science
The University of Tokyo
Tokyo, Japan

Doctoral Programme in Chemistry and Molecular Sciences

Publisher: University of Helsinki
Series: Dissertationes Universitatis Helsingiensis 254/2025

ISBN 978-952-84-1107-9 (print)
ISBN 978-952-84-1106-2 (online)
ISSN 2954-2898 (print)
ISSN 2954-2952 (online)
PunaMusta, Joensuu 2025

Abstract

Fourier-transform spectroscopy (FTS) is an optical technique that can be used to interrogate a sample to detect and quantify its molecular constituents. In its most traditional form, the FTS instrument consists of a simple optical delay line, using which an incident incoherent broadband light beam is made to interfere with itself, allowing one to record a time-domain representation of the optical field. The Fourier transform of this so-called interferogram results in the corresponding optical spectrum that reveals the absorption by the sample placed in the way of the optical beam.

While Fourier-transform spectroscopy instruments based on this simple Michelson interferometer scheme were developed to a mature level already during the previous century, and while they are still widely used throughout academia and industry, the technique suffers from certain drawbacks in certain advanced applications. For example, achieving high resolution required for the accurate analysis of the absorption spectra of gaseous samples results in long delay arms and limited measurement speeds.

This thesis addresses these drawbacks and offers new contributions to FTS research by developing advanced instrumentation, or by using traditional FTS to advance other sub-fields of spectroscopy. For example, I have used a commercial high-resolution FTS instrument to measure, for the first time, the fundamental and first overtone rovibrational absorption bands of the radioactive $H^{36}Cl$ molecule. The analysis of these absorption spectra revealed the absorption line wavenumbers, information that is crucial for future applications that may target the detection of this molecule from nuclear facilities or nuclear waste.

Following the aforementioned work that acknowledges the ever-continuing relevance of traditional FTS, the other works included in this thesis explore modern FTS approaches and their benefits. For example, I have studied a relatively new modality of FTS called phase-controlled Fourier-transform spectroscopy and its compatibility with gas-phase (cantilever-enhanced) photoacoustic spectroscopy to improve the measurement speed of said sensitive photoacoustic technique in broadband measurements.

Further still, this thesis work contributes to dual-comb spectroscopy (DCS), an FTS technique that does not require any mechanical scanning parts but that achieves incredibly fast measurements with practically unlimited resolution. In recent years, vast research efforts have been dedicated towards DCS to mature the technique to become the current state of the art. Our contribution was to demonstrate a simple approach to DCS where stable measurements can be restored using a numerical post-correction algorithm that I developed.

Finally, this thesis proposes a completely new approach to FTS. Instead of linear motion, the proposed rotational-Doppler FTS technique utilizes rotational motion and light that carries orbital angular momentum (OAM). As a consequence, RD-FTS offers fast, high-resolution measurements while keeping the experimental setup compact.

Preface

When the teaching of physics and chemistry started in the fifth grade in the elementary school, the two subjects immediately became my favourite ones, in addition to maths that had started already a few years earlier. I still remember one beginning-of-chapter illustration about atoms in one of the school books, where some surface was depicted to comprise these billiard ball-looking things that formed a kind of lattice. I was fascinated – imagine that every-day objects like the desk where I was reading that very book could be conceptualized to consist of these entities called atoms. It felt like a real-life fantasy, where one can glance behind the shroud of every-day life with the help of science.

When I finished my matriculation exams in high-school (with of course excellent grades in all three subjects), I only knew that I wanted to continue my studies at the Kumpula Campus of the University of Helsinki, which is dedicated to the natural sciences. I chose Chemistry, basically at random with the idea that once there, I could mix and match my studies from all three disciplines. This was the right choice. Because, during the very first study years in the Chemistry Department, we were to take the two famous (but also notorious) physical chemistry courses: "Thermodynamics and Dynamics" and "Molecular Structure and Spectroscopy". In particular, the latter course brought back the fascination I had felt about atoms and molecules in the fifth grade, but, this time, instead of billiard balls, we were introduced with the perhaps unintuitive at first but with the even more fascinating mathematical concepts of Quantum Mechanics that describe the structure of atoms and molecules. Long story short, I later managed to secure my first summer job in a laser lab on the 4th floor of the Chemistry Department, which is dedicated to physical chemistry and molecular sciences. There, I have had the pleasure to study molecules, with, of course, the feeling of real-life fantasy strengthened by the fact that I also get to play around with lasers.

Even though aligning a laser beam through some experimental setup hours on end can be dull work at times, what I like about experimental work is its hands-on nature. I construct experimental setups with my own hands and, while doing so, I can conceptualize what I am actually doing by using science; all experimental setups are, after all, based on, or need to be designed according to some underlying theory. One anecdote of this is when I worked as a Master's student with the optical parametric oscillator light source that led to my first publication: I spent embarrassingly many days aligning the resonator trying to get the OPO to start. I had made my calculations and designed the resonator, but it simply didn't light up. Finally I realised that both of the surfaces of the resonator input mirror were curved after all, which should have been considered in the calculations. After moving the crystal focusing lens by the required amount, and after some realignment, the OPO finally lit up with dazzlingly bright red colours, the second harmonic of the generated near-infrared light beam.

Regarding spectroscopy, what I also like about my work is how much one learns while doing it. Because my research is mostly related to method development, I construct the experimental setups myself from scratch, in other words, the experimental setup is no black box. After working months with the setup, after the setup has been aligned, the sample cell put into place, the gas exchange system designed and after

writing computer scripts to automize the measurement (laser wavelength scanning, laser power and wavelength measurement, signal digitization, gas exchange, *etc.*), it is always gratifying to finally start the measurement and to actually see the absorption peak emerging in the measured signal, apart from the times when it doesn't but when the measurement exhibits only noise. When this happens, one needs to take a step back, go back to the drawing board and come up with some new approach or test to solve the new problem.

Finally, as a researcher, it is exciting to demonstrate something that no one else has ever done before. Less ambitiously, my goal as a researcher is simply to contribute. If not something amazingly groundbreaking, then at least something small. If my work manages to inspire or spark some kind of a new idea for some other researcher who has for some reason or other ended up reading my paper whatever their specific research field may be, I have done my job. After all, I believe that it is through the cumulation of small contributions over years or decades that one can then in due time realize that science has, overall, made another giant leap forward.

The first person I want to acknowledge is Matias Jääskeläinen. He worked as a course assistant and helped me on many courses I attended as a Bachelor student. It was he who suggested, both to me and Dr. Markus Metsälä that what if I became a course assistant myself (to help with the said physical chemistry courses). Without this suggestion I very probably wouldn't be writing the current thesis. Thanks to Matias, I actually ended up working as a course assistant on said courses for many years with the pleasure to teach and to help other students that tried to crack the homework problems, to which I had written the model answers myself. This also led me to manage to secure my first summer job in a laser lab under the supervision of Markus Metsälä when I was a second-year Bachelor student in 2018. Thank you Markus for this opportunity. During that summer, I worked with cavity ring-down spectroscopy and learned the basics of experimental work in a laser lab, got routine in aligning lasers and also took up Matlab, a hugely useful programming platform for data analysis, numerical simulations and writing measurement programs, which programming platform is nowadays an integral part of my every-day work. I am also pleased that I got to work with cavity-ring down and am proud that I have aligned such a cavity myself. This is because cavity-ring down is one of the most sensitive spectroscopic techniques available in addition to photoacoustics, the latter technique being immensely important for this thesis. This makes it useful to have personal experience on both techniques.

I also want to thank Dr. Juho Karhu. He helped me a lot during summer 2019 when I worked as a Master's student and on the radiocarbon methane project that led to the publication of the first article included in this thesis. You always have fresh ideas and are prepared to help me in the lab. Thank you for that.

Then, as a whole, I want to thank the entirety of our research group and the persons who have worked there during all or any of these years. I think we have an incredibly friendly and supportive atmosphere on the 4th floor. I also want to thank Mikhail Roiz, an incredibly competent colleague of mine. Your enthusiasm and expertise in laser physics have definitely inspired and helped me during the last few years. We have always had fruitful discussions on whatever project either of us has been working on.

Finally, but most importantly, I want to thank Prof. Markku Vainio, my supervisor during all these years and this thesis work. Thank you so much for your help, support and endless understanding. You have given me the opportunity for truly independent work but you have also always made time to help me with whatever problem I may have had in the lab or otherwise.

Helsinki, September 2024

Santeri Larnimaa

Publications

Below is a list of publications (Articles I–V) included in this thesis, with brief descriptions and with my contributions to them. Note that Article I does not employ Fourier-transform spectroscopy, for which reason that article is only briefly discussed in this thesis as a means to give the reader a wider view about the different aspects of spectroscopy.

I **Santeri Larnimaa**, Lauri Halonen, Juho Karhu, Teemu Tomberg, Markus Metsälä, Guillaume Genoud, Tuomas Hieta, Steven Bell, and Markku Vainio, "High-resolution analysis of the ν_3 band of radiocarbon methane $^{14}CH_4$," *Chemical Physics Letters* **750** (2020), 137488, doi:10.1016/j.cplett.2020.137488.

Description: The fundamental asymmetrical stretching rovibrational absorption band of $^{14}CH_4$ was measured with high resolution using a high-power, continuous-wave optical parametric oscillator light source combined with wavelength modulation and photoacoustic detection. The absorption line wavenumbers were determined and a band fit analysis was performed.

Contribution: I constructed the experimental setup, performed the measurements, analysed the data (not including the band fit analysis), prepared most of the figures, and participated in reviewing the manuscript.

II **Santeri Larnimaa**, Markku Vainio, and Ville Ulvila, "Infrared spectroscopy of radioactive hydrogen chloride $H^{36}Cl$," *Journal of Quantitative Spectroscopy and Radiative Transfer* **277** (2022), 107984, doi:10.1016/j.jqsrt.2021.107984.

Description: The fundamental and first overtone rovibrational absorption bands of $H^{36}Cl$ were measured for the first time, by using a high-resolution Fourier-transform spectroscopy instrument. Band fit analysis was performed to retrieve the molecular constants.

Contribution: I performed the measurements together with Ville Ulvila. I analysed the data, wrote the manuscript and participated in reviewing it.

III **Santeri Larnimaa**, Mikhail Roiz, and Markku Vainio, "Photoacoustic phase-controlled Fourier-transform infrared spectroscopy," *Optics Continuum* **2** (2023) 3, 564–578, doi:10.1364/OPTCON.483779.

Description: We demonstrated a 13-fold speed improvement in broadband cantilever-enhanced photoacoustic spectroscopy by combining the technique with phase-controlled Fourier-transform spectroscopy. For proof of concept, we measured the P-branch of the fundamental asymmetrical rovibrational absorption band of methane in the mid-infrared wavelength region. We performed a detailed analysis on the benefits and drawbacks of the CEPAS-PC-FTS technique.

Contribution: I constructed the experimental setup (not including the mid-infrared optical frequency comb used as the light source), performed the measurements, analysed the data, wrote the manuscript and participated in reviewing it.

IV Mikhail Roiz, **Santeri Larnimaa**, Touko Uotila, Mikko Närhi, and Markku Vainio, "Reference-free dual-comb spectroscopy with inbuilt coherence," *Optics Letters* **49** (2024) 9, 2473–2476, doi:10.1364/OL.521866.

Description: We presented a simple dual-comb spectroscopy instrument for fast, high-resolution gas-phase spectroscopy. The system exhibits inherent phase stability with only minor fluctuations in the interferogram phase that can be post-corrected together with the interferogram timing jitter using a simple numerical algorithm. The performance of the system was tested by measuring gaseous acetylene in the near-infrared (telecom) wavelength region.

Contribution: I participated in the measurements, developed the data acquisition and data processing schemes, analysed most of the data, wrote the part concerning the numerical correction algorithm in the manuscript supplementary document, and participated in reviewing the manuscript.

V **Santeri Larnimaa**, and Markku Vainio, "Fourier-transform spectroscopy based on the rotational Doppler effect," *AIP Advances* **14** (2024) 10, 105329, doi:10.1063/5.0220119.

Description: A novel Fourier-transform spectroscopy technique based on the rotational Doppler effect and on an optical frequency comb light source whose frequency components carry distinct amounts of orbital angular momentum was proposed. The technique offers fast, mode-resolved measurements without the need for long mechanical scan arms. A proof-of-concept measurement using an emulated optical vortex comb light source was performed at the 1 µm wavelength region by measuring gaseous acetylene with photoacoustic detection.

Contribution: I participated in conceiving the idea, constructed the experimental setup, performed the measurements, analysed the data, wrote the manuscript and participated in reviewing it.

Acronyms

CEPAS	Cantilever-enhanced photoacoustic spectroscopy
CRDS	Cavity ring-down spectroscopy
CW	Continuous-wave (laser)
DAQ	Data acquisition (card)
DCS	Dual-comb spectroscopy
FOM	Figure of merit
FT	Fourier transform
FTIR	Fourier-transform infrared spectroscopy
FTS	Fourier-transform spectroscopy
FWHM	Full-width-at-half-maximum
HITRAN	High-resolution transmission molecular absorption database
HWHM	Half-width-at-half-maximum
ILS	Instrument lineshape function
LG	Laguerre–Gaussian
NICE-OHMS	Noise-immune cavity-enhanced optical heterodyne molecular spectroscopy
OAM	Orbital angular momentum
OFC	Optical frequency comb
OPO	Optical parametric oscillator
PAS	Photoacoustic spectroscopy
PC-FTS	Phase-controlled Fourier-transform spectroscopy
PPLN	Periodically-poled lithium niobate
QEPAS	Quartz-enhanced photoacoustic spectroscopy
RD-FTS	Rotational-Doppler Fourier-transform spectroscopy
RDE	Rotational Doppler effect
SCAR	Saturated-absorption cavity ring-down spectroscopy
SNR	Signal-to-noise ratio
SPP	Spiral phase plate
WMAS	Wavelength-modulation absorption spectroscopy

Contents

Introduction

Spectroscopy utilizes electromagnetic radiation (light) to study many kinds of matter. By measuring the absorption spectrum of a sample, one can determine its constituents, their amounts but also the structure of the constituent molecules (or atoms) themselves. This thesis focuses on gas-phase molecular absorption spectroscopy, the applications of which are various. For example, spectroscopy can be used for greenhouse gas and atmospheric composition monitoring,[1,2] remote sensing of volcano eruptions,[3] air-quality measurements,[4,5] detection of compounds in space,[6,7] breath analysis,[8] and for many other applications.[9–12]

The most sensitive spectroscopic approaches typically utilize tunable single frequency light sources.[13] While successful, these approaches usually suffer from limited wavelength tunability, which in turn limits the measurements to the detection of only a few, if not only a single absorption line, potentially disallowing multi-species detection. In contrast, spectroscopic techniques based on broadband light sources allow for the measurement of a wide optical bandwidth in a single measurement and therefore the simultaneous measurement of absorption features belonging to multiple different molecules.[14–17]

One such broadband spectroscopic approach is Fourier-transform spectroscopy (FTS), a technique based on a simple interferometric device that records the time-domain representation (interferogram) of the optical field such that the Fourier transform of the interferogram reveals the corresponding optical spectrum. While the technique was invented already during the previous century, its success seems never-ending. Furthermore, FTS research enjoys renewed interest due to the more recent invention of several advanced Fourier-transform spectroscopy approaches.

This thesis studies several of such advanced FTS techniques. While in Article II we used traditional FTS to measure and analyse the absorption spectrum of the $H^{36}Cl$ molecule that has not been previously studied spectroscopically, Articles III–V investigate advanced FTS techniques to improve the measurement speed and/or spectral resolution of broadband spectroscopic measurements. In addition to the increased measurement speed being convenient for the person conducting the measurements, increased measurement speed can allow accurate measurements of short-lived species or monitoring of fast processes such as chemical reactions.[10,18,19] With regards to the improved spectral resolution, it allows accurate production of spectroscopic data[20] but it also assists in resolving close-lying absorption features to allow more accurate, say, multi-species detection.[14–17]

In Article III, we investigated the possibility of combining the so-called phase-controlled FTS technique (a special modality of FTS)[21,22] with cantilever-enhanced photoacoustic spectroscopy (CEPAS).[23] CEPAS is a highly-sensitive detection technique but it has, until now, suffered from unreasonably slow measurements when combined with FTS.[24] However, improving the measurement speed by using the PC-FTS approach is a trade-off with increased experimental complexity and limited spectral resolution, which issues are discussed at length in this thesis.

In Article IV we contributed to dual-comb spectroscopy (DCS), which is the current state-of-the-art form of FTS that allows fast and high-resolution measurements without any mechanical scanning parts.[25] The novelty of our contribution is the

utilization of special infrared optical frequency comb light sources developed in our lab[26] such that experimentally simple but stable (mutually coherent) measurements are ensured with only minor post-corrections required by using a numerical algorithm I developed.

Finally, Article V proposes a completely new Fourier-transform spectroscopy approach that is based on the rotational Doppler effect[27] (in contrast to traditional FTS that utilizes the linear Doppler effect) and on a special "vortex comb" light source whose frequency components carry different amounts of orbital angular momentum (OAM). This new spectroscopic approach promises fast and high-resolution measurements but achieves these with a more compact experimental setup than traditional FTS would allow. Because the proposed "rotational-Doppler FTS" technique is completely new, more research on the topic is required. In this thesis, I analyse the feasibility of the proposed spectroscopic technique and identify key issues that require future research.

This thesis is organized as follows. Although the main topic of this thesis is Fourier-transform spectroscopy, Section 1 discusses spectroscopy in a more general sense. It is targeted to readers (mostly) unfamiliar with spectroscopy and it illustrates different aspects of spectroscopy, from applications to more theoretical considerations and, in particular, to instrumentation. Examples are mostly drawn from tunable single frequency laser spectroscopy, such as from Article I where I used a tunable mid-infrared light source to record high-resolution spectra belonging to the radioactive $^{14}CH_4$ molecule. These measurements provided new, high-quality spectroscopic information that allowed a more rigorous rovibrational analysis of the molecule than before.

Starting from Section 2, the rest of this thesis considers Fourier-transform spectroscopy, with Section 2 presenting the basic principles of the technique while giving emphasis on selected details such as resolution, photoacoustic detection, phase correction and light sources. The section culminates in a summary of Article II that demonstrates the use of traditional Fourier-transform spectroscopy to study the absorption spectrum of $H^{36}Cl$. The following sections (Sections 3–5) then summarize the results from the three remaining articles that demonstrate novel modalities and their benefits to Fourier-transform spectroscopy. Instead of only summarizing the results, I have taken the opportunity to use this space to complete the discussion in the articles by presenting supporting details, simulations and decision making that lead to the final results presented in the articles. Much of this additional discussion is found as Appendices to this thesis.

Particular emphasis is given on the rotational-Doppler spectroscopy work (Article V; Section 5). This is because I find the topic most interesting and the proposed technique most novel. To that end, a longer review about the origin of the rotational Doppler effect and about common detection techniques is given. In addition, I study the practical limits of the technique in terms of the modulation signal strengths, the rotating target selection and problems with crosstalk.

A final but an important aspect I want to exhibit in this thesis is the usefulness of numerical simulations. In experiments, one typically has many variables that may affect the results in varying and often unknown degrees. In particular, Fourier-transform spectroscopy relies heavily on data processing as the absorption spectrum is obtained indirectly via measuring and Fourier-transforming the interferogram. This demands

confidence on the part of the data processor to claim that the operations performed on the data are justified. Once the results are obtained, they also need to be understood. Fortunately, these can be easily tested by setting up, if you will, a synthetic lab using some programming platform such as Matlab or Python. Indeed, a large portion of my working hours has been spent on writing Matlab code to test and to learn about different details underlying the experiments. It is most illuminating to see with one's own eyes how changing the value of some parameter affects the results. The reader of this thesis will then find many illustrations but also animations that support the discussion. The animations can be viewed by reading a downloaded copy of this thesis with a suitable PDF reader and by clicking on the animations.

1 Molecular absorption spectroscopy

Spectroscopy studies the interaction between light and matter. One can study how light is absorbed, emitted or (inelastically) scattered by atoms and molecules. In all of these interactions, the light field and the molecules (or atoms) exchange energy. For example, in the case of absorption, when a molecule encounters a photon, it may absorb it if the energy of the photon (which is proportional to the optical frequency) matches the energy difference between two suitable energy states of the molecule. Depending on the optical frequency, the absorption may then induce a change in the rotational, vibrational or electronic state of the molecule, or in all of these. In this thesis, all the measurements performed are related to the so-called rovibrational transitions of molecules. What this means is that the optical frequency of the light source used is tuned to excite some vibrational motion of the molecule. However, due to spectroscopic selection rules, the change in the vibrational state is usually accompanied by a change in the rotational state as well. The many selection rules in spectroscopy imply that only certain molecular transitions can be observed via coupling of the external electric field (light) to the molecule. The specific selection rule referred to here is intuitively understood by noting that photons carry angular momentum (they have spin), which means that the absorption of the photon needs to result in a change of the rotational state of the molecule to conserve the total angular momentum.*

The so-called fundamental rovibrational transitions of molecules typically lie in the mid-infrared optical region. For example, the fundamental rovibrational absorption band of HCl measured in Article II is located at the 3.5 µm (2885 cm^{-1}; 86.5 THz) region.† What "fundamental" here means is that the absorbed photon excites the molecule from the ground state (vibrationally still molecule apart from the quantum mechanical effect called the zero-point energy) to the first excited vibrational state. Also the so-called overtone transitions can be measured, which means that if the energy of the photon is, for example, approximately twice the energy of the fundamental transition, the absorption can excite the vibrational motion by two quanta, which is called the first overtone transition. These transitions are typically orders of magnitude weaker than the fundamental ones, but still often appealing for a laser spectroscopist to target as laser and optical component technology is much more mature in the near-infrared, particularly in the 1.5 µm telecom region. For more complex molecules than the diatomic HCl, even more complex vibrational motions than a simple stretching of a single bond are available. For example, in Article IV we measured the so-called $\nu_1 + \nu_3$ combination band of gaseous acetylene. Figure 1 illustrates different vibrational motions probed in this thesis work; Table 1 lists the corresponding wavelengths and the relative absorption strengths of these rovibrational absorption bands.

*Unless the molecule offers some other mechanism for the angular momentum to be conserved, *i.e.*, if it offers some other place to put the extra angular momentum.

†A laser scientist may prefer to use the *wavelength*, λ, to describe a light field. A convention in spectroscopy is to prefer the *wavenumber*, $\tilde{\nu}$ (in units of cm^{-1}), which is the inverse of the wavelength. In this thesis I mostly prefer the optical *frequency*, ν, which is obtained from the wavenumber by multiplying by the speed of light c. Finally, the energy of the photon would be obtained by multiplying the optical frequency by the Planck's constant h.

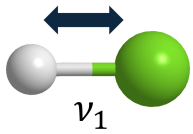

(a) The HCl molecule and its only possible vibrational movement (labelled here with ν_1) probed in Article II.

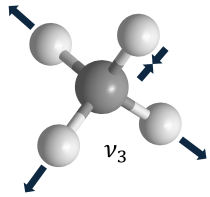

(b) The asymmetric CH-stretching of methane probed in Articles I and III.

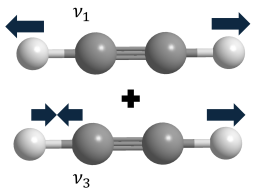

(c) The symmetric (ν_1) and the asymmetric (ν_3) CH-stretches of acetylene were jointly excited in Article IV.

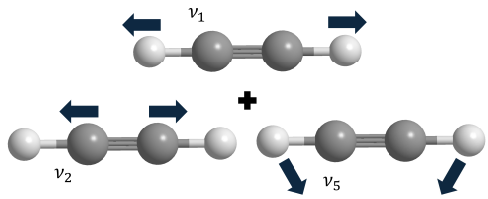

(d) The symmetric (ν_1) CH-stretch, the symmetric CC-stretch (ν_2) and the *cis*-bending mode (ν_5) of acetylene were jointly excited in Article V.

Figure 1: Illustration of the different vibrational modes probed in this thesis work. The ν_i labelling scheme of these so-called normal modes follows the common convention.[28]

Table 1: The molecules and their rovibrational absorption bands measured in this thesis work. For example, $2\nu_1+\nu_2+\nu_5^{l_5}$ means that two quanta of the vibrational mode ν_1 (see Fig. 1), one quantum of ν_2 and one quantum of ν_5 have been jointly excited; the superscript l_5 refers to the so-called vibrational angular momentum related to the degenerate ν_5 bending mode.[29] "Line" refers to the strongest measured absorption line of that band (the symmetry label "A1" and the parity label "e" refer to the lower state), with the following wavelength, wavenumber and optical frequency values referring to that specific transition. S is the line intensity of the transition and S_{rel} the line intensity relative to that of the strongest transition in the table. Thus, the value 2.7×10^6 in the last row means that the transition is over two million times weaker than the one described by the first row. See Table 2 for other information on the transitions.

Molecule	Band	Line	λ (nm)	$\tilde{\nu}$ (cm^{-1})	ν (THz)	S (cm^{-1}/cm^{-2})	S_{rel}
^{1}H^{36}Cl	ν_1	R3	3375.9	2962.140	88.8	6.40×10^{-19}	1.0
^{1}H^{36}Cl	$2\nu_1$	R3	1743.0	5737.113	172.0	1.65×10^{-20}	38.9
^{12}C^{1}H$_4$	ν_3	P4 A1	3356.8	2979.004	89.3	1.227×10^{-19}	5.2
^{12}C$_2$^{1}H$_2$	$\nu_1+\nu_3$	P15 e	1534.1	6518.486	195.4	8.768×10^{-21}	73.1
^{12}C$_2$^{1}H$_2$	$2\nu_1+\nu_2+\nu_5^{l_5}$	R17 e	1063.6	9402.162	281.9	2.379×10^{-25}	2.7×10^6

1.1 Beer–Lambert law

Figure 2 shows the schematic of perhaps the simplest possible absorption spectroscopy experiment to probe molecular transitions: one takes a beam from a single frequency (continuous-wave; CW) laser, shines it through the sample (which is in the context of this thesis always a gas sample), and guides it onto a photodetector. Then one scans the wavelength (optical frequency) of the laser while recording the intensity of the laser beam. If absorption occurs, it is observed as decrease in the laser intensity behind the sample. The absorption through a sample cell of length L is described by the Beer–Lambert law:[30]

$$\frac{I(\nu)}{I_0(\nu)} = \exp(-\alpha(\nu)L) \equiv \mathrm{T}\,, \tag{1.1}$$

where I is the (optical frequency dependent) light intensity with the sample, and I_0 without. $I_0(\nu)$ is referred to as the "background spectrum", and it can be determined by repeating the measurement through the gas cell without the sample, or by fitting some kind of background function, such as a polynomial, to the spectrum measured with the sample, or, more often than not, by combining both of these two approaches.[31]

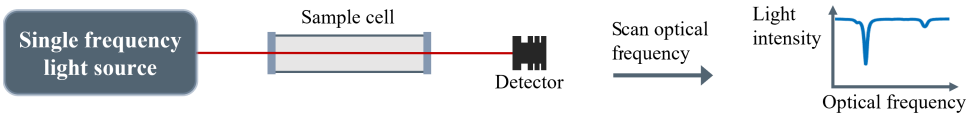

Figure 2: Schematic of perhaps the simplest absorption spectroscopy measurement: the optical frequency of a single-frequency laser is scanned while the light intensity behind the sample is recorded to obtain the transmission spectrum, where sample absorption is seen as dips in the measured light intensity.

The fraction $I(\nu)/I_0(\nu)$ in Equation (1.1) is called the *transmission* (T) and it describes the absorption as a fraction of the light intensity that has not disappeared into the sample. Usually, the measured transmission spectrum is processed into the actual *absorption spectrum*, which is defined in this thesis as the plot of the *absorption coefficient* $\alpha(\nu)$ against the optical frequency (or wavenumber). The absorption coefficient (in units of cm^{-1}) is defined as[32]

$$\alpha(\tilde{\nu}) = Sf(\tilde{\nu})c_V N_{V,\mathrm{tot}}\,, \tag{1.2}$$

where S is the *line intensity* ($\mathrm{cm}^{-1}/\mathrm{cm}^{-2}$), which is a constant that describes the fundamental absorption strength of a given transition of a given molecule. $N_{V,\mathrm{tot}} = p/(k_\mathrm{B}T)$ is the total number density (cm^{-3}) of the sample molecules (all molecules, including those whose absorption features are not targeted) as described here by the perfect gas law (p is pressure, T temperature and k_B the Boltzmann constant). $c_V = N_V/N_{V,\mathrm{tot}}$ is the concentration (volume mixing ratio) of the molecule of interest (*e.g.*, the number of $^1\mathrm{H}^{36}\mathrm{Cl}$ molecules in an air sample divided by the total number of molecules in the sample). Finally, $f(\tilde{\nu})$ is a function ($1/\mathrm{cm}^{-1}$) that describes the absorption lineshape. It is normalized to one such that the area (cm^{-2}) of a measured absorption line yields:

$$A = \int_{-\infty}^{\infty} \alpha(\tilde{\nu})\mathrm{d}\tilde{\nu} = Sc_V N_{V,\mathrm{tot}} \int_{-\infty}^{\infty} f(\tilde{\nu})\mathrm{d}\tilde{\nu} = Sc_V N_{V,\mathrm{tot}}\,. \tag{1.3}$$

The two main mechanisms that can broaden an absorption line and that are relevant to this thesis are the pressure broadening and the Doppler broadening.[33] The former effect is important at pressures close to the atmospheric pressure (1 atm = 1013.25 mbar) and beyond, and it is due to collisions between the molecules in the sample. This yields a Lorentzian absorption lineshape (see Appendix A1). The latter effect is due to the molecules having a certain velocity distribution at a given temperature (molecules travelling at different velocities experience different incoming light frequencies due to the Doppler effect) and it yields a Gaussian lineshape. A lineshape function often used to include both effects is the Voigt profile,[34,35] which is the convolution of the two above absorption lineshape functions. In this thesis, I use the Voigt profile in almost all the works to fit the measured absorption lines (in Article II, I assumed a Lorentzian lineshape).

It should be noted that there are also more complex absorption lineshape functions that include more effects, or that address certain assumptions made when deriving the previously mentioned absorption lineshapes. In fact, it is currently recommended[36] that spectroscopists should use the Hartmann–Tran profile,[37] a lineshape model that can conveniently consider multiple of the so-called beyond-Voigt effects. However, as these lineshape models include many more fitting parameters, the proper use of them requires one to record a set of absorption spectra measured at different pressures and temperatures, and to use the so-called multispectral fitting approach.[38] In addition, the inclusion of the beyond-Voigt effects usually require high signal-to-noise ratios in the measured spectra to see clear systematic structures in the residuals under the fitted absorption lines to inform the data processor that perhaps a beyond-Voigt lineshape should be tried. In [39], the spectral quality requirements for the use of the beyond-Voigt lineshapes are studied in quite some detail. In this thesis, usually only a single spectrum at a given pressure and temperature was recorded, and usually the signal-to-noise ratios were such that the use of only the Voigt profile was justified. In Appendix A1, I present the equations for the absorption lineshape models used in this thesis. Table 2 lists typical values for the pressure and Doppler broadening for the molecules and transitions probed in this thesis work.

Table 2: The measurement conditions, and the pressure and Doppler broadening linewidths (half-width-at-half-maximum) for the transitions in Table 1. All measurements have been performed at approximately room temperature (~296 K) and using a 10 cm long sample cell.

Molecule	$\tilde{\nu}$ (cm^{-1})	p	c_V	γ_{Lor} (GHz)	γ_{Dop} (GHz)
$^{1}H^{36}Cl$	2962.140	1 atm	0.0016	1.88	0.09
$^{1}H^{36}Cl$	5737.113	1 atm	0.0016	2.05	0.17
$^{12}C^{1}H_4$	2979.004	1000 mbar	0.01	1.97	0.14
$^{12}C_2{}^{1}H_2$	6518.486	300 mbar	0.12	0.71	0.24
$^{12}C_2{}^{1}H_2$	9402.162	270 mbar	1.0	1.03	0.34

The Beer-Lambert law (1.1) implies three important aspects of spectroscopy. One is that the absorption spectrum depends on the molecule (via the line intensity S). Indeed, the absorption spectrum of a molecule depends on the structure of that molecule, which means that no absorption spectrum of a molecular species is exactly alike that of some other. This means that by analysing what absorption peaks appear in the measured spectrum, one can perform qualitative analysis on the sample, in other words, one can determine which molecules are present in the sample. On the other hand, because the heights (or areas) of the measured absorption peaks depend on the concentration c_V, one can also perform quantitative analysis on the sample. Finally, by analysing the absorption spectrum, one can also study the molecules themselves. For example, one can extract structural information on them. This is the basis for the more fundamental or theoretical aspect of spectroscopy.

1.2 Spectroscopic models

To see how an absorption spectrum can give information about the structure of the molecule, let's inspect Figure 3, which shows the fundamental rovibrational absorption band of HCl, as measured with a Fourier-transform spectroscopy instrument in Article II. Intriguingly, the spectrum shows clear structure: it consists of two branches of narrow, approximately equidistant lines, and of an empty space between

the branches. A typical exam question in a Bachelor-level course would be to explain why the spectrum looks like it does. A follow-up question could be to calculate the equilibrium bond distance of the HCl molecule based on the spectrum.

To explain the spectrum, we first note that the absorption seems to occur only at specific, well defined optical frequencies. This implies that the energy levels of a molecule are quantized, which brings us to the fact that to explain the spectrum, we require quantum mechanics. Indeed, each line in the spectrum corresponds to a transition between two quantized energy levels of the molecule. In this case, the vibrational quantum number v (that labels the different vibrational energy levels of the molecule) has changed from 0 to 1 for all the transitions, whereas the rotational quantum number J has either decreased (for the transitions in the so-called P-branch) or increased (for the R-branch) by one quantum, as indicated in Figure 3. The empty space between the branches corresponds to the so-called Q-branch (pure vibrational transition with no change in the rotational state), the lines of which are absent for the HCl molecule, reflecting the fact that the total angular momentum must be conserved (the photon that is absorbed has spin, which is a type of angular momentum).

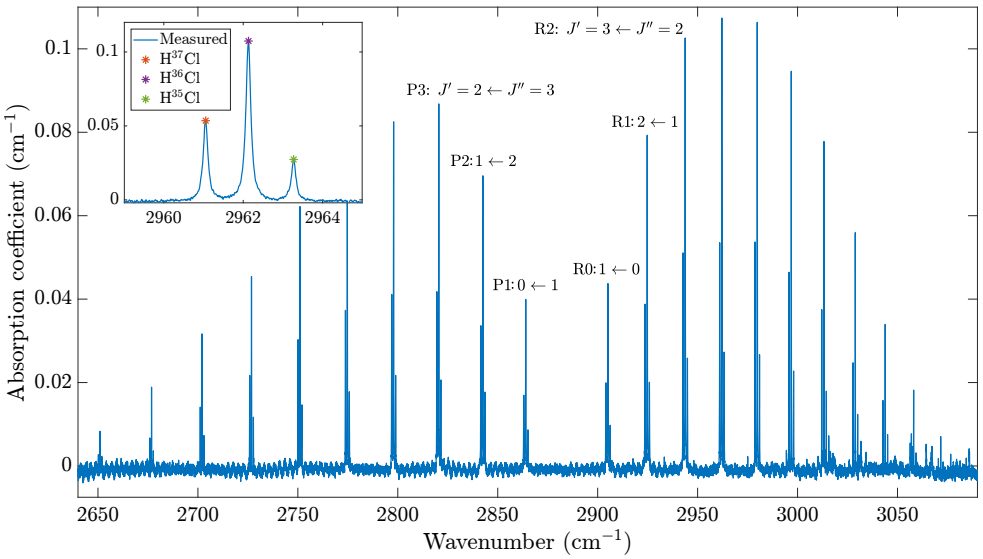

Figure 3: The fundamental rovibrational absorption band of HCl measured in Article II. Compared to the article, I have subtracted water absorption to better reveal the absorption by HCl only. Because the sample contains multiple isotopoloques of HCl, the spectrum consists of three distinct absorption bands, each slightly shifted from one another due to the isotope shift,[40] as revealed by the inset that shows a zoomed-in view to the R3 absorption lines. This means that rovibrational spectroscopy is sensitive to different molecular masses and can be used to discern different isotopologues in a sample. The rotational quantum numbers have been marked for a few transitions in the figure; by common convention, the prime refers to the upper, and the double prime to the lower (vibrational) energy state.

To go into more detail, the more theoretical aspect of spectroscopy tries to apply quantum mechanics to molecular systems in order to derive expressions that would describe what kind of absorption lines one can expect for a given molecule. On the other hand, a measured experimental spectrum can be used to test these models,[41] to determine which quantum mechanical effects are important for the molecule,[42] or to extract experimental values for the parameters in the derived model (such as the bond length mentioned above[43]). The starting point for these approaches is the

(time independent) Schrödinger equation:

$$\hat{H}\psi = E\psi\,, \tag{1.4}$$

where $\hat{H}$ is the Hamiltonian operator that consists of operators describing the particles' translational and potential energies. The Schrödinger equation is basically a second order differential equation whose solutions are the wavefunctions ψ that describe the possible energy eigenstates of the system with E being the corresponding total energy. Even though the equation seems innocently simple, only in rare cases can it be solved analytically.

One quantum mechanical problem that can be solved analytically is the simple harmonic oscillator, a useful model to describe the vibrations of a diatomic molecule, such as HCl. For brevity, I will skip the lengthy derivations that can take up several chapters in many textbooks and will give only the resulting vibrational energies:*

$$E_v = \left(v + \frac{1}{2}\right)\hbar\omega\,, \tag{1.5}$$

where $v \in \mathbb{N}_0$ and $\omega = (k_\mathrm{f}/\mu)^{1/2}$, where in turn μ is the effective mass[44] and k_f is the bond stiffness, another structural parameter whose experimental value can be determined experimentally by studying absorption spectra.

It can be shown that for a harmonic oscillator, only radiative transitions with $\Delta v = 1$ are possible, with the transition $v' = 1 \leftarrow v'' = 0$ corresponding to the already mentioned fundamental vibrational transition. This is another example of a selection rule in spectroscopy. However, in reality a molecular system is not exactly harmonic,† which means that also transitions such as the first overtone $v' = 2 \leftarrow v'' = 0$ are allowed, albeit they are much weaker (see Table 1). Both the fundamental and the first overtone rovibrational transition bands of $\mathrm{H}^{36}\mathrm{Cl}$ were measured in Article II.

Also molecular rotation can be considered in a similar manner, which leads to a rotational energy expression[40]

$$E_J = B_v(J+1) - D_v J^2(J+1)^2 + H_v J^3(J+1)^3 + \cdots\,, \tag{1.6}$$

where J is the rotational angular momentum quantum number, and, in particular, $B_v = \hbar/(4\pi\mu r_v^2)$ is the rotational constant with r_v the (vibrational state dependent) equilibrium bond length. The higher order molecular constants (D, H, ...) consider further corrections to the energy expression such as the non-rigidity of the rotator.

Finally we arrive at the spectroscopic expression that describes the absorption lines appearing in the HCl rovibrational band. By defining the integer $m \equiv -J'' = -J' - 1$ for the P-branch and $m \equiv J' = J'' + 1$ for the R-branch, and denoting the pure vibrational transition frequency (the band center) by $\nu_{v\leftarrow 0}$, the rovibrational transition frequencies for both branches can be expressed (up to H) as

*More information on basic quantum chemistry can be found in the excellent textbooks [44], [45] or [28], all books that have been close companions of mine during my studies.

†Anharmonicity also slightly changes the vibrational energies, which is typically considered by the inclusion of additional expansion terms to different powers of $(v + 1/2)$ in the vibrational energy expression (1.5).

$$
\begin{aligned}
\nu &= E_{v'=v} - E_{v''=0} + E_{J'} - E_{J''} \\
&= \nu_{v\leftarrow 0} + (B_v + B_0)m + (B_v - B_0 - D_v + D_0)m^2 \\
&+ (H_v + H_0 - 2D_v - 2D_0)m^3 + (3H_v - 3H_0 - D_v + D_0)m^4 \\
&+ (3H_v + 3H_0)m^5 + (H_v - H_0)m^6 \,. \qquad (1.7)
\end{aligned}
$$

In Article II, the measured absorption lines were fitted with Lorentz profiles to extract the absorption line center frequencies. Then, the above expression was fitted to these data to determine the structural coefficients.* This is a traditional way of analysing the measured spectrum and it was done because it serves as a sanity check for the measurements: because the fit converged nicely to the measured data, it gives us confidence that the measurements have been successful. On the other hand, it is rather easy to fit a polynomial to any kind of data, especially if the polynomial is flexible enough. Even though the fit does serve as a tool to reproduce the measured absorption line centers, one may question if the structural constants truly hold physical meaning. In addition, it is known that such polynomial expressions perform poorly in extrapolating absorption line centers beyond the measured frequency range.[46–48]

Fortunately, more refined methods exist.[46,49] These typically make use of a number of experimental line position data sets for a given molecule and its isotologues to infer the underlying potential energy function that can subsequently be used to back-calculate the line positions but also the molecular constants. Alternatively,[50] one can also fit the so-called Dunham parameters (basically a more rigorous formulation for the molecular constants[51]) in an isotope-independent manner to experimental data consisting of a large number of line positions describing multiple isotopologues. Regarding the latter approach, I am pleased that the work in Article II inspired Velichko and Mikhailenko,[48] and later Marinina *et al.*[52] to consider the $H^{36}Cl$ absorption bands more rigorously.

In the work by Velichko and Mikhailenko,[48] they used their previously determined, isotopically independent Dunham parameters (determined from experimental data on several isotopologues of HCl other than the $H^{36}Cl$ one)[50] to calculate the transition wavenumbers for the fundamental and the two first overtone bands of $H^{36}Cl$ (lines P25–R25). The line positions produced by their model agree with our experimental data within the experimental uncertainties, not including a few lines, for which, in hindsight, the signal-to-noise ratios were probably too poor for it to be prudent to include them in the fits. In addition, when outside the wavenumber range for which we could extract experimental data (we managed lines P10–R10 for the fundamental, and P1–R7 for the first overtone band), the line positions calculated based on the molecular constants I determined in Article II can deviate greatly from the ones from their model, as expected (see Table 3 in Section 2.6). Finally, in a later work, Marinina *et al.*[52] used the results from [48] to calculate the line intensities for the $H^{36}Cl$ molecule. I am glad that our experimental contribution led to this increased knowledge on this specific isotopologue of HCl, which data will be useful for any future application that wants to detect this molecule using absorption spectroscopy.

*More precisely, a reduced dataset was generated by calculating suitable differences between the measured absorption line frequencies to limit the number of parameters to be fitted at a time. This is known as the combination differences approach.[40,42]

To close off this section on spectroscopic models, I want to note that the above has considered only one of the simplest possible molecules, a heteronuclear diatomic molecule. If molecules of more complex symmetries are considered, the absorption spectra and the spectroscopic expressions that describe them become much more complicated. For example, in Article I we measured and analysed the fundamental antisymmetric stretching rovibrational ν_3 band of the $^{14}CH_4$ molecule. Due to the spherical symmetry of the molecule, the absorption spectrum does resemble that of the heteronuclear diatomic molecule. However, a Q-branch emerges and the absorption lines in the P- and R-branches show fine structure (see the figures in Article I). The corresponding energy expressions then consist of many more terms with some of them describing the splitting of the absorption lines. In that case, a simple polynomial fit does not suffice, but one needs to construct and diagonalize Hamiltonian matrices in a suitable basis set as part of the fitting routine to obtain the wavefunctions and the corresponding energies. Such a fit was performed by Professor Lauri Halonen for Article I.

1.3 Instrumentation and photoacoustic spectroscopy

The previous section was about the more theoretical aspects of spectroscopy, and no more is said about those in the rest of this thesis. Instead, the rest of this thesis considers at least as important an aspect of spectroscopy: instrumentation. In other words, I discuss how to construct experimental setups to enable the measurement of the absorption spectra in the first place so that one could then analyse them, theoretically or otherwise. Even though the basic concept of an absorption measurement is quite simple (recall Fig. 2), when targeting trace gas detection (such as the parts-per-billion-level noise-equivalent limit of detection of $^{14}CH_4$ in Article I), or otherwise weak transitions (such as the 10^{-25} $\mathrm{cm}^{-1}/\mathrm{cm}^{-2}$ level line intensity in Article V), the simple approach in Figure 2 won't suffice, but more sophisticated and increasingly complex experimental setups are typically needed. If targeting the otherwise strong fundamental rovibrational absorption bands in the mid-infrared optical region, a further complication is that suitable light sources may not be readily available.

One nice example of a more sophisticated experimental setup than the one in Figure 2 is the one used in Article I. We required a high power and widely tunable continuous-wave light source in the mid-infrared wavelength region. To that end, I constructed an optical parametric oscillator, which is a light source based on nonlinear optics.* Basically, if a properly shaped 1 µm laser beam (called the pump beam) is suitably focused (mode matched) into an optical resonator and into a so-called nonlinear crystal (in our case, a periodically poled lithium niobate crystal) that lies inside the resonator, due to the special response of the crystal material to the incoming electric field, the pump photons are split into near-infrared (signal) and mid-infrared (idler) photons.[53] While the generated signal beam circulates inside the resonator, the idler beam exits the resonator and is guided into the experimental setup. If the signal beam wavelength is properly stabilized inside the resonator, the idler wavelength can be scanned over the absorption feature of interest by scanning the pump wavelength (because the nonlinear process conserves total energy between

*Also the broadband light sources utilized in Articles III and IV are based on nonlinear optics, as discussed later.

the partaking photons). At each wavelength step, the idler wavelength can also be quickly modulated around its average value. Without going into detail, this approach called wavelength modulation absorption spectroscopy (WMAS)[54] leads to the measurement of basically the different order derivatives of the absorption features with the benefit that slowly varying background features are efficiently suppressed.

In addition, instead of using a simple gas cell and a photodetector to record the transmission spectrum, we used cantilever-enhanced photoacoustic spectroscopy (CEPAS).[23] This technique is used in almost all the works in this thesis (apart from Articles II and IV) due to its high sensitivity. Basically, when the gas sample is trapped inside a closed volume (the sample cell), absorption inside the cell leads to a slight increase of the sample temperature and consequently to a slightly increased pressure.[55] If the incident optical power is then modulated, for example, by using an optical chopper (or in the case of Article I by using the WMAS approach), the periodic absorption leads to the generation of a sound wave, which can then be recorded with a sensitive microphone. In the case of CEPAS, this sensitive microphone is a silicon cantilever that bends as response to the pressure modulation, which movement is monitored interferometrically to convert the pressure modulation into a corresponding voltage signal.[56,57] This technique has been proven to be one of the most sensitive spectroscopic techniques available. For example, Tomberg *et al.*[58] demonstrated, at the time, a record sub-parts-per-trillion detection limit of HF using the CEPAS technique combined with a high-power OPO light source.

The sensitivity improvement is possible, because the photoacoustic signal (microphone output voltage) is proportional to the incident optical power:[55]

$$V = S_{\mathrm{m}} C_{\mathrm{cell}} P \alpha(\tilde{\nu}) \,, \tag{1.8}$$

where S_{m} is the microphone sensitivity (V/Pa), C_{cell} the cell constant (Pa/[W cm^{-1}]), P the incident optical power (W) and $\alpha(\tilde{\nu})$ the absorption coefficient (cm^{-1}). In this thesis, I have utilized the above property that the sensitivity in PAS scales with the optical power: the 3 ppb noise-equivalent limit of detection of $^{14}CH_4$ in Article I was thanks to the high-power OPO light source, and the detection of the extremely weak transitions of acetylene at the 1 µm wavelength region in Article V was enabled by amplifying the input laser optical power. Note also how the signal in PAS is directly proportional to absorption, which means that one, in a way, skips the transmission spectrum measurement step of the Beer–Lambert law. While this leads to benefits as described below, the technique does not readily offer absolute absorption measurements (as opposed to the transmission spectrum measurement approach) but typically requires calibration, *i.e.*, the determination of the proportionality product $S_{\mathrm{m}} C_{\mathrm{cell}} P$.

Another reason for the high sensitivity of (CE)PAS is that, at least in principle, the technique is background-free. What this means is that the detected signal is generated only if absorption occurs – it is easier to detect a signal rising above the noise floor of the measurement compared to having to detect a small dip in a transmission spectrum, particularly because each extra optical frequency that is detected contributes to additional (laser intensity) noise in the measurement.[59] Regarding Fourier-transform spectroscopy (the topic of the next section), the background-free nature of CEPAS leads to the effective use of the detector dynamic range, which then leads to sensitivity gains, in addition to the reduced intensity noise, as was nicely demonstrated in Article III and elsewhere.[59]

In this thesis work, I have used the CEPAS implementation as commercialized by Gasera Ltd since the invention of the technique by Wilcken and Kauppinen *et al.* in the University of Turku.[56,57] It should be noted that also other cantilever-enhanced PAS approaches exist.[23] In addition, another highly sensitive PAS approach is the quartz-enhanced (QEPAS) approach, where a modulated light beam is focused in between the prongs of a quartz tuning fork that converts the sound waves to an electrical signal due to the piezoelectric effect.[60,61] Competing, or even unprecedented sensitivities can be achieved, particularly if combined with other tricks to enhance the sensitivity, such as the joint utilization of optical and acoustic resonances.[13]

Finally, also other highly-sensitive optical techniques than PAS exist, such as cavity ring-down spectroscopy (CRDS),[62] noise-immune cavity-enhanced optical heterodyne molecular spectroscopy (NICE-OHMS)[63] or saturated-absorption cavity ring-down spectroscopy (SCAR),[64] the lattermost technique offering the highest (parts-per-quadrillion) sensitivities currently achievable with optical methods. A comprehensive review of these techniques is out of scope for the current thesis. However, it suffices to say that the sensitivity benefits with those techniques are achieved by utilizing optical resonators, which typically results in sophisticated but increasingly complex experimental setups, at least compared to CEPAS. All in all, the discussion in this section should nicely illustrate how targeting higher sensitivities or special wavelength regions leads to ever more demanding requirements for the instrumentation and to its own research field under the wide umbrella of spectroscopy.

The above discussion has basically considered laser spectroscopy with single frequency lasers. One benefit of those techniques is the high optical frequency precision defined by the linewidth of the laser used. However, the tunability of single frequency lasers is often limited. For example, in Article I, even though the OPO could be widely (but slowly) tuned by tuning the nonlinear crystal temperature, the actual measurements over the absorption features were done by tuning the pump laser wavelength, which limited the optical bandwidths of a given measurement window to only a few tens of GHz, allowing me to record only a few absorption lines at a time. Wouldn't it be nice to be able to measure over a much larger optical bandwidth, for example, to measure the whole rovibrational band of HCl (Fig. 3) in a single measurement without having to perform any laser wavelength scans but by using broadband light sources? This is indeed possible by using Fourier-transform spectroscopy, which is the topic of the rest of this thesis.

2 Fourier-transform spectroscopy

The goal of any absorption spectroscopy experiment is to record the absorption spectrum, *i.e.*, a curve that describes the absorption as a function of the optical frequency. With tunable single frequency lasers this is easy as a measurement at a chosen optical frequency describes the absorption at that specific frequency, after which the optical frequency can be tuned to repeat the measurement at a new frequency.* Spectroscopy with broadband light sources, meaning with light beams that contain multiple different optical frequencies, comes with the extra difficulty that one needs somehow to tell apart all the different optical frequencies and to determine how the sample absorbs at each of them. One solution is to use a grating, which disperses each optical frequency to a distinct angle so that one can measure the absorption at each of them separately.[28,65] A drawback of this technique is that as the light is dispersed, only a small fraction of the total light intensity is measured at a time, which may lead to a poor signal-to-noise ratio in the measurement.[66–69] In addition, the resolution of the instrument may be limited as the resolving power of the grating may not be sufficient.

Fourier-transform (infrared) spectroscopy (FTS, or more traditionally, FTIR) is another way to perform broadband spectroscopy without the need to disperse the light beam. It is an age-old technique developed to a mature level already during the previous century, starting from the 1950s,[68,70] and it is still widely used in academia and industry. For example, high-resolution FTIR instruments (even almost the same model as we used in Article II) are still used for high-quality linelist measurements,[20,71,72] and, as a chemistry student, one of the first analyses performed after synthesizing some organic compound in a lab course was to run an FTIR measurement on the product to detect any impurities and to see the emergence of the characteristic absorption features of the product molecule to prove the success of the synthesis. Since the invention of the optical frequency comb light source, its combination with an FTIR instrument,[73,74] and the first dual-comb spectroscopy experiment,[25,75] FTS research has been revived to a new renaissance – including my writing the present thesis where I contribute to the field by demonstrating new FTS research: the use of a traditional FTIR instrument to measure and analyse the up to now unstudied absorption spectrum of the $H^{36}Cl$ molecule (Article II), the in-depth analysis of the relatively new phase-controlled FTS technique and its application to CEPAS (Article III), our simple approach for dual-comb spectroscopy (Article IV) and the proposition of a completely new FTS technique based on the rotational Doppler effect (Article V).

Traditional FTIR is based on the Michelson interferometer, a type of frequency down-converter (depicted in Fig. 4),[66,76] which maps each optical frequency to some more slowly oscillating but easily detectable intensity modulation. This is required because the optical frequencies (oscillations of the electric field that are in the THz regime) are too fast to be measured directly. The goal of FTS is to record a time domain signal called the interferogram, which consists of a sum of different sinusoidal intensity modulation signals, each corresponding to a unique optical frequency. The interferogram is a sort of time-domain representation of the incoming optical field,

*Of course, the spectrum of a "single frequency" laser is never an infinitely narrow line. However, the kHz or a MHz linewidth of a typical continuous-wave laser used for spectroscopic purposes can be considered negligible in the context of this thesis.

such that the interferogram can be converted to the corresponding spectrum by calculating its Fourier transform. Fourier transform (FT) is a mathematical operation that basically answers to the question, which frequencies with which amplitudes and phases one needs to sum up to yield the time domain signal one started with.[77]

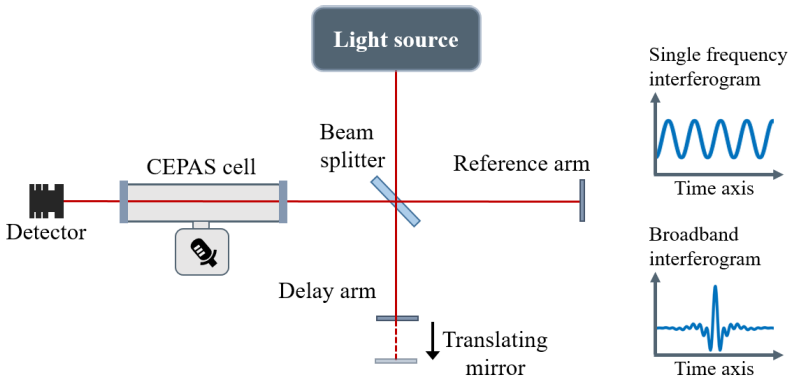

Figure 4: Schematic of a traditional FTIR instrument. The interferogram is formed at the detector due to interference between the combined light fields from the two arms when the delay arm length is scanned. The detector can either be a conventional photodetector, or one can use photoacoustic detection.

In the Michelson interferometer (Fig. 4), the incoming light beam is split into two arms of the interferometer. The two beams are then back-reflected and combined again, after which they are guided through the sample and onto a photodetector. To perform a measurement, one scans the length of one of the arms (the delay arm), which basically delays the optical field travelling in that arm. When the delayed beam is combined with that from the other (reference) arm, the two beams interfere on the detector: Depending on the delay, the two electric fields either sum up in phase (interfere constructively), or out of phase (destructive interference). In the former case, the intensity observed at the detector is that of the incident light source, but in the latter, no intensity is detected (the light beams are perfectly reflected towards the light source to conserve total energy). If the back-reflecting mirror in the delay arm is translated with a constant velocity, one detects sinusoidal intensity modulation at the detector in the case of a single frequency light beam (see the inset of Fig. 4). In the case of a broadband light source, each optical frequency is down-converted to intensity modulation signal appearing at a unique frequency such that the interferogram then consists of the sum of all of them. At zero optical path difference, all the sinusoids sum up in phase. When the path difference is scanned, each of the down-converted sinusoids fall increasingly out of phase, meaning that the interferogram of a broadband light source appears as a burst-like shape, often called the centerburst. Once the interferogram has been recorded, it is Fourier-transformed to yield the corresponding spectrum. If the down-conversion relation is known (Eq. 2.1), the down-converted frequency axis can be scaled to the corresponding optical frequency axis.

2.1 Down-conversion relation

To derive the down-conversion relation in FTIR, let's denote the mirror velocity by u. In a time t, the (optical) path difference scanned is $2ut$. For a light beam of wavelength λ, the scan length corresponds to $2ut/\lambda$ optical cycles. This basically means that the intensity modulation appears at a frequency $2u/\lambda$. Converting the wavelength to the optical frequency, the down-conversion relation is

$$f_{\mathrm{down}} = \frac{2u}{c}\nu\,, \tag{2.1}$$

where c is the speed of light, and where $2u/c$ is called the down-conversion factor. We notice that, indeed, each optical frequency is mapped to a unique down-converted frequency, the value of which can be chosen by choosing the translational velocity of the mirror. For example, in Article II, the scan speed of the FTIR instrument was chosen to be 2.5 cm/s, which down-converts the red HeNe reference laser optical frequency (474 THz; 633 nm) to 80 kHz, the measurement of which value allows one to determine the down-conversion factor. Appendix A2 shows a more quantitative derivation of the intensity modulation signal.

2.2 Conventional versus photoacoustic detection

It was said that the interferogram of a broadband light source consists of a single burst centered around the zero path difference. On the other hand, any structure in the spectrum, such as absorption, is seen as multiple side bursts around the centerburst, as shown in Figure 5. To explain these interferogram shapes, and to illustrate the benefits of using (CE)PAS detection in FTS (Article III), Figure 5e shows the interferogram corresponding to the absorptive part only. It is these latter types of interferograms that one measures with photoacoustic spectroscopy, as signal is generated from the intensity modulation only if absorption occurs at that specific optical frequency. This is in contrast to a transmission spectrum measurement, where one basically measures the sum of the interferogram describing the light source spectrum and the interferogram describing only the absorption. To see this, let's make the small absorption approximation to the Beer–Lambert law (1.1), which yields $S(\nu) \approx S_0(\nu)(1-\alpha(\nu)L)$, where this time I denote the spectrum with $S(\nu)$. A basic property of the Fourier transform is that the FT of a sum is the sum of the FTs of the functions that are summed.[66] Therefore, the resulting interferogram

$$I(t) = \mathrm{FT}[S(\nu)] = I_0(t) - \mathrm{FT}[S_0(\nu)\alpha(\nu)L]\,, \tag{2.2}$$

where $I_0(t)$ is the interferogram corresponding to the light source spectrum and where $S_0(\nu)\alpha(\nu)L$ is the spectrum that the (CE)PAS detector sees. This is one benefit of using CEPAS detection in Fourier-transform spectroscopy: As only the absorptive part generates signal, one can increase the input optical power to efficiently fit the interferogram to fill the photodetector voltage range (unless detector nonlinearity is a problem[78,79]). With a transmission spectrum measurement, it is the large centerburst describing mainly the nonabsorbing part of the optical spectrum that fills the majority of the usable detector range such that the smaller sidebursts may be masked by noise. In addition, in cases where the measurement sensitivity is limited

by the light source intensity noise, CEPAS detection may lead to higher sensitivity measurements as only the frequencies that are absorbed contribute to the total intensity noise. This has been discussed at length, *e.g.*, in [59], and it was also demonstrated in Article III that the CEPAS approach indeed leads to more sensitive FTS measurements.

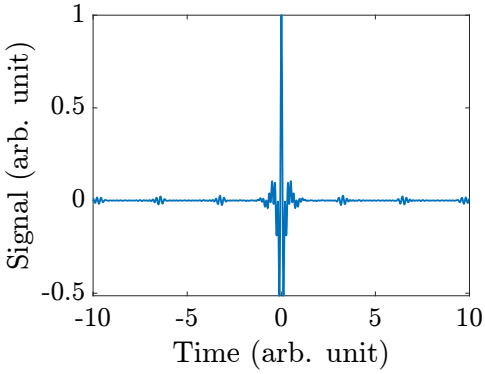

(a) Interferogram of a broadband light source modified by sample absorption. The absorption information is encoded as the small sidebursts around the centerburst.

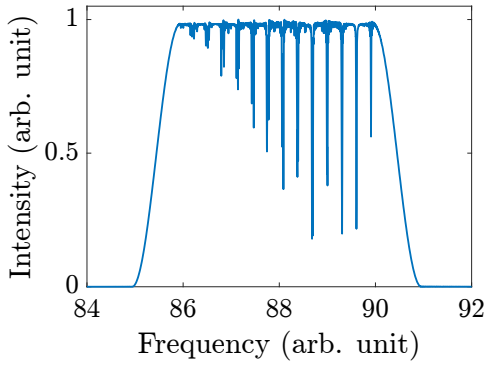

(b) Corresponding spectrum of (a).

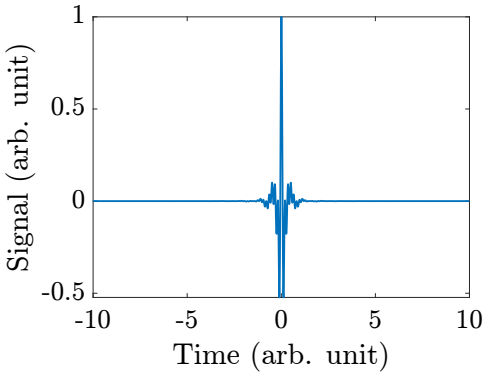

(c) Interferogram of a broadband light source without absorption, which means that no sidebursts appear.

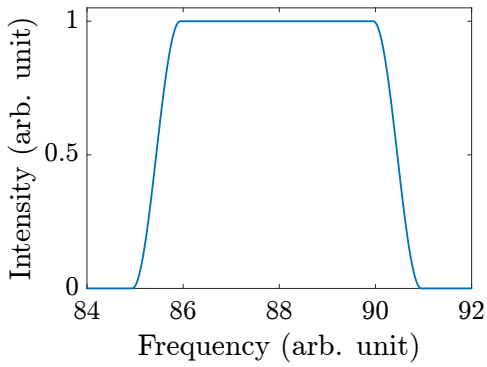

(d) Corresponding spectrum of (c).

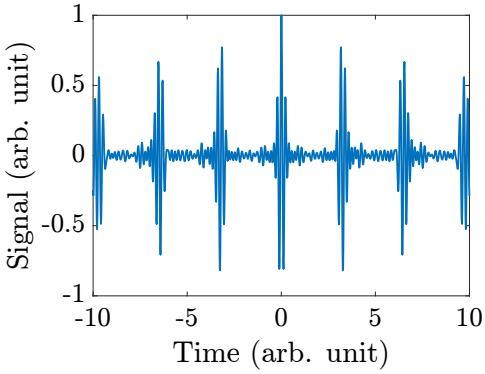

(e) Interferogram corresponding to the sample absorption only.

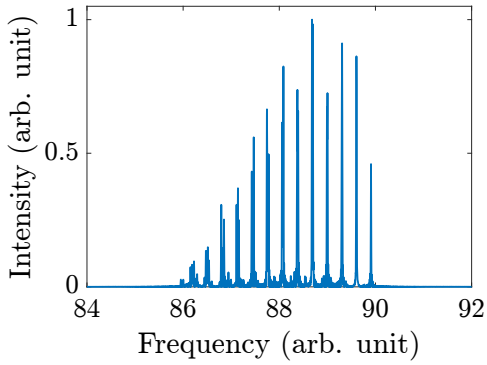

(f) Corresponding spectrum of (e).

Figure 5: Broadband interferograms and corresponding spectra.

2.3 Spectral resolution

Spectral resolution means the capability of a spectroscopic instrument to tell apart two close-lying optical frequencies.[80] In tunable single frequency laser spectroscopy, this is ultimately limited by the laser linewidth (a type of instrument lineshape function) as there is no benefit in densening the spectral point spacing beyond this. In some contexts, resolution may mean the capability of discerning two close-lying absorption features from one another. In that context, the resolution may be limited by the chosen spectral point spacing, or even pressure because absorption features broaden as a function of the pressure. In the context of Fourier-transform spectroscopy, resolution refers to the width of the so-called instrument lineshape function (ILS), which is usually limited by the measurement time (the mirror scan distance).* This can be intuitively explained by remembering that as the FTIR instrument is scanned, the optical frequencies fall increasingly out of phase. To observe the destructive interference for two infinitely close frequencies, an infinitely long measurement time (scan length) would be required.

A basic property of the Fourier transform is that the FT of a product is the convolution of the FTs of the functions that are multiplied.[66] When measuring a single optical frequency but truncating the measurement, the interferogram is basically the product of the sinusoid and a boxcar function. The corresponding FT is then the convolution of a delta function (infinitely narrow line) and a sinc function (the FT of the boxcar), which basically yields a sinc function located at the frequency of the sinusoid. It then follows that when measuring an interferogram consisting of two optical frequencies, the ability to tell them apart in the resulting spectrum depends on the width of the sinc function (the length of the interferogram, *i.e.*, the width of the boxcar).

In this thesis, resolution is defined based on a *double-sided interferogram* as

$$\delta\nu = \frac{1}{\frac{\Delta T}{2}} \times \frac{1}{c_{\mathrm{down}}} \equiv \frac{1}{\Delta T'} \times \frac{1}{c_{\mathrm{down}}}\,, \tag{2.3}$$

where ΔT is the total length of the time window (in the middle of which the centerburst lies for a double-sided measurement; $\Delta T'$ is the "maximum optical delay" defined as the distance from the centerburst time location to the end of the time window), and c_{down} is the down-conversion factor (for FTIR, given by Eq. 2.1), which scales the resolution in the radiofrequency spectrum to the corresponding resolution in the optical spectrum.† This definition corresponds to the width of the base of the sinc ILS function, by which I mean the distance between the first zero-crossings of the sinc function (see Figs. 6a and 6b). In Article III, I was careful to define the resolution as the full-width-at-half-maximum (FWHM) of the ILS function, as it is sometimes defined.[76] Here, I deviate from that definition because even for a sinc ILS, two frequencies separated by the FWHM are completely unresolved (approx.

*The resolution can also be limited by the divergence of the light beam, which is typically governed by using apertures in the FTIR instrument.[66] In Article II, 1 mm input aperture diameter was used not to limit the resolution otherwise achievable with the chosen mechanical scan distance. Due to the low divergence of a typical collimated laser beam, which type of light was used in this thesis work apart from Article II, I omit any further discussion about input apertures.

†Note that for traditional FTIR, this resolution definition reduces to a simple form with the insertion of the down-conversion factor (2.1): $\delta\nu = \frac{u}{L'} \times \frac{c}{2u} = \frac{c}{2L'}$, where $L' = u\Delta T'$ is the mechanical scan length starting from the zero optical delay (centerburst location).

20 % dip in between them is observed when the separation is 1.2 times the FWHM). In contrast, two sinc functions separated by the width of their base are completely resolved, and ILSs resulting from some more drastic apodization functions are still most likely resolved at least to some extent, as illustrated in Figure 6b.

If the interferogram is apodized (multiplied) with some other function than (only) a boxcar, it yields some other instrument lineshape function than a sinc function. Figure 6a illustrates three different apodization functions used in this thesis work: the already mentioned boxcar, the "Norton–Beer medium" used in the HCl work in Article II,* and a typical envelope function observed for the single frequency interferograms in the phase-controlled FTS work in Article III (this envelope function is probably the result from some misalignment or imaging errors in the optical setup, for which reason it is called here a self-apodizing function). The effect of these apodizing functions is that the resulting broadband spectrum is the convolution of the underlying spectrum without apodization and the resulting instrument lineshape function, which basically broadens the absorption features, making it increasingly difficult to discern close-lying absorption features. The highest possible resolution is observed with the sinc ILS, but using a stronger apodization function can smoothen the sometimes aggressive sinc oscillations in the spectrum baseline. Figure 6c illustrates the effects of different amounts of apodization in the context of the PC-FTS work in Article III.

This discussion on optical resolution reveals one of the biggest drawbacks of traditional FTIR for gas-phase absorption spectroscopy, where measuring sharp absorption features with negligible instrumental broadening requires long scan lengths and consequently slow measurements. For example, assuming the 2.5 cm/s scan speed and 680 MHz resolution (44 cm double-sided mechanical scan length) used in the HCl work in Article II, the measurement of a single interferogram can take tens of seconds, whereas averaging multiple interferograms can easily increase the total measurement time to several minutes. The invention of dual-comb spectroscopy (the topic of Section 4) has greatly improved this as high resolution measurements can be performed in a fraction of a second but with minimal crosstalk between adjacent optical frequencies, making the measurements resemble those performed with tunable single frequency lasers that exhibit negligible instrumental broadening.† For example, in Article IV a single interferogram corresponding to 250 MHz optical resolution was recorded in less than 100 µs! Also Articles III and V deal with increasing the measurement speeds. While the phase-controlled FTS technique (Section 3) allowed more than a ten-fold increase in the measurement speed compared to traditional FTIR for fixed (albeit modest) resolution, the rotational Doppler FTS technique (Section 5) promises both fast and high-resolution measurements with an experimental setup much simpler than in dual-comb spectroscopy.

*This function is defined by $f(t) = \sum_{i=0}^{2} C_i \left[1 - (t/\Delta T')^2\right]^i$ with $-\Delta T' \leq t \leq \Delta T'$ and $C_0 = 0.152442$, $C_1 = -0.136176$ and $C_2 = 0.983734$.[81,82]

†Note that using a special FTS technique[96,97] employing an optical frequency comb light source, basically ILS-free measurements or resolutions beyond the nominal resolution of the FTIR instrument can be achieved.

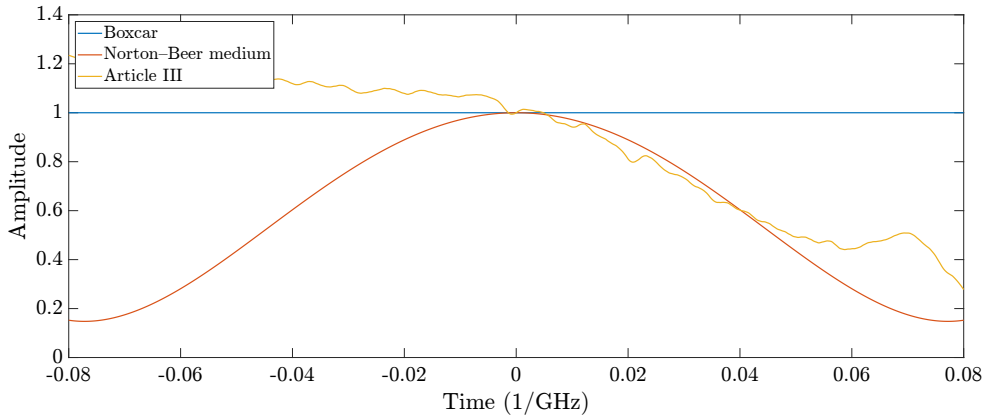

(a) Apodization functions. "Article III" corresponds to the experimental self-apodization observed for the single frequency interferograms in the phase-controlled FTS work. The Norton–Beer medium ILS is relevant for the HCl work in Article II.

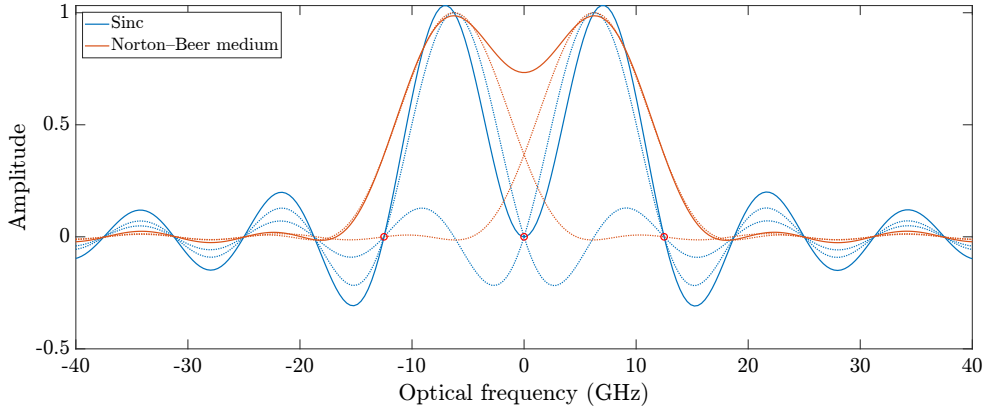

(b) The Fourier transform (spectrum) of an interferogram consisting of two optical frequencies separated by 12.5 GHz and apodized with the boxcar or with the Norton–Beer medium apodization functions in (a). Note how the two optical frequencies are completely separated with the sinc instrument lineshape function (12.5 GHz wide base; $12.5 \times 0.603\,\mathrm{GHz} = 7.54$ GHz FWHM), but also reasonably well separated with the Norton–Beer medium ILS (26 % dip; the FWHM is 1.4 times that of the sinc function).

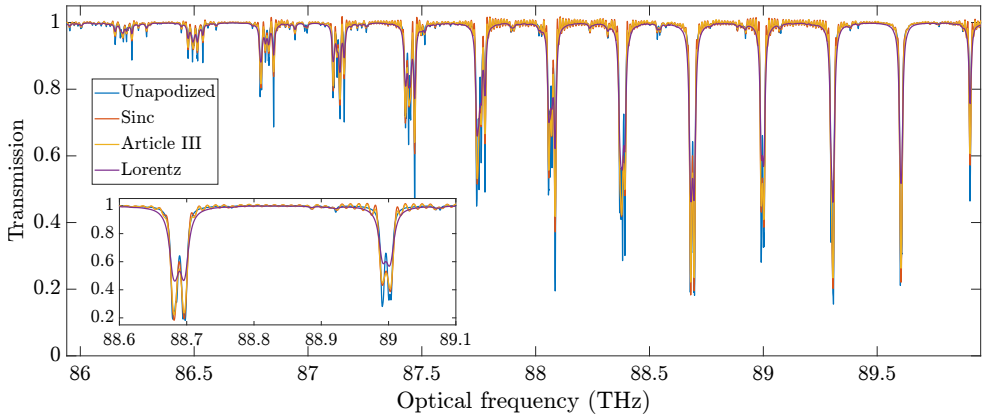

(c) The effect of apodization on a simulated methane transmission spectrum with the same experimental conditions as in the PC-FTS work in Article III. The resolution here corresponds to 12.5 GHz wide sinc base, see (b). Note how the "Article III" self-apodization function (see panel a) results in a spectrum much closer to that obtained with the sinc ILS function than to the Lorentz convolution spectrum, which is included here to foreshadow how the realised resolution in Article III deviates in a major way from the expected resolution.

Figure 6: Illustration of different apodization functions, the corresponding instrument lineshape functions, and their effect on a broadband spectrum.

2.4 Phase correction

In Fourier-transform spectroscopy, many corrections on the interferograms may be required. In phase-controlled FTS (Article III), the so-called phase- and group-delay corrections are needed, as discussed in Section 3. In dual-comb spectroscopy (Article IV; Section 4), timing jitter and (time-dependent) phase corrections are performed. For completeness, here I briefly discuss the (frequency dependent) phase correction as it is defined in FTIR literature, even though it was used only in Article II (as implemented by the FTIR instrument manufacturer). Note that the FTIR phase correction is not the same thing as the (time-dependent) phase correction in dual-comb spectroscopy or the phase-delay correction in PC-FTS, but the FTIR phase correction could be performed in addition to those.

Due to possible dispersion in an FTIR instrument, misalignment, asymmetrical sampling about the centerburst, or due to other reasons, an interferogram is rarely perfectly symmetrical, which means that the Fourier transform is a complex function with its real part representing the symmetric and the imaginary the asymmetric part of the interferogram.[66,67,76,83–85] The simplest approach to obtain the spectrum is to measure a double-sided interferogram, Fourier-transform it and take the absolute value of the result. The problem with this approach is that it rectifies all noise, which results in poor noise reduction when averaging spectra. In addition, because of the noise rectification, a noise offset is generated where light intensity is close to zero, leading to possible misinterpretation of the absorption peak heights, especially with photoacoustic detection as the intensity is basically zero everywhere except at the absorption peaks.

Instead, one can recover the true spectrum $S'(\nu)$ as the real part of the complex FT by performing the phase correction, which means the calculation of

$$S'(\nu) = \mathrm{Real}[S(\nu) \times \exp(-\mathrm{i}\phi(\nu))]\,, \tag{2.4}$$

where $S(\nu)$ is the complex spectrum and $\phi(\nu) = \arctan\left(\mathrm{Im}[S(\nu)]/\mathrm{Real}[S(\nu)]\right)$ is the phase spectrum. This operation basically shifts all the information about the spectrum from the imaginary side to the real side, making the underlying interferogram effectively symmetrical again, and allowing one to recover the spectrum as the real part of the FT only.

Another benefit of the phase correction is that it can be used to increase the resolution of the spectrum up to two times compared to the measurement of a double-sided interferogram. This is done by recording only a short double-sided portion around the centerburst from which to calculate the phase spectrum, but by continuing the interferogram measurement on one side of the centerburst for as long as the instrument allows. The resulting resolution then corresponds to that calculated based on the length of the one-sided portion ($1/\Delta T'/c_{\mathrm{down}}$, where $\Delta T'$ is the length of the one-sided portion; see Eq. 2.3). It is noteworthy that in the case of unequal-sided interferograms, the phase correction is mandatory to realise the increased resolution and to avoid additional distortion of the spectrum, as illustrated in Figure 7 and discussed, *e.g.*, in [67]. In addition, the double sided part needs to be weighted properly to avoid double counting of the information around the centerburst. Finally, prior to FT, the interferogram can be zero-padded to make the spectrum appear smoother (addition of zeros is seen as interpolation of the spectrum to denser sampling) and

the interferogram should be circularly shifted about the centerburst, for example, about the maximum value of the centerburst in the Mertz method.[76] This references the phase to the centerburst (otherwise, the phase spectrum will exhibit only noise).

In the PC-FTS work in Article III, I did not use the phase correction but recorded only double sided interferograms and defined the spectra as the absolute value of the complex FT. This was done for simplicity as it is well known that any inaccuracies in the phase correction can easily distort the spectrum even for double-sided, but especially for unequal-sided interferograms.[85] Instead, the reference spectrum against which I compared the measurements was derived from the experimental self-apodization function (deduced from typical envelopes of the single frequency interferograms; see Supplement 1 of Article III, and recall Fig. 6a). However, the derived reference spectrum is much closer to that assuming a perfect sinc instrument lineshape function than to that exhibiting the realised resolution (see Fig. 6c). Even though part of the discrepancies might be explained due to ill-behaving noise and the lack of phase correction, the main reason for the differences is the imperfect phase- and group-delay corrections as discussed in Section 3 and proved in Appendix A5.2.

2.5 Light sources and the optical frequency comb

Traditionally, one would use incoherent, such as thermal light sources in an FTIR instrument. For example, in the HCl work in Article II, we used a Globar light source for the mid-infrared and a tungsten light source for the near-infrared measurements. The benefit of these light sources is that they are relatively simple and compact devices that offer a wide spectral bandwidth (several thousand cm^{-1}). However, due to their large divergence, they may be difficult to align into more sophisticated experimental setups and can limit the resolution of the measurement, unless governed with an aperture (which in turn decreases the optical throughput). For example, even though incoherent light sources can be used, *e.g.*, for phase-controlled FTS (Section 3),[22] the alignment of such a light source would have been difficult, and it also would have degraded the sensitivity due to the already high losses of the experimental setup.* In contrast, collimated lasers due to their high brightness, directionality and low divergence are extremely attractive light sources for FTS,[73,86–88] even though their optical bandwidths are typically modest compared to thermal light sources. For example, one special broadband laser type greatly important for this thesis is the optical frequency comb (OFC), a light source used in Articles III and IV. The typical optical bandwidth was a few tens (Article IV) or a few hundred (Article III) inverse centimeters. More generally, the optical bandwidths of OFCs can exceed the thousand cm^{-1} mark.[86,89,90]

The spectrum of an optical frequency comb consists of extremely narrow, equidistant lines. As such, it can be thought as a collection of continuous wave lasers. The optical frequencies of an OFC can be defined via

$$\nu_n = n f_\mathrm{r} + f_0 \,, \tag{2.5}$$

where f_r is the repetition frequency (the distance between adjacent optical frequency components), n is the mode number (integer labelling the comb tooth in question)

*The PC-FTS setup utilizes a grating, which leads to high optical losses.

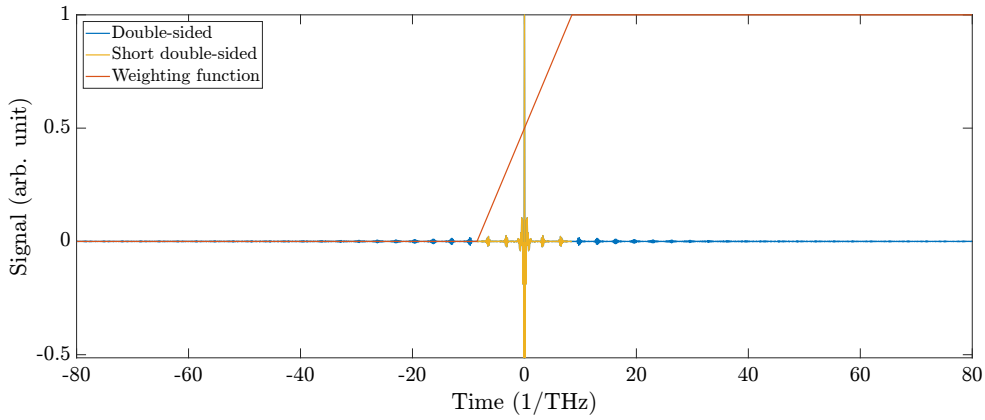

(a) The short double sided interferogram (without the weighting ramp) is used to determine the phase spectrum for the phase correction of the unequal-sided interferogram (obtained here by multiplying the full resolution double-sided interferogram with the weighting function).

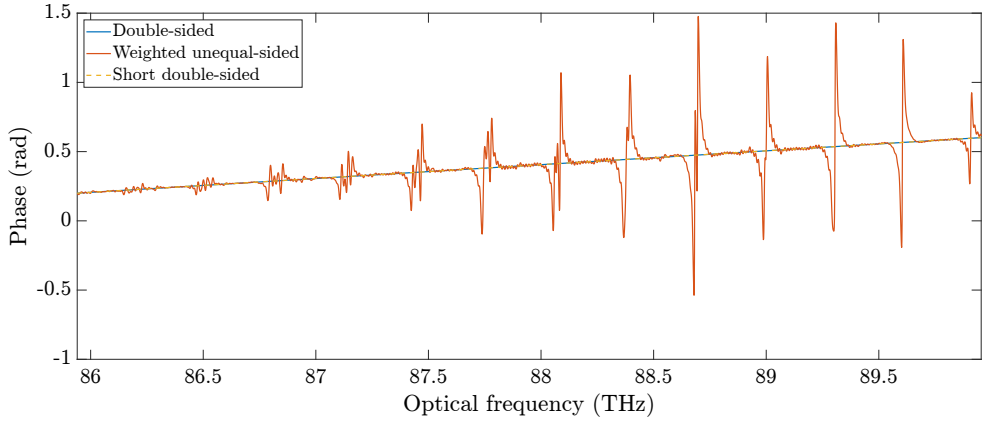

(b) The phase spectrum obtained from the short double-sided interferogram matches nicely the phase of the full resolution double-sided interferogram. In contrast, using the phase spectrum from the weighted unequal-sided interferogram would result in a distorted spectrum.

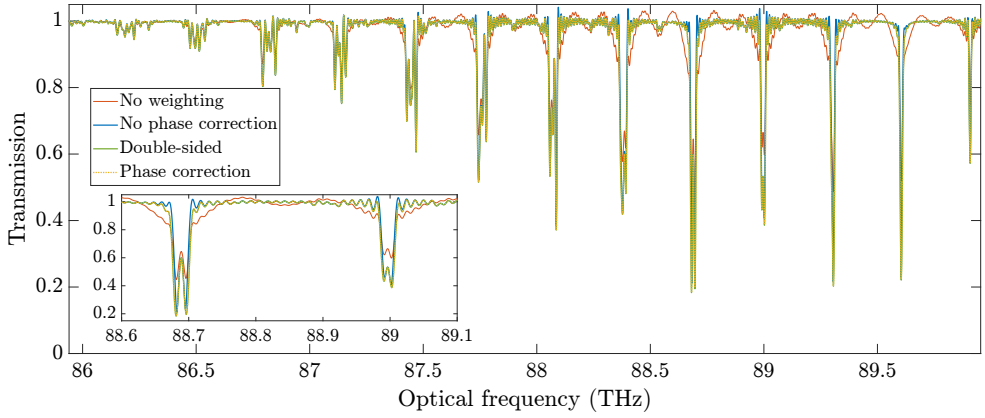

(c) The phase correction of the properly weighted unequal-sided interferogram using the phase spectrum obtained from the (unweighted) short double-sided interferogram results in a sinc instrument lineshape function and yields the same resolution as would be obtained with the full resolution double-sided interferogram, even though in the case of the unequal-sided interferogram, effectively almost only half of the total length of the double-sided interferogram has been measured. In contrast, the absolute value of the FT of the properly weighted unequal-sided interferogram yields a slightly distorted spectrum (*i.e.*, if the phase correction is not performed). The effect is even more drastic if the weighting is not performed for the short double-sided portion in the unequal-sided interferogram.

Figure 7: Illustration of the FTIR phase correction.

and f_0 the carrier-envelope offset frequency. There are different approaches for OFC generation,[86] the mode-locked lasers being the only type of which I consider here.[91,92] In the time domain, the output from such lasers consists of ultrashort pulses (femtosecond pulses in our case) that exit the device at the repetition frequency. To construct such short pulses, it means that in the frequency domain, a collection of different optical frequencies that sum up in phase are required (in that sense, this discussion is analogous to the explanation of FTIR that a broad spectrum yields a short burst-like interferogram in the time-domain). Considering the OFCs used in Articles III and IV, we started from a commercial mode-locked laser (Menlo Systems) at the 1 µm wavelength region and converted the light to the 1.5 µm (used in Article IV) and 3 µm (used in Article III) wavelength regions in a nonlinear crystal.[93] The process is seeded by a 1.5 µm continuous-wave laser, which acts as a pre-generated comb tooth, ensuring a comb-teeth structure for the newly generated beams at the new wavelengths.

One major benefit of using OFCs as light sources in FTIR is that if the radiofrequencies f_r and f_0 that define the OFC are stabilized to radiofrequency references, extremely frequency-accurate measurements can be achieved.[86,94] This, however, requires high resolution scans from the FTIR instrument. On the other hand, matching the scan lengths to the repetition rate frequency can yield basically instrument lineshape function-free measurements with only modest scan lengths.[94–97] Unfortunately, the phase-controlled FTS technique utilized in Article III (Section 3) does not offer spectral resolutions high enough to fully exploit the frequency precision of OFC light sources, nor was it expected to. Still, the high brightness and directionality of the OFC were otherwise useful. On the other hand, dual-comb spectroscopy (Section 4) utilizes two OFCs and allows extremely fast, high-resolution measurements, as made use of in Article IV.

2.6 Spectroscopy of $H^{36}Cl$

To summarize the results obtained in Article II, we used a commercial high-resolution FTIR instrument (Bruker IFS 120 HR) to measure the fundamental and the first overtone rovibrational bands of the radioactive $H^{36}Cl$ molecule at atmospheric pressure and with 680 MHz resolution (sinc base definition; Norton–Beer medium apodization function). Due to the atmospheric pressure, I used Lorentzian functions for the absorption line fits, which was supported by the fact that no obvious structure emerged under the absorption peaks in the fit residuals. On the other hand, part of the broadening of the absorption lines are still due to the instrumental and the Doppler broadening (with the former effect exceeding the latter in our case). This was considered in the uncertainty budget when stating the fitted linewidths as the pressure broadened linewidths. Still, while the estimated total uncertainties for the determined linewidths were typically 3 %, the actual values were typically 10 % larger than expected based on previous measurements of the different HCl isotopologues,[98] for which the differences between the pressure broadenings seem negligible.[99] I suspect these discrepancies may stem from, *e.g.*, unaccounted for misalignment of the instrument, or from some other reason that broaden the instrument lineshape function beyond the stated nominal resolution. In Appendix A4.1, I study in more detail the Lorentzian fit model assumption and the effect of the ILS when fitting the absorption lines.

On the other hand, the linewidth results were extra as the main objective of the article was to determine the absorption line center wavenumbers, which we managed for several lines (P10–R10) in the fundamental band, as summarized in Table 3. The measured fundamental rovibrational band has already been shown in Figure 3. For completeness, Figure 8 shows the measured overtone band. Despite the long averaging (100 interferograms), the SNR of this spectrum is only modest. Still, we were able to successfully determine the line positions of several lines (P1–R7) even in this band. Furthermore, the band fit analysis already discussed in Section 1.2 was performed for both bands.

This work was gratifying to me, as the spectrum of HCl is perhaps the most famous one: it serves as the first example of a rovibrational spectrum for any Bachelor student in a course on the basics of spectroscopy. In Bachelor-level physical chemistry lab works, I have measured the rovibrational band of HCl (and later served as an assistant on that course for many years) using a low-resolution table-top FTIR instrument with the Cl-35 and -37 isotopologues barely resolved. Here, a high-resolution instrument was used, which allowed these isotopologues to be fully resolved, including the Cl-36 one, the spectrum of which has not been previously measured. It was therefore quite interesting to still be able to contribute something new to the spectroscopy of the HCl molecule. Further still, our work inspired further theoretical studies on the $H^{36}Cl$ molecule,[48,52] as already summarized in Section 1.

More generally, interest towards optical measurements of radioactive molecules has increased in recent years. For example, VTT (Technical Research Centre of Finland) has extensively studied the $^{14}CO_2$ molecule,[12,100] as has also CNR-INO in Italy,[64,101,102] but also others.[103,104] The goal is to develop cheaper and more portable laser spectroscopy instruments (compared to accelerator mass spectrometry[105]) for the detection of this molecule, which is important as $^{14}CO_2$ can be emitted from nuclear waste.[102] The $H^{36}Cl$ molecule is also interesting in the same context as it can be found in nuclear reactor materials.[106] The detection of any molecule using laser spectroscopy requires knowledge of the center wavenumbers of its absorption lines, which are now provided for $H^{36}Cl$ by our work in Article II.

Table 3: Summary of the $H^{36}Cl$ absorption peak center wavenumber results in Article II (measured, or calculated based on the molecular constants) compared to those calculated in [48]; recall the discussion about spectroscopic models in Section 1.2. The calculated values in [48] agree with our experimental ones within the experimental uncertainties for the non-outlier lines. All numerical values are in cm^{-1}.

Band	$1 \leftarrow 0$	$2 \leftarrow 0$
Measured lines	P10–R10	P1–R7
Largest uncertainty (68 % confidence level)	0.002	0.007
Outlier lines according to calculations in [48]	P10, P9 and P6	P1 and R0
Largest discrepancy of *measured* lines compared to [48] including the outlier lines	0.0036	0.022
Largest discrepancy of *calculated* lines compared to [48] within the experimental range	0.0027	0.0043
Discrepancy of the *calculated* line R25 compared to [48]	0.309	-0.926

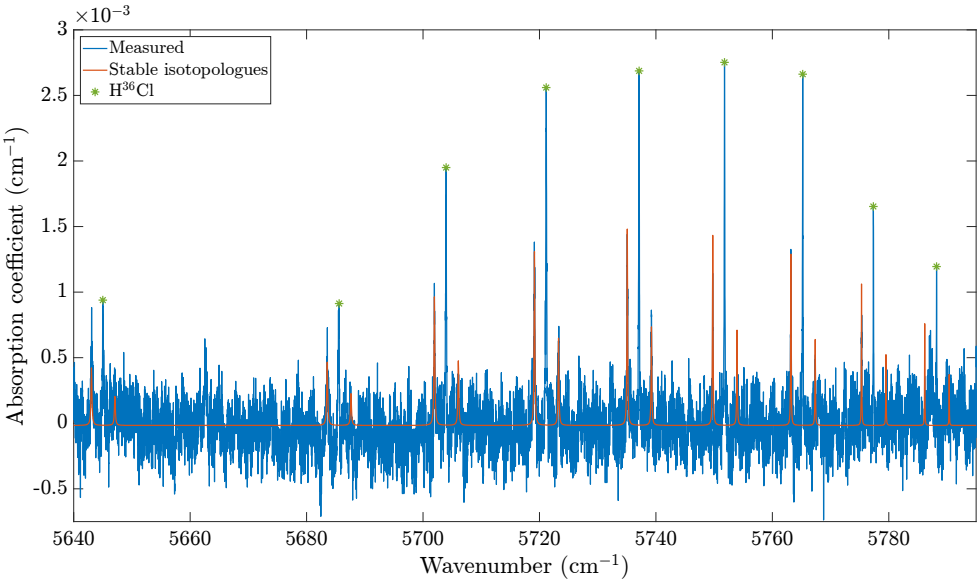

Figure 8: The first overtone absorption band of $H^{36}Cl$ (lines P1–R7), as measured for Article II. Note that this is not the raw data, but I have subtracted a sine function (to consider spectral etalon fringes) and a simulated water absorption spectrum to better reveal the absorption by HCl only. The simulated HITRAN spectrum for the stable isotopologues $H^{35}Cl$ and $H^{37}Cl$ has been drawn to show that the $H^{36}Cl$ absorption lines fall between those of the stable isotopologues.

3 Phase-controlled Fourier-transform spectroscopy

In our research group, we have worked quite extensively with cantilever-enhanced photoacoustic spectroscopy (CEPAS). For example, the record HF detection limit measurement in [58], or the radiomethane work in Article I both utilized CEPAS. We have also used CEPAS combined with FTIR, for example, in [24] that preceded the work in Article I, but also in the works that form the bulk of the doctoral thesis by Tommi Mikkonen.[107] The use of CEPAS with FTIR is possible, because the detection utilizes a low-stiffness cantilever that allows simultaneous detection of multiple sound waves, in other words, the detection does not require that the modulation frequency coincides with the resonance frequency of the detector like in quartz-enhanced PAS.[108] The trade-off of using the low-stiffness cantilever, however, is that the detection bandwidth is limited to low audio frequencies, typically to frequencies below 600 Hz,* see Figure 9. This leads to long measurements because the FTIR instrument needs to be scanned very slowly in order to down-convert the optical frequencies of interest below that 600 Hz. For example, the measurements in Article II would have required as slow as ~1 mm/s mechanical scan velocities from a traditional FTIR instrument and consequently 25 s long interferograms (12 GHz resolution; 2.5 cm mechanical double-sided scan length).

When we came across the interesting new phase-controlled Fourier-transform spectroscopy (PC-FTS) technique first demonstrated by Hashimoto and Ideguchi,[21] we

*Detection above the 600 Hz resonance up to about 1 kHz is also possible[59] but possibly with reduced sensitivity.

were intrigued. They showed that by replacing the translating mirror of a traditional FTIR instrument with a special type of delay line, fast, Nyquist-limited measurements could be achieved. This technique sounded like a solution to our problems with the slow CEPAS-FTIR measurements, and we wanted to test if this new PC-FTS technique could work with CEPAS. In the end, we demonstrated a 13-fold speed improvement in broadband CEPAS measurements by using the PC-FTS technique instead of traditional FTIR. In the experiment, we measured the P-branch (lines P14–P3) of the fundamental asymmetric stretching ν_3 band of methane using the mid-infrared optical frequency comb generator constructed by Mikhail Roiz.[93]

One new insight from the work in Article III was the importance of a feature of CEPAS that has previously been mostly overlooked: Even though CEPAS allows broadband detection due to its wide response, the response is (down-converted) frequency dependent, which requires an extra normalization step, unless the detection is limited to a narrow bandwidth within the relatively flat response region between, say, 200–400 Hz (see Fig. 9). More importantly, the (down-converted) frequency dependent response requires stable scan velocities by the instrument, because otherwise the non-constant scan velocities couple to the signal strength and lead to a distorted instrument lineshape function (recall the self-apodization function discussion in Section 2.3). In that sense it could be that a long- and stably-scanning traditional FTIR instrument is more suited for CEPAS than the back-and-forth scanning, accelerating and decelerating galvanometric scanner used in Article II. Alternatively, one could test using a polygonal scanner that rotates in a continuous manner,[21] or one can appreciate the vortex-comb spectroscopy technique in Article V that also is based on continuous rotational motion.

We also emphasized in Article III the requirement for a stable and reproducible scanner even in the case where CEPAS detection is not used. This is because the phase- and group-delay corrections required (explained in Section 3.3) can be more difficult to implement in real time than in traditional FTIR. Finally, I believe that the article is a useful piece of literature for anyone wanting to implement the PC-FTS technique for their application as, since the proof-of-concept demonstrations by Hashimoto *et al.*,[21,22] our article provides a more detailed analysis on the practical limits of the technique, for example, on the expected resolution, optical bandwidth and the speed benefit, which details culminated in my gathering look-up tables in Supplement 1 of the article.

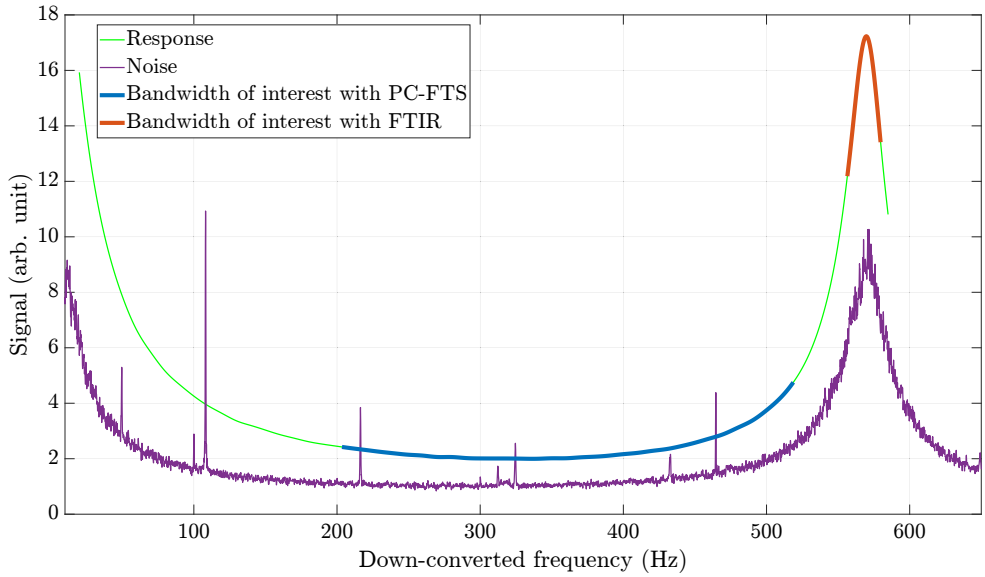

Figure 9: Response and a typical noise spectrum of the CEPAS detector. Note the resonance at 570 Hz. The noise pick-ups are typical for CEPAS and can emerge from electrical signals or from mechanical vibrations. The noise pick-ups did not pose any problems in the measurements here due to the much stronger absorption signals that exceed the CEPAS background noise. The bandwidth of interest means the frequency range to which the optical frequencies between the P14 and P2 absorption lines of methane were down-converted (see Fig. 8 in Article III): the blue curve shows the realised down-conversion with the PC-FTS technique, whereas the orange curve illustrates what the down-conversion would have been if traditional FTIR were used (assuming that the largest optical frequency supported by the PC-FTS instrument is down-converted to 585 Hz by both techniques). The ratio of the blue and orange down-converted bandwidths is 13, reflecting the 13-fold speed improvement achieved in Article III.

3.1 The delay line

Figure 10 illustrates the special delay line utilized in PC-FTS. Basically, the input light hits a grating that disperses the different optical frequency components onto the scanning mirror surface. With the help of the focusing optic, the delay line is constructed to the so-called 4f-geometry that ensures back-reflection of the beam despite the beam pointing deflection that tilting (scanning) the mirror induces. The idea of this special delay line is that because the different optical frequencies strike different locations on the scanning mirror, the *delay difference* between adjacent optical frequencies is increased compared to the traditional FTIR case where the different optical frequencies would strike the same location on the mirror. This means that it suffices to scan only a small angle and still be able to resolve the different optical frequencies. In other words, the optical resolution that is obtained by tilting the mirror by a given angle is increased. Indeed, the delay line can very well be used in normal FTIR mode if the grating is replaced by a plane mirror[109] but it would lead to a decreased resolution for a given measurement time (see Appendix A5.1).

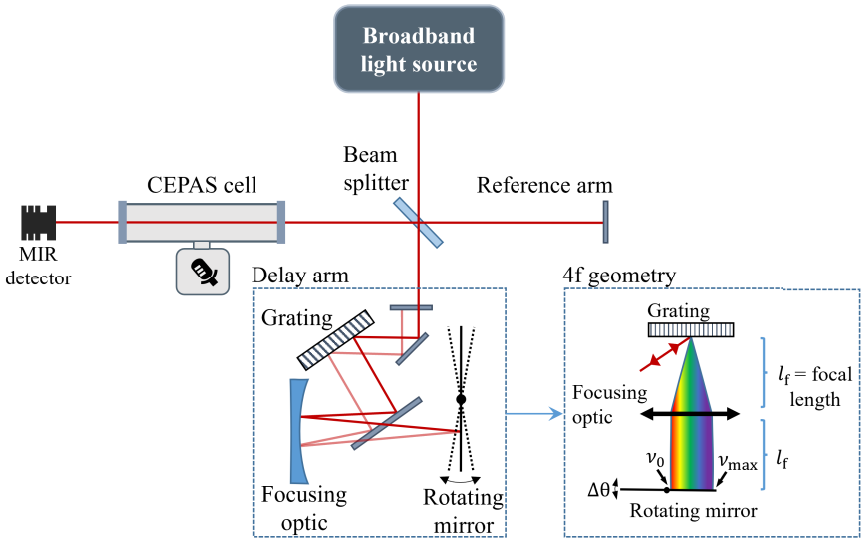

Figure 10: Schematic of the PC-FTS approach. The delay arm consists of a grating, a focusing optic and a rotating mirror in 4f-geometry to ensure back-reflection despite the beam pointing deflection caused by scanning (tilting) the mirror. The red line indicates the path taken by a beam from a single frequency light source; the inset reveals how the grating disperses the different optical frequencies onto the rotating mirror surface in the case of a broadband light source.

On the other hand, if a fixed optical resolution is desired, the interferogram in PC-FTS can be obtained faster than in traditional FTIR by a factor of $\nu_{\mathrm{max}}/\Delta\nu$ (as derived in Supplement 1 of Article III). Here, ν_{max} is the maximum optical frequency of interest, and $\Delta\nu$ is the optical bandwidth that is accommodated onto the scanning mirror surface. This accommodation results in the down-conversion of the optical frequencies according to

$$f = \frac{8 l_{\mathrm{f}} N \Delta\theta f_{\mathrm{scan}}}{\nu_0}(\nu - \nu_0)\,, \tag{3.1}$$

which result can be derived using simple geometry (see Appendix A5.1, or Supplementary Information of [21]). Here, l_{f} is the focal length of the focusing optic in the 4f-geometry, N is the grating groove density, $\Delta\theta$ the maximum mechanical scan angle of the mirror, f_{scan} the scan frequency of the rotating mirror and ν_0 the optical frequency striking the pivot point of the mirror. Compared to the down-conversion relation in traditional FTIR (Eq. 2.1), the down-conversion here depends on many more parameters, all of which may affect the performance of the setup in terms of the desired resolution, optical bandwidth or the maximum down-converted frequency, and in ways not directly clear from the above equation. An in-depth analysis on the effects of all these parameters can be found in Supplement 1 of Article II, including numerical examples found in the look-up tables gathered in the supplement; Table 4 below summarises these effects in a qualitative way.

Table 4: The effect of **increasing** the optical frequency striking the pivot point (ν_0), the optical bandwidth ($\Delta\nu$), the grating groove density (N), the focal length (l_f) or the width of the grating (D) on the speed benefit ($F = \nu_\mathrm{max}/\Delta\nu$), optical resolution ($\delta\nu$), the required scanning mirror width (W) and the required maximum scan angle ($\Delta\theta$), assuming that all other parameters are kept unchanged when one of them is changed. The up-arrow means that the value increases, the down-arrow that it decreases and the horizontal line that the value will be unchanged. For example, increasing the grating groove density has no effect on the speed benefit or the required maximum scan angle, but it improves the optical resolution (the $\delta\nu$ value decreases) while it requires a wider scanning mirror. Note that the results further assume that the maximum down-converted frequency is kept constant, which explains why the speed benefit is affected only by the optical bandwidth and ν_0.*

	F	$\delta\nu$	W	$\Delta\theta$
ν_0	↑	↑	↓	–
$\Delta\nu$	↓	–	↑	–
N	–	↓	↑	–
l_f	–	–	↑	↓
D	–	↓	–	↑

3.2 Speed benefit

The speed benefit in PC-FTS, meaning that an interferogram can be measured by a factor of $\nu_\mathrm{max}/\Delta\nu$ faster than in normal FTIR, can be explained by the fact that the PC-FTS technique stretches the down-converted frequencies to fill the whole detection bandwidth. Then, adjacent down-converted frequencies are widely spaced and a shorter measurement time suffices to resolve them. In contrast, in normal FTIR, the frequencies are densely spaced (see Fig. 3 of Article III, or Fig. 9 here), which then requires a longer measurement time to resolve them. In principle, one could scan the normal FTIR instrument faster to compensate for this, but this would lead to higher down-converted frequencies: in CEPAS, the response of the detector is limited, so scanning faster would first lead to decreased sensitivity and finally to the detector not being able see the interferogram at all. This is what we mean in the article that the PC-FTS technique leads to "fundamentally faster" measurements.

There is also another point of view to the speed benefit. In the work by Hashimoto and Ideguchi,[21] it is not the response of the detector but the highest available sampling frequency that limits the highest possible scan and interferogram acquisition rates. In other words, it is assumed that the measurement has to obey the Nyquist sampling theorem,[76] which basically states that to avoid signal aliasing,† the signal has to be sampled at least with a frequency twice the largest frequency present in the signal. Interestingly, there is a technique well documented in FTIR literature called undersampling.[67,69,76] There, by optically and electronically filtering the signal in a suitable manner to ensure that there is empty space in the detection bandwidth above the zero frequency but below the start of the down-converted frequency bandwidth

*For example, increasing N requires using a wider scanning mirror because the optical frequencies are dispersed to a larger span of angles, resulting in a wider spot that the scanning mirror needs to accommodate. Then, the optical frequency striking the edge of the mirror will experience a larger delay for a given mirror tilt than previously, which means that one needs to scan slower to keep the highest down-converted frequency constant, meaning that no improved speed benefit is achieved.

†Meaning, to avoid the sampled signal appearing at some completely different frequency than the underlying true signal such that it could even overlap with some other signals of interest.

where the spectrum would appear if the Nyquist sampling theorem were adhered to, one can choose to undersample the interferogram to make the spectrum appear as a suitable alias at lower frequencies and still be able to ensure unique mapping between the optical and down-converted frequencies. Then, it could be possible to increase the scan speed to stretch the spectrum to efficiently fill the whole detection bandwidth similar to PC-FTS. However, in applications requiring the fastest interferogram acquisition rates, there surely is a limit to how fast one can scan any mechanical scanner. Then, the PC-FTS technique offers the benefit of not having to scan that fast but still being able to record the interferogram with the fixed target resolution.

Unfortunately, there is a caveat to the speed benefit of PC-FTS. The $\nu_{\max}/\Delta\nu$-fold speed improvement (decreased measurement time) will lead to a decreased signal-to-noise ratio (SNR) by a factor $\sqrt{\Delta\nu/\nu_{\max}}$, *i.e.*, by the square root of the inverse of the decrease in the measurement time, a result I have also verified with numerical simulations. However, note that this is not a special feature of PC-FTS *per se* but is common to all FTS techniques: the SNR is proportional to the square root of the measurement time as discussed in more detail in Appendix A3.

Still, the speed benefit can be useful even if the SNR is correspondingly worsened. Regarding CEPAS measurements, one benefit could be the measurement of sticky gases: the spectrum needs to be measured as fast as possible, after which a new gas exchange or flushing is desired before a new measurement is made in order to minimize the effect that the concentration of the molecules of interest in the gas phase can change as a function of time due to wall ad/desorption. Apparently, this was a problem in the HF work in [58]. More generally, regarding measurements without CEPAS, it can be desired to obtain spectra as fast as possible, for example, to monitor some fast phenomena in real time. Such applications include, for example, dynamic mixing of liquids as demonstrated by Hashimoto *et al.*,[22] combustion analytics,[110] or perhaps monitoring chemical reactions.[19] Finally, it is always a benefit to be able to obtain a spectrum fast. From personal experience, it is frustrating to wait for long periods of time for a measurement to be completed only to find that it needs to be repeated. If the spectrum could be obtained fast, and if the preliminary results seem promising, one can always decide to average until a desired SNR is achieved.

3.3 Phase- and group-delay correction

The PC-FTS technique also comes with the drawback that more complicated interferogram corrections are required. In traditional FTIR, it suffices to perform the so called group-delay correction. "Group delay" can be explained most simply in the case of using a broadband light source that emits light pulses. The group *velocity* describes the velocity by which these pulses travel.[111] The delay line in an FTIR instrument delays these pulses, hence the term group *delay*; the interferogram then forms as these pulse pairs strike the detector and interfere as a function of the delay.[112]

The group delay is obtained as the frequency derivative of the *phase* delay, which describes how a given optical frequency is delayed in the system. This is basically the down-conversion relation, if multiplied by 2π and time t. In another words, it is

$\phi_\nu(t) = -2\pi c_{\mathrm{down}}(t)\nu t$ for traditional FTIR. The group delay is then[21]

$$\tau(t) = -\frac{1}{2\pi}\frac{\mathrm{d}\phi_\nu(t)}{\mathrm{d}\nu} = c_{\mathrm{down}}(t)t\,, \tag{3.2}$$

where the FTIR down-conversion factor $c_{\mathrm{down}}(t) = 2u(t)/c$ is generally time dependent (nonlinear) if the translating mirror travels with an inconstant velocity. Traditionally, this can be considered by monitoring, simultaneously with the broadband interferogram, the interferogram of a red HeNe alignment laser whose beam travels in the system jointly with the broadband light beam. Then, the inconstant velocity of the mirror will be seen as time dependence in the down-converted frequency of the HeNe laser, while it is known that the actual optical frequency of the HeNe laser should be, for all practical purposes, constant. The zero-crossings of the HeNe laser interferogram can then be used to resample the broadband interferogram,[113] or the detection system can be designed to trigger a measurement point every time the HeNe laser interferogram crosses zero voltage. This linearises the time axis.*

In PC-FTS, the down-conversion relation (3.1) depends, in addition to the down-conversion factor, on the frequency ν_0. This frequency is defined as the optical frequency that hits the pivot point of the rotating mirror (and is therefore down-converted to the zero frequency), which is also time dependent as the mirror surface is generally not situated exactly at the pivot point but is offset due to the finite thickness of the mirror. This leads to a phase drift that is common for all of the optical frequencies,† an effect that needs to be considered separately from the group delay correction, as this drift will be cancelled from the correction signal when calculating the frequency derivative (the group delay), as can be seen from Equation (S13) in Supplement 1 of Article III. Basically, the phase- and group-delay corrections can be performed by recording, not one as in traditional FTIR, but two single frequency interferograms at two different optical frequencies, and by using those measurements to derive correction curves, one of which is used to induce a (time dependent) phase shift for the broadband interferogram, and the other to resample the interferogram to yield a linear delay axis, as is discussed in detail in Supplement 1 of Article III.

Because the phase- and group-delay corrections require simultaneous monitoring of two optical frequencies, the corrections are more difficult to implement in real time than in traditional FTIR. Indeed, in Article III we performed the corrections based on separate measurements, stored the correction curves, and used them to post-correct newly measured broadband interferograms. It turned out that the mirror scanning was not reproducible enough, which distorted the instrument lineshape function and yielded a lower-resolution absorption spectrum than expected. Figure 11 shows the final measured CEPAS absorption spectrum together with a few reference spectra: a reference spectrum corresponding to the ideal (sinc) instrument lineshape function

*Strictly speaking, the (lab) time axis is always linear, but it is the effective optical time, *e.g.*, the group delay axis that is linearised by the group delay correction; the effective optical time axis is obtained from the lab time axis by multiplying with the down-conversion factor.

†For a reader already familiar with dual-comb spectroscopy, this phase drift basically describes the drift of the envelope offset frequency of the interferogram, which basically describes the shape of the burst within its envelope; the group-delay correction corresponds to the correction of the drift or jitter of the repetition rate difference, which affects the locations of the burst envelopes. In other words, the group vs. phase delay discussion separates the phase drifts that an optical frequency can experience to a part that describes phase common to all the frequencies and to a part that scales as a function of the frequency.

(13.3 GHz resolution), a spectrum corresponding to the expected instrument lineshape function (basically the spectrum already shown in Fig. 6c), and a spectrum convoluted with a Lorentzian function (10.5 GHz FWHM) that matches reasonably well with the experimental spectrum. There is no actual theoretical justification for assuming this lattermost ILS, but it simply seemed to match best with the experiment compared to a couple of other ILSs that I tried. The main idea here is simply to show that, at least qualitatively, all the acetylene absorption peaks are present and that their heights qualitatively follow those expected. The reason for the distorted spectrum is, as mentioned, the irreproducibility of the mirror scanning, which led to residual phase noise that degraded the spectrum quality despite the interferogram corrections. In Article III, I mentioned that this hypothesis was supported by some numerical simulations. In Appendix A5.2, I show these simulations.

Still, I want to point out that despite the current problem with the reduced spectrum quality, spectra like that shown in Figure 11 could most likely be used already, *e.g.*, for methane concentration measurements. The obvious approach would be to perform calibration curve measurements, *i.e.*, to measure such spectra at different methane concentrations, as for example has been done in [14,16]. Of course, ideally the irreproducibility problem of the mirror scans should be solved to improve the spectrum quality. The simplest approach would be to invest in a more stable scanner, or perhaps the corrections could be implemented in real time, to which end one could draw inspiration from dual-comb literature.[114,115] Finally, if the reduced resolution is not a problem, one could simply use the delay line in normal FTIR mode (by replacing the grating with a plane mirror), which would then simplify the corrections. In any case, I suspect that it will be difficult to push the resolution of PC-FTS measurements to, or beyond, the 1 GHz level,* which limits its use in high resolution gas-phase measurements. Alternatively, by combining the technique with an optical frequency comb that has a few GHz mode spacing, one could perform interleaving measurements beyond the nominal resolution.[116,117]

*For example, by solving the scanner instability and the self-apodization problems, by performing one-sided measurements and by using, say, a two times wider (50 cm) and 1.5 times higher groove density (450 mm^{-1}) grating, perhaps the currently achieved highest resolution (12 GHz) demonstrated in Article III could be improved down to 2 GHz. However, at high resolutions and large scan angles, aberrations or other new problems could potentially arise.[110]

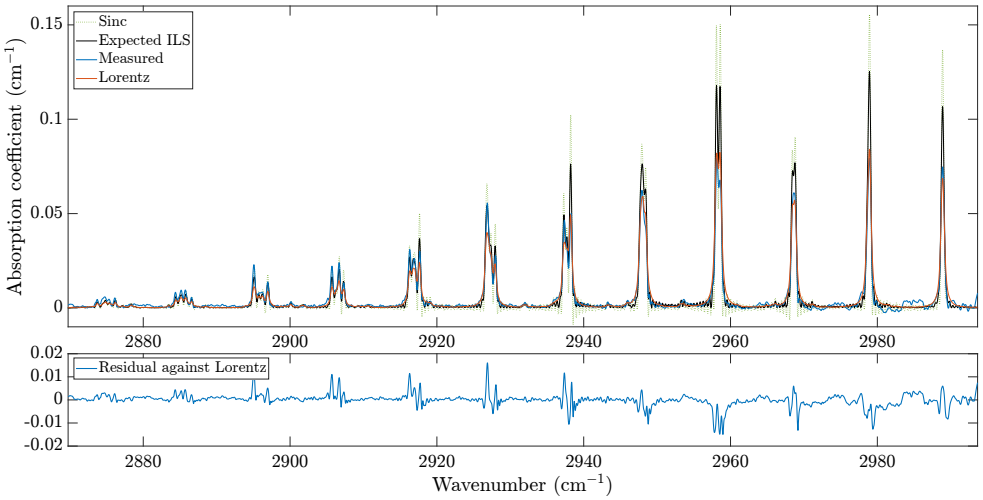

Figure 11: The absorption band (lines P14–P3) of methane measured with the CEPAS-PC-FTS approach for Article III, together with the reference spectra discussed in the text.

4 Dual-comb spectroscopy

As mentioned in Section 3, with pulsed light sources, Fourier-transform spectroscopy can be explained by noting that the interferometer delays the pulses in the delay arm so that the interferogram is generated when the pulses from the two arms slide over one another and interfere. Splitting the incoming pulse train into the arms of a scanning interferometer can then be viewed, in a way, as copying the pulse train but such that the delay arm effectively changes the repetition rate of the pulse train travelling in the delay arm. One can then envision that Fourier-transform spectroscopy could be performed without any mechanical scanning parts by simply spatially overlapping the beams from two optical frequency combs that have slightly different repetition rates. This is the basis for dual-comb spectroscopy (DCS),[25,118] a technique that has revolutionized the field of Fourier-transform spectroscopy.

In the frequency domain, DCS can be understood through beating between the different comb teeth of the two light sources, as illustrated in Figure 12: depending on the carrier-envelope offset frequencies and the repetition rates of the combs, some comb teeth pairs overlap in their optical frequencies, but the optical frequencies of the subsequent ones differ in increasing multiples of the repetition frequency difference Δf_r. In other words, the first comb teeth pair is down-converted to the zero radiofrequency, the next one to Δf_r, the next one to $2\Delta f_\mathrm{r}$, and so on. This leads to a down-conversion relation[25]

$$f_\mathrm{RF} = \frac{\Delta f_\mathrm{r}}{f_\mathrm{r}}(\nu - \nu_0)\,, \tag{4.1}$$

where ν_0 is the optical frequency of the overlapping comb teeth and ν the optical frequency that will be mapped to the radiofrequency f_RF. Similar to PC-FTS, as only the optical bandwidth of interest is down-converted, this allows efficient use of the detection bandwidth and leads to fast measurements. In fact, for DCS, the

Nyquist sampling theorem dictates that the optical bandwidth needs to satisfy

$$\Delta\nu \leq \frac{f_\mathrm{r}^2}{2\Delta f_\mathrm{r}}\,, \tag{4.2}$$

which follows from Equation (4.1) by noting that it is the repetition rate of the laser that ultimately limits the sampling rate (*i.e.*, $f_{\mathrm{RF,max}} \leq f_\mathrm{r}/2 \equiv f_\mathrm{s}/2$): as the interferogram is formed by pulse pairs striking the detector, we cannot get information any faster than at the rate at which new pulse pairs are generated. Equation (4.2) then shows that by having control over the optical bandwidth that is to be down-converted, one can increase the repetition rate difference, which in turn increases the rate at which new interferograms can be recorded: one interferogram (with a single "centerburst" in the lingo of traditional FTS) is generated after a time $1/\Delta f_\mathrm{r}$, after which a new interferogram (burst) will start to form.

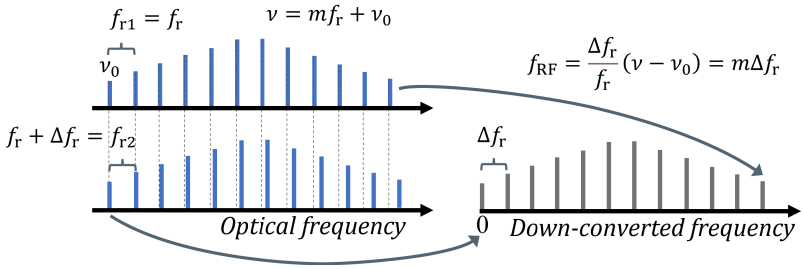

Figure 12: Principle of the down-conversion in DCS. The down-converted spectrum in the radiofrequency domain is obtained due to beating between the comb teeth of the two optical frequency combs that have slightly different repetition rates.

To give a numerical example, in Article IV we used OFCs with repetition rates of approximately 250 MHz. However, it was the sampling rate of the data acquisition card at our disposal that limited the sampling rate to 200 MHz. By using a repetition rate difference of 11.7 kHz, we were able to down-convert a maximal optical bandwidth of 194.05–195.58 THz (1.53 THz) to 4–76 MHz (see the experimental spectra in Section 4.2). Then, a single interferogram was recorded in 85 µs (at a rate 11.7 kHz). On the other hand, there is no need to stop the measurement after a single interferogram has been recorded, but often a train of such bursts is measured before Fourier-transformation. Hereafter, a single interferogram is called a **burst** and a time-window consisting of multiple successive bursts a **segment**. Indeed, in Article IV, we typically recorded segments consisting of 937 bursts, which corresponds to a total measurement time of 80 ms. The Fourier transform of such a segment then corresponds to an optical (radiofrequency) resolution of less than 1 MHz (25 Hz).* Compare this to the HCl work (Article II), where sub-GHz resolution with an FTIR instrument took several seconds. These numbers illustrate the power of DCS: high resolution measurements can be achieved in an incredibly short measurement time. For example, dual-comb spectrometers reaching a few µs interferogram acquisition rates are promising tools for gas-phase reaction kinetics.[10,18]

Another benefit of DCS is that if all the degrees of freedom of the partaking OFCs, namely, the carrier-envelope offset frequencies and the repetition frequencies of the

*This number is misleading as it describes the so-called mutual coherence of the two OFCs, achieved in post-processing. This basically means that despite the fact that the two OFCs may (do) drift during a measurement, a narrow linewidth can still be achieved despite the underlying optical frequency inaccuracy, which value is estimated later in this section.

combs are referenced to external standards and stabilized, extremely frequency-accurate measurements with a precision of ~kHz in the optical frequency regime can be conducted.[25,90,112,119,120] In the spectroscopic demonstrations presented in this thesis, however, no such high frequency accuracy was necessary. Instead, the OFCs involved were basically free-running (but mutually coherent, see below). Even in this case, frequency accuracy in the order of MHz can typically be achieved.[25] In our case, the frequency accuracy is mostly defined by 1) the linewidth of the CW laser that is used to define the frequencies of the overlapping comb teeth as discussed below, and 2) by the absolute drifts of the repetition rates of the OFCs during measurements. For example, a typical drift of the CW laser was < 30 MHz during the long-time averaging measurement (~20 min) discussed in Article IV. On the other hand, typical repetition rate drift of a single comb was in the order of a few tens of hertz. This corresponds to an absolute optical frequency drift of 50 MHz for a comb line at the optical frequency of 195 THz (mode number $\approx$ 780 000, given the 250 MHz repetition rate). This frequency accuracy was enough for our purposes, where the absorption linewidths were typically close to 1 GHz (see Table 2).

Even if the OFCs involved are free-running in the absolute sense, to achieve reasonable signal-to-noise ratios (SNRs) and long-time averaging, the two OFCs need to be *mutually coherent*. Basically, as the carrier-envelope offsets and repetition frequencies of both combs typically drift and jitter independently from one another, when the beams from such light sources are overlapped for interference, these instabilities are seen as drift and jitter in the interferogram shapes and their arrival times, leading to degradation of the instrument lineshape function and SNR, unless properly addressed. Further still, averaging such segments without proper corrections can lead to the interferograms washing out completely. This is an issue for DCS, because coherent averaging is needed to improve the SNR: recall from section 3 that increasing the measurement speed (decreasing the measurement time) leads to decreasing SNR.

There are different approaches for ensuring mutual coherence. The most obvious but also the most laborious approach is to stabilize both combs in the absolute sense, for example, by locking two comb modes at different parts of the optical spectrum against auxiliary lasers (that themselves may be stabilized against external frequency references to improve the frequency accuracy).[112,119] Another approach is to stabilize the repetition and carrier-envelope offset frequencies of one of the combs, and then force the corresponding degrees of freedom of the other comb to follow those of the first one.[121] On the other hand, at least partial mutual coherence can be achieved passively, for example, for the repetition rates in the form of dual-comb lasers where the optical frequency combs share the same laser cavity,[122–124] or for the carrier-envelope frequency by cancelling it via generating the optical frequency combs using nonlinear optics.[125–127]

This discussion reveals one of the biggest drawbacks of DCS. Even though the technique is conceptually quite simple in the sense that one simply needs to overlap two laser beams on a detector to observe interference, the requirement for this high mutual coherence easily results in sophisticated but complex experimental setups, particularly if opting for an active stabilization scheme. Regarding these, with the many phase-locked loops often required, measurements can lack robustness or long-term operation capability as the locks are easily disturbed by environmental interferences such as by mechanical vibrations, from which I have intimate personal experience by having participated in carrying out the measurements presented in Article IV.

In recent years, more and more research has been dedicated to finding solutions to avoid having to use optical phase locks altogether to simplify the experiments. In that regard, different post-correction algorithms have been demonstrated. For example, using auxiliary lasers, one can derive optical error signals such that one of the signals describes the interferogram phase and the other the relative timing jitter between the combs. Instead of using these for stabilizing the OFCs by phase-locked loops, they can be digitized and used for post-corrections.[115,128] Further still, in the so-called adaptive sampling approach,[129] the digitization step can be omitted if the interferogram phase signal is used to perform the phase correction using an electronic frequency mixer and if the timing jitter signal is used to define the data acquisition card sampling rate. Finally, the phase and timing jitter information can also be extracted directly from the interferograms themselves.[122,130] In Article IV, I developed a similar numerical algorithm to consider the residual incoherence of our setup by extracting the phase and timing jitter information from the interferograms only.

A further aspect often complicating the experimental DCS setups is that OFCs aren't often readily available in the wavelength region where one would like to perform spectroscopy, such as in the mid-infrared region. A common solution is to convert light from an available region to the target region by using nonlinear optics such as optical parametric oscillators[25,120,131] or difference frequency generation.[25,125] In Article IV, we also used nonlinear optics to transfer light from the 1 µm wavelength region to the 1.5 µm and the mid-infrared (3 µm) regions using a scheme similar to [127]. As a reminder, the mid-infrared beam from such a light source was already used in the PC-FTS work in Article III. Here, two such optical frequency combs were needed to perform dual-comb spectroscopy. Although the mid-infrared beams from these light sources could very well be used to reach the strong fundamental rovibrational bands of selected molecules, in the proof-of-concept demonstration in Article IV, we used the near-infrared beams at the 1.5 µm region to interrogate the $\nu_1 + \nu_3$ combination band of gaseous acetylene. This choice was for the simple reason that for initial characterization of the setup, the 1.5 µm region is much more appealing due to the better availability of high-quality components, optical fibers and detectors.

The main benefit of our approach in Article IV is the simplicity of the experimental setup, as depicted in Figure 13. Basically, we take two 1 µm mode-locked lasers (with slightly different repetition rates) and focus the beam from each into separate periodically-poled, MgO-doped lithium niobate crystals that drive the so-called pulse-trapped, single-pass optical parametric generation process that transfers the light to the 1.5 µm wavelength region.[26,132] Both nonlinear processes are seeded by the same continuous-wave 1.5 µm laser, which acts as a common pre-generated comb tooth for the resulting optical frequency combs. This ensures that the carrier-envelope offset frequency of the generated interferograms is basically zero, meaning that the interferogram phase is almost completely stabilized without the need for any external phase locks. Then, one of the combs propagate through the acetylene gas sample while the other bypasses it. Finally, both combs are combined and sent to a photodetector to digitize the interferograms with a data-acquisition card for further processing.

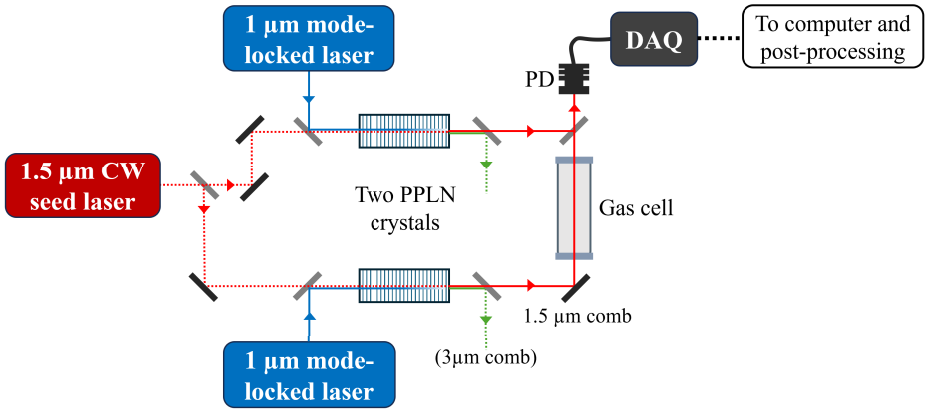

Figure 13: Simplified schematic of the dual-comb setup. PPLN: periodically-poled lithium niobate crystal. PD: photodetector. DAQ: data acquisition card.

Designing the OFC light sources and constructing the dual-comb setup formed the bulk of the thesis work of Mikhail Roiz.[133] The dual-comb setup was later improved by Touko Uotila. All three of us shared ideas, and participated in many of the measurements. That said, my main contribution to the work was designing the interferogram digitization and data processing schemes to yield the final fitted absorption spectra from the raw data. In particular, I developed the numerical algorithm that was used to ensure mutual coherence between the two light sources without the need for phase-locked loops or optical error signals. For that reason, the rest of this space is used to discuss the numerical correction algorithm, and to show the steps taken to produce the final acetylene spectra in Article IV. In the following, I first discuss the numerical algorithm in more detail. Then, I show how the raw dual-comb spectra were processed and fitted to reveal the acetylene absorption. In Appendix A6.1, the discussion on the numerical algorithm is continued: I use the method on synthetic data to prove its performance.

4.1 Numerical post-correction algorithm

The interferogram phase and repetition rate difference corrections have been explained in quite some detail in Supplement 1 of Article IV. Briefly, by analysing the shapes of subsequent interferograms (bursts) in a time window (segment) consisting of multiple such bursts, one can determine a curve that describes the interferogram carrier-envelope phase as a function of time, in another words, during that segment. A complex representation of the segment can be generated via the Hilbert transformation, after which the shapes of the bursts in that segment can be forced to appear equal by multiplying with $\exp(-\mathrm{i}\phi(t))$, where $\phi(t)$ is the determined phase curve. In addition, by analysing the time locations of every burst in the segment, one can determine a curve that describes how the repetition rate difference jitters or drifts as a function of time. With that information, one can resample the segment to make the bursts appear at equidistant intervals, which linearizes the time axis. In that sense, the interferogram phase and timing jitter corrections are conceptually equivalent to the phase- and group-delay corrections in PC-FTS. One important difference is that in the corrections here, one determines only a single, constant phase value per interferogram (burst) in the segment, whereas in PC-FTS, only a single interferogram

(burst) can be measured at a time and the corrected phase (delay) is time dependent throughout that interferogram. These same notions hold also for the timing jitter / group delay corrections.*

It is noteworthy that one can also derive real-time correction signals for both the interferogram phase and timing from beat notes between selected comb teeth and auxiliary lasers.[115,129] In fact, we derived such a signal for the repetition rate difference (as described in Supplement 1 of Article IV), and emulated the adaptive sampling approach[129] by resampling the segments using the digitized optical error signal. We showed that the resulting absorption spectra, when using the numerical corrections versus the optical error signal, were basically identical. Regarding the interferogram phase, only minor fluctuations† remained to be corrected thanks to the inherent mutual coherence of our dual-comb approach (the use of the seed laser); the minor fluctuations are mainly due to having to split the seed laser into two separate arms where optical path difference fluctuations can occur, for instance, from environmental air currents. One easy solution to mitigate this would be to reconstruct the DCS setup inside an air-tight box.

Furthermore, we found that there was no considerable improvement in the spectra if the interferogram phase during segments was corrected, for which reason only the repetition rate difference was corrected for the segments. Instead of correcting the phase during segments, we corrected it between segments. What this means is that due to limitations of the data acquisition card that we used, there was considerable dead time between finishing recording a segment and starting to record a new one (single segment measurement took approx. 1.1 s), during which time the interferogram phase can drift to some extent. For example, during a long-time measurement (~20 min; 1024 segments), the phase between segments drifted less than 2.5 rad, which, however, could already lead to an SNR decrease (the interferogram washing out) if not corrected. Interestingly, due to the dead time, this total measurement time of 20 min corresponds to an effective averaging time of only 82 s. Therefore, there is untapped averaging potential that could be unleashed by improving the data acquisition scheme. The simplest solution would be to invest in a more sophisticated data acquisition card that allows continuous real-time acquisitions. This would also improve the optical frequency accuracy estimated in the preceding section because the light sources would have less time to drift for a given effective averaging time.

Continuing the discussion on real-time measurements, even though the post-correction algorithm used here seems promising, the correction of a single segment can take several seconds, especially if the phase during the segment is corrected. The inherent phase stability, then, was fortunate so that the phase correction was needed only once in a while (*i.e.*, between segments). What made the phase correction slow was the brute force manner in which I implemented it: the phase of a burst is adjusted in a loop until the cross-correlation (which measures the similarity in the burst shapes) between that burst and a reference burst is maximized.[115] It is noteworthy that the carrier envelope phase could also be extracted directly from a given burst.[122,134] However, the method I used simply worked, and for the proof-

*Some minor time dependency during a burst in the corrections here can ensue from interpolating the phase / timing jitter data to consider the phase/timing also in between subsequent burst.

†During a 80 ms long segment, the interferogram phase typically stayed constant within 0.6 rad. Were this drift linear during the segment, it would correspond to a radiofrequency (optical frequency) change of 1.2 Hz (25 kHz).

of-concept demonstration in Article IV, the slowness of the corrections was not a concern.

Another difference between our method and some others found in the literature[122, 134] is that I defined the burst time instances as the maxima of the bursts themselves instead of, *e.g.*, the maxima of the burst envelopes.[122] This is justified in our case where the burst shapes in a segment are basically identical due to the inherent phase stability. This approach has the benefit that it can speed up the repetition rate difference correction as it is faster to find the signal maxima instead of calculating the burst envelopes (for example, by calculating the absolute value of the Hilbert transformation). In the ideal case, there wouldn't be need for correcting even the repetition rate difference. Therefore, the adaptive sampling approach of [129] is appealing, although the technique requires multiple auxiliary lasers and a more complex experimental setup. In Article IV, we also proposed that perhaps the recently demonstrated dual-comb lasers,[122] where the repetition rate difference fluctuations are inherently mitigated, could complement our method. Finally, the corrections performed here can surely be optimized further to push our method towards true real-time measurements.[135] In that sense, the real-time correction averaging scheme of [128] is impressive.

This discussion on the numerical correction algorithm is continued in Appendix A6.1, where I show that the corrections work on synthetic interferograms with added phase and repetition rate fluctuations. In the next section, I will close off this part of the thesis and complete the discussion in Article IV by showing the steps by which the corrected, averaged and Fourier-transformed interferograms, *i.e.*, the raw radiofrequency spectra were processed into the final acetylene absorption spectra.

4.2 Experimental absorption spectra

Figure 14 shows the acetylene dual-comb spectrum, obtained from Fourier-transforming the result from correcting and averaging 1024 segments (each consisting of 937 subsequent bursts). The insets reveal the dual comb structure and the nice-looking sinc instrument lineshape function. The green asterisk indicates the maximum dual-comb peak and the magenta line the portion of data between subsequent comb teeth that was used to calculate the noise standard deviation to define and track the dual-comb SNR as a function of segment averaging number (see Fig. 3 (e) of Article IV).* In addition, one can see the acetylene absorption imprinted on the spectrum outline. According to fits, these correspond to about 12 % acetylene concentration.†

*A detail omitted in the article is that in the SNR analyses, the segments were apodized with a sine lobe. This was to suppress the sinc instrument lineshape function oscillations that started to dominate the noise in the space between adjacent dual-comb peaks, capping the SNR to about 3000 unless the apodization was used.

†There is a mistake in Article IV where we stated that the concentration is 6 %. This mistake is explained in Appendix A6.2.

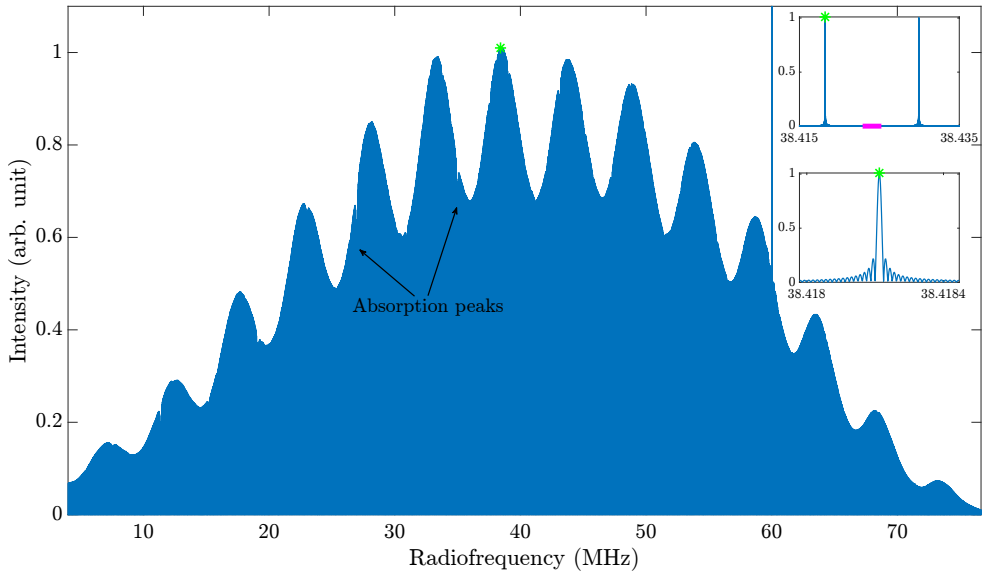

Figure 14: The dual-comb radiofrequency spectrum with acetylene absorption obtained from correcting and averaging 1024 segments (each containing 937 interferograms or bursts in succession). The insets reveal the dual-comb peak structure with the green asterisk illustrating the maximum dual-comb peak, and the magenta line the portion of data between subsequent comb teeth that were used to calculate the noise standard deviation to define the dual-comb peak SNR. The spurious peak at 60 MHz is due to the optical error signal (used to test the emulated adaptive sampling approach) connected to the 2nd channel of the DAQ card leaking also to this channel. The strong etalon effect is due to an optical filter used to limit the optical bandwidth.

To process the data further, the dual-comb peaks in Figure 14 were picked. The precision of peak picking was typically refined by fitting a 2nd order polynomial across a few points around the peak maxima in order to relieve the need for excessive zero-padding prior to FT. It is noteworthy that by resampling the interferogram in a special way[120] one could omit these steps and still find the dual-comb peak values accurately, while significantly decreasing the data size. The peak picking was repeated for a separately measured background spectrum. Then, the radiofrequency axes were scaled to optical frequencies according to Equation (4.1); The ν_0 frequency was determined by measuring the seed laser wavelength with a wavelength meter and refined further in the fitting routine. The repetition rate frequency was provided by the pump laser operating software. The repetition rate difference was obtained from the corrections: the corrections forced the repetition rate difference to a value exactly $1/(85.22\,\mu s) \approx 11.7$ kHz, which was initially the average repetition rate difference for a train of pulses (segment) prior to corrections.

The resulting two peak-picked and frequency axis-scaled spectra are shown in Figure 15. Note that the horizontal axis is flipped compared to Figure 14 due to the seed laser frequency being at a higher optical frequency than the optical spectrum itself. We can see that the acetylene and the background measurement do not match perfectly. This mismatch did not seem to be affected by the corrections, but it was a recurrent problem in our measurements. We suspect the reason is most likely due to detector nonlinearity[78,136] as implied by later tests by Touko Uotila. It also could be that the spectral contents of the combs (comb peak amplitudes) drift during the time that separates the acetylene and background measurements, for example, due to thermal drifts or some other effects typical for nonlinear optics.[132,137] We should

test implementing the scheme, *e.g.*, in [119], where the absorption and background spectra are recorded simultaneously to see if it would improve the match.

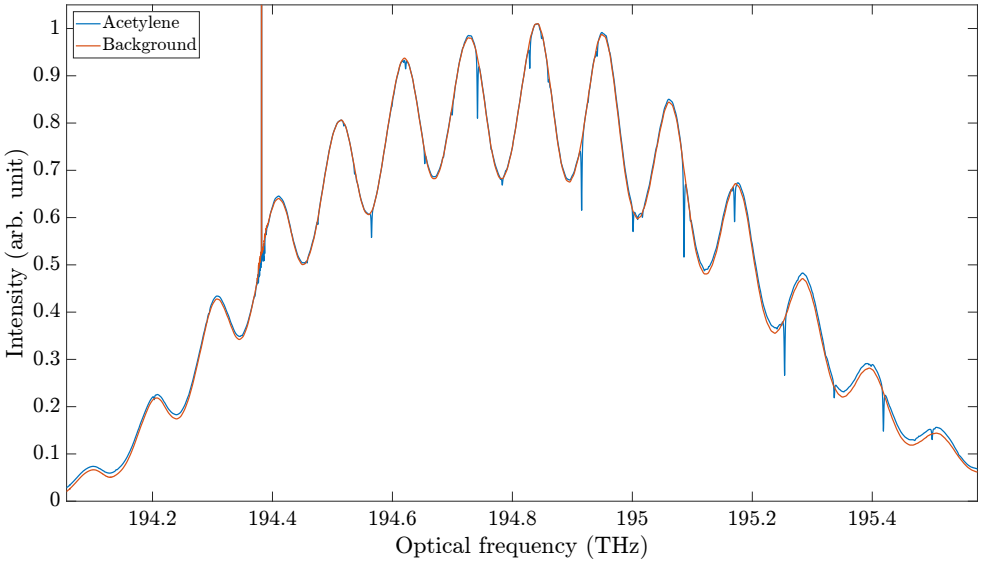

Figure 15: The raw acetylene (and background) spectrum obtained by picking the dual-comb peaks from the spectrum shown in Fig. 14 and by scaling the radiofrequency axis to optical frequencies using Eq. (4.1).

Due to the imperfect matching between the acetylene and background spectra in Figure 15, dividing the acetylene spectrum by the background spectrum will result in a residual background. The residual background was considered using an interesting derivative approach explained in Appendix A6.3. After considering the residual background, we get the final acetylene "transmission" spectrum, shown in Figure 16. Importantly, due to the current asymmetric configuration of the DCS setup where only one of the optical frequency combs propagates through the acetylene sample, the vertical axis of Figure 16 describes the quantity $\exp(-\alpha L/2)$ instead of the transmission $\exp(-\alpha L)$ in the Beer–Lambert law (1.1). This is explained in more detail in Appendix A6.2.

As extra compared to Fig. 4 of Article IV, Figure 16 contains similarly processed spectra but with different amounts of interferogram corrections. We can see that all cases yield basically identical results; the differences are in the per mill level and considered negligible for our purposes. Perhaps in the case of trace gas detection or accurate absorption lineshape parameter determinations, the differences between the different approaches and the discrepancies between the HITRAN database[138] should be reconsidered. Fortunately, the simulations presented in Appendix A6.1 provides a synthetic lab for extensive testing between the different approaches if necessary. In addition, the background correction problem should be solved to allow better comparisons to HITRAN. In any case, the residuals in Figure 16 are excellent. The standard deviation of the residuals is 0.1 %, which value seems typical.[121,130,136,139–141] Calculating the standard deviation of the residuals between 195.31 THz and 195.41 THz results in an SNR of about 500 for the largest acetylene peak, implying a noise-equivalent limit of detection of 250 ppm (noise equivalent absorption $\alpha_{\mathrm{min}} = 1.6 \times 10^{-4}\,\mathrm{cm}^{-1}$; $1024 \times 80\,\mathrm{ms} = 82\,\mathrm{s}$ total effective measurement

time). In addition, the calculated figure of merit (FOM) for our system is 6.9×10^6,* which is in the same order of magnitude as for other high-quality DCS setups (see Table 1 in [142] for a comparison).

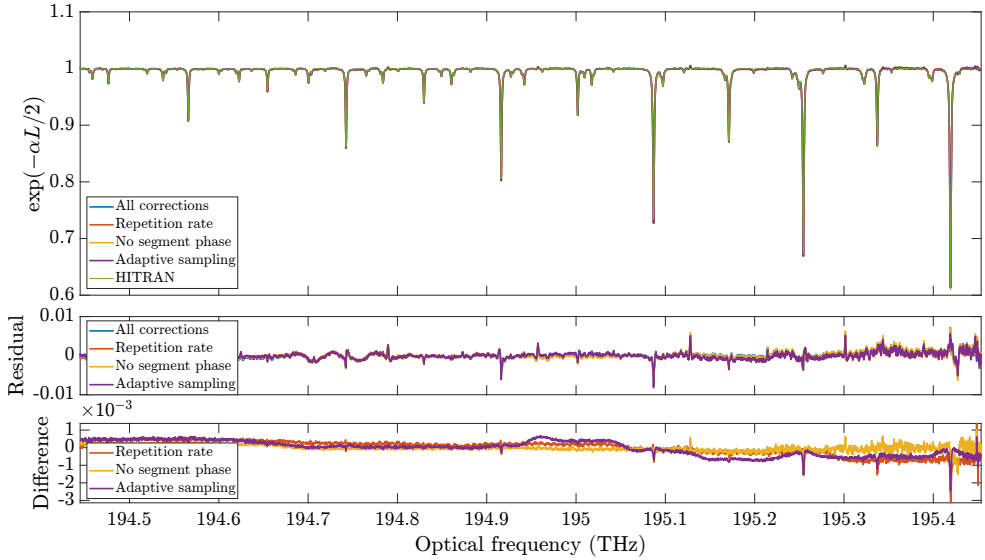

Figure 16: The final background corrected acetylene spectra illustrating the effect of different amounts of interferogram corrections. Note the vertical axis definition of the top panel, which describes a different quantity to the transmission described by the Beer–Lambert law (1.1), as explained in Appendix A6.2. In the legend, "Repetition rate" means correcting the repetition rate difference during segments but not the time dependent phase during segments (but only between segments). "No segment phase" means that the phase correction was not done even between segments (so only the repetition rate difference correction was performed). "All corrections" means performing the time dependent phase correction between but also during segments, in addition to the repetition rate difference correction. "Adaptive sampling" means correcting the repetition rate difference according to the digitized optical error signal (see Article IV) in addition to correcting the phase in between segments (but not during). The middle panel shows respective residuals from HITRAN fits. The lowest panel shows the differences between the differently processed spectra against the "All corrections" one.

*The FOM basically describes the noise performance of a DCS setup in an optical bandwidth and measurement time normalized manner.[136] The larger the FOM is, the less noisy the system is. The FOM here was calculated based on a single spectrum (so without averaging) by calculating the average SNR of the dual-comb peaks basically between the frequency span shown in Fig. 14 (peaks at least 1 % from the maximum peak), by multiplying by the number of dual-comb peaks (5960) and by dividing by the square root of the measurement time ($\sqrt{80\,\mathrm{ms}}$ for the single segment).

5 Rotational-Doppler Spectroscopy

In Article V, a novel type of Fourier-transform spectrometer was proposed. I call the proposed technique rotational-Doppler Fourier-transform spectroscopy (RD-FTS), or vortex-comb spectroscopy (VCS) as in the article. Compared to traditional FTS, the translating mirror of the interferometer is replaced by a rotating mirror, somewhat similar to the PC-FTS work. However, instead of a mirror that tilts back and forth as in PC-FTS, the mirror simply rotates about its surface normal such that the rotation axis is overlapped with the incident beam propagation axis. Therefore, the rotating mirror directly back-reflects the delayed beam with no need for the 4f geometry that is required in PC-FTS to compensate for the beam deflection due to the mirror tilt. A simplified schematic of the RD-FTS setup used in Article V is shown in Figure 17.

In Section 2, traditional FTS was explained by how the light field is delayed in the delay arm compared to a reference beam in the reference arm. An equivalent explanation can be given by considering how the translating mirror shifts each frequency component in the delay arm by a unique amount due to the linear Doppler effect. This alternative description of traditional FTS is given in Appendix A2. The RD-FTS technique can then be viewed as the rotational counterpart of traditional FTS: each frequency component striking the rotating mirror experiences a unique *rotational* Doppler shift. As in traditional FTS, when the frequency-shifted light field is beat against a reference light field, intensity modulation ensues at unique down-converted frequencies, generating the interferogram.

There are, however, some fundamental differences between the two techniques. For one, the frequency shift due to the linear Doppler effect in traditional FTS is proportional to the optical frequency of the light. In RD-FTS, the frequency shift due to the rotational Doppler effect (RDE) is proportional to the amount of orbital angular momentum (OAM) that the frequency component carries (see Fig. 18) – even a white-light source can generate intensity modulation at a single down-converted frequency if all the optical frequencies in the beam have been prepared to carry the same amount of OAM.[143] Therefore, to perform vortex-comb spectroscopy, the frequency components in the incident field have to carry unique amounts of OAM in order to realise the optical frequency-dependent down conversion (see Fig. 17). Interestingly, such light sources already exist in the form of the so-called optical vortex frequency combs, novel light sources only recently demonstrated;[144–146] I briefly comment on these light sources in Section 5.5.

Another difference between traditional FTS and RD-FTS is that in the latter technique, no rotational Doppler-shift is observed in specular reflection from a perfect rotating mirror surface. The reason for this is that the topological charge (meaning, the OAM mode of the beam) does not change in specular reflection:* the rotational Doppler shift is proportional to the change of OAM in the interaction in the same way that the linear Doppler shift is proportional to the change of linear momentum upon reflection. Therefore, instead of a perfect mirror surface, the rotating surface needs

*This statement is elaborated more in the following section. Briefly, a phase flip is expected for a wave that is specularly reflected from a perfect mirror. This also flips the sign of the topological charge. The statement "OAM mode has to change in interaction with the rotating object to observe a rotational Doppler shift" should then be interpreted as deviation from this expected phase flip behaviour.

to have some kind of roughness to generate OAM modes other than the incident one. Here, by an optically rough surface I basically mean a surface whose reflectivity (or sometimes depth) has spatial variability. As reflection from such a surface generally ensues to multiple different OAM modes, multiple rotational Doppler shifts are also present. Despite this, the resulting intensity modulation can be ensured to appear at a single down-converted frequency that is proportional to only the incident OAM mode (and the rotational frequency of the target), if the detection scheme is designed properly (discussed in Section 5.2). In addition, care must be taken to design the surface roughness, or, in our case, the specific shape of the target that modifies the surface reflectivity. This is because only some targets yield intensity modulation for a given input OAM mode (although the frequency of the modulation does not dependent on the shape of the target). In the case of Article V, the target we used is a rectangular slit cut out of white paper and taped onto the rotating mirror surface. The choice for this specific target is explained in detail in Section 5.3.

Even though the behaviour at specular reflection from a perfect mirror surface shows a difference between the linear and rotational Doppler effects, strong analogy between the effects can be established if the rotational Doppler effect is compared to the mature technique called Doppler velocimetry.[147–149] Doppler velocimetry is a means to detect transverse motion relative to an observer by illuminating a rough surface at an angle. Then, a reduced Doppler shift is observed for light scattered to angles other than the one expected for specular reflection. The rotational Doppler effect is, in a way, the rotational counterpart of this effect, as detection of the rotational motion of a target is detection of its (rotational) transverse motion. Incredibly, this rotational motion can be detected in normal illumination of the target as it is the incoming vortex light itself that effectively provides oblique illumination due to the skew of its wavefront, as explained in more detail in the subsequent section.

Until now, the rotational Doppler effect has mainly been used for the detection of the rotational velocity (or rotational direction[150]) of different objects,[151–155] even at the photon-counting level over a long free-space link.[156] Also probing the angular velocity of spinning microparticles[157] has been demonstrated, and measuring the rotation of astronomical objects[158] has been envisioned. In addition to rotation velocity sensing, by analysing the modal composition of the reflected or transmitted light, it is possible to identify the symmetries of the rotating object itself.[159,160] On the other hand, Zhou *et al.* have proposed a complex spectrum analyser to measure the modal composition of OAM-carrying light.[161]

In Article V, we proposed a completely new application for the rotational Doppler effect, namely, the RD-FTS technique that can be used for molecular absorption spectroscopy. In the article, we emulated a vortex-comb light source by using a tunable, single frequency laser prepared to carry a chosen amount of OAM at a time. We successfully measured an absorption feature of gaseous acetylene in the 1 µm wavelength region using a total of 11 OAM modes and constructed the broadband spectrum as if it were measured using an optical vortex comb. In my opinion, the proposed technique is exciting. It offers a completely new way of performing spectroscopy even though it is based on one of the oldest and most well-established spectroscopic techniques, *i.e.*, on Fourier–transform spectroscopy. In addition, the technique relies on the rotational Doppler effect, which, although a phenomenon already known for quite some time,[162] seems to enjoy growing interest. Further still, OAM light or structured light is itself a hot topic in the field of fundamental photonics, with new

papers published basically every day and whole conferences dedicated to that subject only. Even though the main novelty of the proposed RD-FTS technique may lie in its curiosity at this stage, it also offers some potential benefits compared to traditional FTS, if developed further.

One of the benefits of the RD-FTS technique compared to traditional FTS is that high-resolution – even mode-resolved measurements – can be achieved in a short measurement time and with a compact experimental setup. For example, in Article V we achieved an optical resolution of 230 MHz (the mode spacing of the emulated vortex comb) in a measurement time of only a few tens of milliseconds! In contrast, more than 0.65 m long scan lengths, and surely longer measurement times than in RD-FTS, would be required to reach the same resolution when using a traditional FTIR instrument. Compared to PC-FTS, where the optical resolution is limited to only a few GHz, the RD-FTS technique is a clear improvement.

Another benefit of the RD-FTS technique is that the down-conversion relation is of the same form as in phase-controlled FTS or dual-comb spectroscopy (see Fig. 17). This leads to the same kind of speed benefit as demonstrated with PC-FTS in Article III. As an improvement, no phase-delay corrections were required as the optical frequency mapped to the zero down-converted frequency is defined by the optical frequency that does not carry any OAM. In addition, no explicit group-delay correction was needed because we ensured stable rotation by using a commercial rotator with already stable and rotational frequency-precise operation. Compared to the dual-comb work of Article IV, the RD-FTS technique, like PC-FTS, is an auto-correlation method, meaning that the experimental setup is much simplified as there is no need for two fancy light sources that need to have high mutual coherence, but only a single light source is required.

Like in Article III, this new RD-FTS technique was used with CEPAS detection. Whereas the changing scan velocities posed problems in the PC-FTS experiment, the continuous rotation in RD-FTS is definitely an improvement. However, the RD-FTS technique has its own challenges, perhaps the most important of which is the requirement for meticulous optical alignment: imperfect alignment leads to impure down-conversion, which can majorly distort the measured absorption lines. In other words, intensity modulation can appear at down-converted frequencies other than the desired one, which leads to crosstalk. While this issue was mostly ignored in Article V, here (Section 5.4), I discuss it in more detail.

Another drawback of the RD-FTS approach as implemented here is that it may be limited to only narrow optical bandwidths as the modulation depth (strength of the intensity modulation signal) decreases as a function of the OAM mode. Similarly, the beam sizes increase as a function of the OAM mode, possibly leading to practical limitations on the optical bandwidth. Both of these drawbacks were briefly discussed in Article V. Here, that discussion is continued and appended by simulations. In the following, I first explain the origin of the rotational Doppler effect in detail. Then, I focus on some experimental details that were out of scope to be thoroughly explained in the article, such as the target selection, modulation depths, and the crosstalk problem.

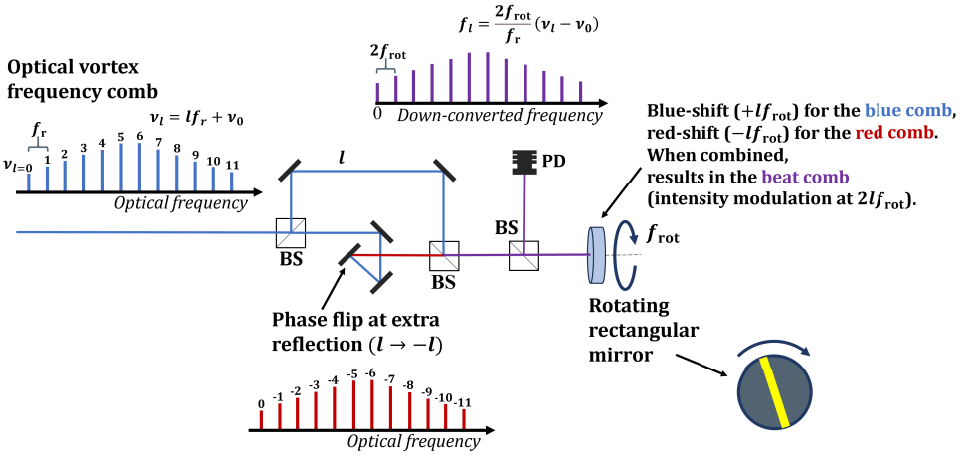

Figure 17: Schematic of the rotational-Doppler FTS approach used in Article V. An optical vortex comb, which is an optical frequency comb with repetition rate f_r but with each optical frequency carrying a distinct number of quanta l of orbital angular momentum, is incident on the experimental setup. Using a beam splitter (BS), the light beam is split into two arms, where an extra reflection flips the topological charge l in one of the arms. The beams are combined and sent onto a rotating target, which is a rectangular mirror in our case. Due to the rotational Doppler effect, each optical frequency is shifted by a unique amount proportional to the topological charge l and the rotational frequency f_{rot}. As a result, a beat comb with repetition rate difference $2f_{rot}$ is generated. This is detected in the usual way for FTS, *i.e.*, by Fourier-transforming the interferogram observed on a photodetector (PD). The strength of the beat signal at each down-converted frequency depends on the shape of the rotating target as discussed at length in Section 5.3.

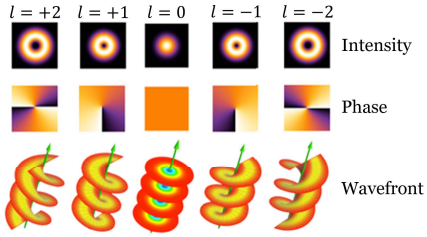

(a) Intensity, phase and the wavefront of a few different order vortex beams.[163]

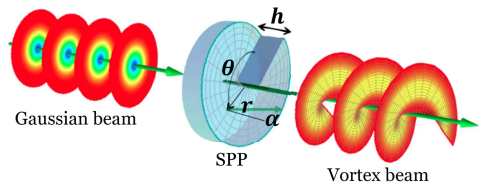

(b) Generation of a vortex beam from a Gaussian beam using a spiral phase plate (SPP).[164] An SPP is an optical component whose thickness h varies as a function of the azimuthal angle θ such that the angular phase of the beam is advanced by $l \times 2\pi$ after one full cycle, thus resulting in a vortex beam with the topological charge l. The angle α illustrates the wavefront skew of the beam relative to the beam propagation direction at the radial distance r.

Figure 18: Illustration of vortex beams. Light fields exhibiting an angular phase $\exp(i\theta l)$ carry $l\hbar$ of OAM per photon. The integer l is also called the topological charge. Vortex beams can be generated using cylindrical lenses or spatial light modulators,[165] angular gratings[166] or spiral phase plates[167] (SPPs). Only SPPs are discussed in this thesis because such optical components were used to generate the OAM-carrying beams in Article V. The electric field of a vortex beam is discussed in Appendix A7.1.

5.1 Rotational Doppler effect

In the preceding section it was said that there is analogy between the linear and rotational Doppler effects. In fact, the rotational Doppler effect can be explained through the linear Doppler effect.[152,168,169] To understand this, let's first consider the case presented in Figure 19a, where a Gaussian beam is incident at an angle α on an optically rough surface. Some of the incident light is reflected to an angle $\beta = -\alpha$ (specular reflection), but some is scattered to a collection of angles β, depending on the surface roughness. In Figure 19a, emphasis is given to the scattering angle $\beta = 0$. If the surface has linear velocity transverse to the surface normal, the incident and scattered fields experience linear Doppler shifts proportional to the velocity components parallel to the beam propagation direction, as illustrated by the vector decomposition shown in Figure 19a. The overall linear Doppler frequency shift is then given by

$$\Delta f_{\text{lin}} = \frac{u}{c}\left[\sin(\alpha) + \sin(\beta)\right]\nu\,, \tag{5.1}$$

where u is the velocity of the surface, c is the speed of light and ν the optical frequency of the light. From this it can be seen that for specular reflection ($\beta = -\alpha$), no overall linear Doppler shift can be detected. This means that one cannot detect transverse motion in the case of a perfect mirror surface, which foreshadows the result that no rotational Doppler shift is generated in the case of reflection from a perfect rotating mirror. Note that the principle presented in Figure 19a is the basis for Doppler velocimetry, a method used to detect linear transverse motion of objects.[147–149]

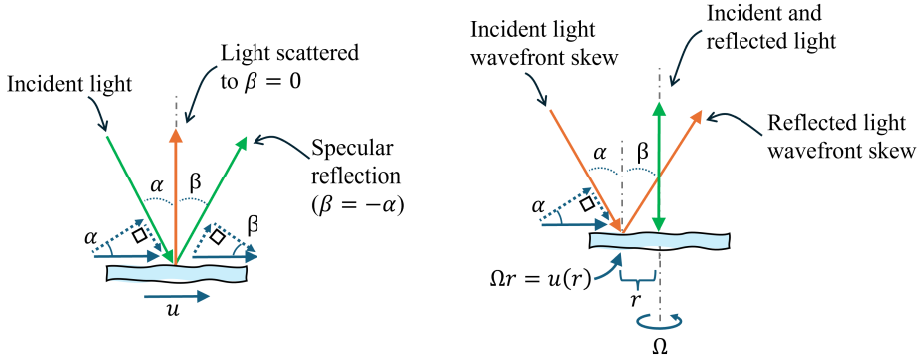

(a) Linear Doppler effect. Incoming light with incident angle α experiences a reduced Doppler frequency shift proportional to the linear velocity u of the target, unless the scattering angle $\beta = -\alpha$ (specular reflection), as given by Eq. (5.1).

(b) Rotational Doppler effect. Vortex light, with Poynting vector skew angle α, incident and reflected along the surface normal (rotational axis of the target) experiences a reduced Doppler shift proportional to the radial velocity u at each radial displacement r, unless the reflected wave skew angle $\beta = -\alpha$ (perfect mirror reflection). Refer to Fig. 18 for an illustration of the vortex beam wavefront skew. Considering the net effect of each skew angle at each radial displacement and radial velocity, the beam experiences an overall frequency shift proportional to the sum of the topological charges of the incident and reflected beams and the angular frequency of the target, as given by Eq. (5.2).

Figure 19: Illustration of the linear and rotational Doppler effects.

The rotational Doppler effect is often explained[152,168] via the notion that because a vortex beam with the wavelength λ has a helical wavefront, its Poynting vector is skewed by an angle $\alpha = l\lambda/(2\pi r)$ relative to the beam propagation direction at each radial distance r from the beam center.[170] This is illustrated in Figure 19b. See also, *e.g.*, the illustrative pictures in [152,168]. It then follows that when a vortex beam with a skew angle α is normally incident on a rotating surface that has an angular frequency Ω, there is a *rotational* Doppler shift if the rotating surface reflects the incident beam to a skew angle β, *i.e.*, if the topological charge is changed from l to m in the process:

$$\begin{aligned}\Delta f_{\mathrm{rot}} &= \frac{r\Omega}{c}\left[\sin\left(\frac{l\lambda}{2\pi r}\right) + \sin\left(\frac{m\lambda}{2\pi r}\right)\right]\nu \\ &\approx \frac{r\Omega}{c}\left[\frac{l\lambda}{2\pi r} + \frac{m\lambda}{2\pi r}\right]\nu \\ &= \frac{\Omega}{2\pi}\left[l+m\right], \end{aligned} \tag{5.2}$$

where at a radial location r the transverse velocity is given by $u(r) = r\Omega$, and where the customary approximation $\sin(\alpha) \approx \alpha$ is made, justified by using large beam sizes compared to the light wavelength λ.[152]

Here I want to properly address the often confusing statement found in literature that the rotational Doppler frequency shift is proportional to the "change of the topological charge" in the interaction process. Often, the two cases of reflection and transmission are considered jointly without a clear distinction. However, it is expected that the phase and therefore the topological charge of a vortex beam is inverted in specular reflection. For example, the so-called vortex doubler[171] is based on this phenomenon: if a Gaussian beam is transmitted through a spiral phase plate (SPP) that increments the topological charge by $+l$ (see Fig. 18b), and if the beam is immediately back-reflected using a mirror to guide it once again through the SPP (which this time decrements the topological charge by $-l$ due to the opposite propagation direction through the component), the resulting topological charge of the beam will be $-2l$ (and not zero) due to the OAM mode inversion in the reflection. Whether the sign changes in reflection is in a way dependent on the choice of coordinates, *i.e.*, whether we observe the light beam from a fixed external coordinate system, or if we attach the coordinate system on the propagating beam and define the positive direction always towards the propagation direction.[27] Here, the latter definition is used.* Therefore, the statement "change of the topological charge in reflection" can be thought as deviation from the expected result that the topological charge is inverted: if the topological charge were not inverted in the process but conserved $l \to l$, then the rotator had had to apply a torque corresponding to $2|l|$ in order to prevent the sign from changing.[27] It is noteworthy that such rotators

*In the context of the vortex doubler, let's first note that a vortex beam is characterized by an azimuthal angle-dependent phase, which can be generated via propagating a Gaussian beam through a spiral-phase plate (SPP), a component whose thickness has angular dependency. Let's say that the SPP gets thinner to the counter-clockwise direction (CCW). Then, the wavefront of the resulting vortex also rotates CCW (less phase delay in this direction). In the back-propagating direction after the reflection, this time the SPP thickens CCW. Because we know that the SPP will not cancel the already generated vortex, the wavefront must rotate CW in this propagation direction. This means that the rotation direction of the vortex has changed in the reflection when viewed from coordinates attached onto the vortex.

exist. For example, Emile *et al.*[172] have successfully observed a rotational Doppler shift in reflection from a right-angle prism, whereas Dholakia *et al.*[162] and Courtial *et al.*[173] have observed it in transmission through a Dove prism. In contrast, rotational Doppler shift cannot be observed from specular reflection from a perfect mirror surface.[27,169] The sign convention in Equation (5.2) is consistent with this result. Unfortunately, in Article V we were not careful enough with the sign convention and the derivations in the supplementary material of Article V may be more appropriate for considering the case of transmission through a rotating object. However, there is no loss of generality in the derivations as one can always replace the dummy index m by another, *e.g.*, $k = -m$. In this thesis, I will keep the notation consistent with the case of reflection, for which purpose the modal decomposition approach used in the supplementary material of Article V is revised later in this section.

An even simpler explanation for the rotational Doppler shift can be given by considering a Gaussian (or a vortex) beam incident on a rotating SPP.[169] The thickness of an SPP varies as a function of the azimuthal angle θ as $\Delta h = \Delta l \theta \lambda/(2\pi)$, such that after one whole cycle, the thickness has changed by Δl times the wavelength λ, thus modifying the phase of the input beam by $\exp(\mathrm{i}\Delta l\theta)$, *i.e.*, changing the OAM content of the incident beam by Δl.[167] If the SPP simultaneously rotates in a time Δt by $\Delta\theta = \Omega\Delta t$, where Ω is the angular frequency of the SPP, the beam accumulates a linear phase ramp $\Delta l\Delta\theta$, meaning that the angular frequency of the beam changes by $\Delta l\Omega$, in addition to the OAM mode change. Note that a spiral phase plate is a transmissive component, but effectively the same result would be obtained by considering a reflective surface whose depth varies accordingly.[169]

The preceding case considers a pure mode converter and a Doppler shift through pure phase modulation. In Article V, the rotating target we used induces only amplitude modulation (*i.e.*, it modifies the reflectivity of the surface). Therefore, an explanation for the rotational Doppler shift in this case is required. Imagine an input mode carrying a helical phase $\exp(\mathrm{i}l\theta)$ incident on a reflective target such as the rectangular mirror used in Article V. Because the target modifies the spatial distribution of the field (assuming the width of the target is smaller than the cross section of the beam), the reflected field must comprise multiple OAM modes. In other words, to construct an electric field with such an amplitude pattern, we require a suitable basis set, such as the Laguerre–Gaussian mode family (see Appendix A7.1), which is the most commonly used mode family to study OAM light. If the reflection changes the OAM mode by the topological charge $\Delta l = k$, it means that the incident field accumulates a phase $\exp(\mathrm{i}k\theta)$. If the reflective pattern simultaneously rotates, the rotation can be considered as a shift of the origin of the azimuthal angle $\theta_0 = \Omega t$.[27,160,174] All in all, the resulting phase of the reflected field is then $\exp(-\mathrm{i}l\theta)\exp(\mathrm{i}k(\theta+\theta_0)) = \exp(\mathrm{i}(k-l)\theta)\exp(\mathrm{i}k\Omega t)$, meaning that the overall topological charge of the reflected field is $m = k - l$ and that there is an accompanying angular frequency shift by $(l+m)\Omega$. Note the phase flip $l \to -l$ in reflection.

Up to this point we have established that when a light beam is incident on a rotating surface, it undergoes a frequency shift if the OAM mode changes in the process. We have also considered the OAM mode and the corresponding frequency change in the case of a pure mode converter that rotates, *e.g.*, a rotating spiral phase plate, which leads to a single rotational Doppler shift. In the case of pure amplitude modulation, the idea of reflection to multiple modes (and thus to multiple different rotational Doppler shifts) was introduced. What is missing is to consider a general rough surface

that rotates, to consider, how that surface can affect the OAM and consequently the frequency content of the beam in reflection. This can be done by expanding on the idea that the surface itself can be thought as a superposition of pure mode converters. The customary approach[152, 156, 169] is to express the effect of the surface roughness by a complex function $\psi(r,\theta)$. This function basically describes how the amplitude and phase of an incident field are modified in reflection, and it can be expressed as a superposition in a suitable basis set. One choice is the Laguerre–Gaussian mode family:

$$\psi(r,\theta) = \sum_{k,p} A_{k,p} LG_p^k(r,\theta)\,, \tag{5.3}$$

where $LG_p^k(r,\theta)$ is a Laguerre–Gaussian mode (see Appendix A7.1) with the topological charge k and number of radial nodes p, and where the complex coefficients $A_{k,p}$ are found by calculating[156]

$$A_{k,p} = \int_0^{2\pi} \int_0^{\infty} [LG_p^k(r,\theta)]^* \psi(r,\theta) r \mathrm{d}r \mathrm{d}\theta\,. \tag{5.4}$$

Equation (5.4) offers an explicit way to study the modal content of a chosen amplitude or phase mask. It is this modal composition of the target that determines to which OAM modes an incident field is reflected to, and, consequently, which rotational Doppler shifts are present in the reflected field. To give an example, Zhang *et al.*[156] have analysed the modal composition of a three-leaf clover target. In that case, the target comprises mostly the fundamental Gaussian mode, but also modes whose topological charges are multiples of three, reflecting the 3-fold symmetry of the target. Similarly, Emile *et al.*[159] have analysed the modal composition of different wedge-shape patterns. In Appendix A7.2, I perform a similar analysis for the rectangular (2-fold symmetry) target used in Article V.

To bridge the gap between the above discussion and the derivations in Article V, I rewrite Equation (5.3) in a more general basis that considers the fact that the rotational Doppler shift depends only on the topological charge k (and not on the radial nodes p), this time including the rotational motion of the target

$$\psi(r,\theta,t) = \sum_k A_k(r) \exp(\mathrm{i}k\theta) \exp(\mathrm{i}k\Omega t)\,. \tag{5.5}$$

When a vortex beam

$$E_i(r,\theta,t) = B(r) \exp(-\mathrm{i}\omega t) \exp(\mathrm{i}l\theta) \tag{5.6}$$

is incident on such a target, the reflected field

$$\begin{aligned} E_r(r,\theta,t) &= E_i(r,-\theta,t)\psi(r,\theta,t) \\ &= B(r) \exp(-\mathrm{i}\omega t) \exp(-\mathrm{i}l\theta) \sum_k A_k(r) \exp(\mathrm{i}k\theta) \exp(\mathrm{i}k\Omega t) \\ &= \sum_k B(r) A_k(r) \exp(-\mathrm{i}\omega t) \exp(\mathrm{i}k\Omega t) \exp(\mathrm{i}[k-l]\theta) \\ &= \sum_m B(r) A_{m+l}(r) \exp(-\mathrm{i}\omega t) \exp(\mathrm{i}[m+l]\Omega t) \exp(\mathrm{i}m\theta)\,, \end{aligned} \tag{5.7}$$

where $m = k-l$ has been identified as the resulting topological charge for the reflected field. This is basically the result given in Article V with the distinction that the sign convention considers better the case of reflection: if reflection ensues to the mode $m = -l$ (*i.e.*, reflection from a perfect mirror surface), no Doppler shift is detected, as expected.

From Equation (5.7) we can see that, indeed, for a general rough surface, an incident vortex (or a Gaussian) beam is reflected to a collection of modes, each having experienced a corresponding rotational Doppler shift. However, to employ the rotational Doppler shift, for example, to experimentally discern the modal composition (or symmetry) of a rotating target, to determine the rotational frequency of a target, or to perform molecular absorption measurements with the proposed RD-FTS technique, one would desire to detect only selected rotational Doppler shifts. This can be ensured by designing the detection scheme suitably, which is the topic of the following section.

5.2 Common detection schemes

Anderson *et al.*[151] have identified two commonly used schemes to detect the rotational Doppler shift. One of them is the "fringe" method, where both an input beam with the topological charge l and a reference beam (typically $-l$) are incident on the rotating target. These beams will experience equal but opposite rotational Doppler shifts so that the intensity modulation will appear at an angular frequency of $\Delta l\Omega = 2l\Omega$, where Ω is the angular frequency of the rotating target.* The other approach is the "heterodyne" method, where only one of the beams strikes the rotating object, after which the Doppler shifted beam is combined with the reference beam. The authors showed that the fringe approach is sensitive only to amplitude modulation (*e.g.*, to variability in the reflectivity of the rotating surface). In contrast, the heterodyne approach is also sensitive to phase modulation (*e.g.*, to variability in the depth of the reflective surface).

5.2.1 Sensitivity to phase modulation

The simplest way to see that the fringe approach is insensitive to phase modulation is to rewrite the complex function that represents the rough surface (Eq. 5.5) as

$$\psi(r,\theta,t) = A(r,\theta,t)\exp(\mathrm{i}\Phi(r,\theta,t))\,, \tag{5.8}$$

where $A(r,\theta,t)$ gives the variation in the reflectivity of the surface, and $\Phi(r,\theta,t)$ in the phase (depth). In the fringe approach, two vortex beams (given by Eq. 5.6) with respective topological charges l_1 and l_2 are incident on the rotating target. As both input beams are modified by the transfer function $\psi(r,\theta,t)$, the resulting reflected

*The name "fringe" stems from the fact that when combining vortex beams with unequal topological charges, interference fringes appear. In particular, when combining the modes l and $-l$, a petal pattern with $2l$ interference fringes is generated (see, *e.g.*, Animation 1 in Section 5.3). The formation of this petal pattern is the basis for the time-domain explanation of the rotational Doppler effect, as called so by Lavery *et al.*:[168] the intensity modulation is generated by the rotating target moving in the intensity distribution.

intensity

$$I(r,\theta,t) = \left| \left[E_i^{l_1}(r,\theta,t) + E_i^{l_2}(r,\theta,t) \right] A(r,\theta,t) \exp(\mathrm{i}\Phi(r,\theta,t)) \right|^2$$
$$= \left| \left[E_i^{l_1}(r,\theta,t) + E_i^{l_2}(r,\theta,t) \right] A(r,\theta,t) \right|^2 , \tag{5.9}$$

meaning that only the amplitude modulation remains.

In contrast, in the heterodyne approach, only one of the input beams strikes the rotating surface:

$$I(r,\theta,t) = \left| E_i^{l_1}(r,\theta,t) A(r,\theta,t) \exp(\mathrm{i}\Phi(r,\theta,t)) + E_i^{l_2}(r,\theta,t) \right|^2 , \tag{5.10}$$

showing that this time also the phase modulation has an effect.

5.2.2 Heterodyne approach

In the following, no further distinction between amplitude and phase modulation is made. To study in more detail at which frequencies the intensity modulation appears in both the heterodyne and the fringe cases, I make use of the modal decomposition view of the transfer function (Eq. 5.5). To derive the intensity modulation in the heterodyne approach, let a vortex beam $E^{l_1}(r,\theta,t)$ be incident on the rotating surface. The reflected beam is then given by Equation (5.7). When the reflected field is beat against a reference beam $E^{l_2}(r,\theta,t)$, the intensity

$$\begin{aligned}
I(r,\theta,t) &= \left| E_i^{l_2}(r,\theta,t) + E_r^{l_1}(r,\theta,t) \right|^2 \\
&= \left| B_{l_2}(r) \exp(-\mathrm{i}\omega t) \exp(\mathrm{i}l_2\theta) + \sum_m B_{l_1}(r) A_{m+l_1}(r) \exp(-\mathrm{i}\omega t) \exp(\mathrm{i}[m+l_1]\Omega t) \exp(\mathrm{i}m\theta) \right|^2 \\
&= |B_{l_2}(r)|^2 + \sum_m |B_{l_1}(r) A_{m+l_1}|^2 \\
&+ \sum_m B_{l_2}(r) B_{l_1}^*(r) A_{m+l_1}^*(r) \exp(-\mathrm{i}[m+l_1]\Omega t) \exp(\mathrm{i}[l_2-m]\theta) + c.c. \\
&= |B_{l_2}(r)|^2 + \sum_m |B_{l_1}(r) A_{m+l_1}|^2 \\
&+ B_{l_2}(r) B_{l_1}^*(r) A_{l_2+l_1}^*(r) \exp(-\mathrm{i}[l_2+l_1]\Omega t) + c.c. \\
&= |B_{l_2}(r)|^2 + \sum_m |B_{l_1}(r) A_{m+l_1}|^2 \\
&+ 2|B_{l_2}(r) B_{l_1}(r) A_{l_1+l_2}(r)| \cos([l_2+l_1]\Omega t + \phi) ,
\end{aligned} \tag{5.11}$$

where $\phi = \mathrm{Angle}[B_{l_2}(r) B_{l_1}^*(r) A_{l_2+l_1}^*(r)]$, and where, like in the supplementary material of Article V, I have omitted the cross-terms between the different reflected modes m as these will integrate to zero along the azimuthal coordinate when the reflected field is focused onto a detector. This is because the detector sees the integral $\int_0^{2\pi} I(r,\theta,t)\mathrm{d}\theta$, but the integrals $\int_0^{2\pi} \exp(\mathrm{i}[m_1-m_2])\mathrm{d}\theta = 0$ unless $m_1 = m_2$. For this same reason, only the term for which $m = l_2$ remains from the sum in the modulation term above.

From Equation (5.11), we can see that the intensity modulation appears at an angular frequency of $[l_1 + l_2]\Omega$. However, unless the target is a pure mode converter to the mode $m = l_2$, the signal strength may be weak because only this single reflected mode is detected. It is also important to note that the intensity modulation disappears if $l_2 = -l_1$ (with the assumption that the topological charge l_1 will be inverted in reflection from the rotating mirror such that the topological charges of the two beams will be the same at the detector). This means that the rotational Doppler shift cannot be detected in an experimental setup that mimics a Michelson interferometer, *i.e.*, where the input beam is split into two arms, back-reflected and combined again such that the reflection in one of the arms happens from the rotating reflective target.* Instead, after splitting the beams but before recombining them, there needs to be an extra reflection between the arms so that $l_2 = l_1$ (so that the topological charges will be unequal after the l_1 mode will be inverted in reflection from the rotating mirror), as illustrated in Figure 20b. This means that even in the heterodyne case the input and reference beams must in a way form a petal pattern that the rotating target then traverses, as illustrated in Appendix A7.3. Note also that the choice $l_2 = l_1$ also maximizes the signal by maximizing the spatial overlap of the radial distributions $B(r)$.[151]

5.2.3 Fringe approach

Let's then derive the fringe case. For input fields $E^{l_1}(r,\theta,t)$ and $E^{l_2}(r,\theta,t)$, the reflected intensity

$$
\begin{aligned}
I(r,\theta,t) &= \left|E_r^{l_1}(r,\theta,t) + E_r^{l_2}(r,\theta,t)\right|^2 \\
&= \Bigg|\sum_m B_{l_1}(r)A_{m+l_1}(r)\exp(-\mathrm{i}\omega t)\exp(\mathrm{i}[m+l_1]\Omega t)\exp(\mathrm{i}m\theta) \\
&+ \sum_m B_{l_2}(r)A_{m+l_2}(r)\exp(-\mathrm{i}\omega t)\exp(\mathrm{i}[m+l_2]\Omega t)\exp(\mathrm{i}m\theta)\Bigg|^2 \\
&= \sum_m |B_{l_1}(r)A_{m+l_1}(r)| + \sum_m |B_{l_2}(r)A_{m+l_2}(r)| \\
&+ \sum_m B_{l_1}(r)A_{m+l_1}(r)B_{l_2}^*(r)A_{m+l_2}^*(r)\exp(\mathrm{i}[l_1-l_2]\Omega t) \\
&= \sum_m |B_{l_1}(r)A_{m+l_1}(r)| + \sum_m |B_{l_2}(r)A_{m+l_2}(r)| \\
&+ 2\sum_m |B_{l_1}(r)A_{m+l_1}(r)B_{l_2}(r)A_{m+l_2}(r)|\cos([l_1-l_2]\Omega t + \phi)\,, \qquad (5.12)
\end{aligned}
$$

where $\phi = \mathrm{Angle}[B_{l_1}(r)A_{m+l_1}(r)B_{l_2}^*(r)A_{m+l_2}^*(r)]$. To maximize the intensity modulation, the best choice for the topological charges of the input fields is $l_2 = -l_1$. This means that if the beam with l_2 is derived from the l_1 beam, its topological charge needs to be inverted to $-l_1$ by an extra reflection before combining the beams and sending them to the rotating target, as illustrated in Figure 20a. Then, intensity modulation is generated at an angular frequency $2\Omega l$. In the supplementary information of Article V this fringe case was derived for a more complex case, where the

*Unless a mode-inverting component such as a cylindrical lens is inserted into the reference arm.[175]

input field consists of multiple optical frequencies, each with a unique topological charge l. It was shown that also in that case the intensity modulation ensues at unique down-converted angular frequencies $2\Omega l$; mixing between the different OAM modes also happen, but those signals appear at high modulation frequencies and can be filtered out. In Appendix A7.4, I complement this more complex case with a numerical simulation to show the appearance of the expected modulation peaks.

In Article V we used the fringe approach instead of the heterodyne method. One reason for this was that it was simply easier to design a target that modifies the reflectance of the mirror instead of the phase (depth): the target we used was a rectangular slit cut out of white paper an taped onto the rotating reflective mirror. The most important reason, however, was that because we used a mechanical rotator, it was practically impossible to completely prevent it from vibrating when it rotated. These vibrations induce signals due to the linear Doppler effect that can easily mask the rotational Doppler shift signals of interest. In contrast, thanks to the fringe approach, these vibrations can be deemed as common noise between the two input beams so that they are eliminated. It is noteworthy, however, that the heterodyne approach may have advantages in some applications. For example, Anderson *et al.*[151] have shown that for random reflective particles in the heterodyne approach, the signal-to-noise ratio increases as the number of particles increases, whereas it decreases for the fringe approach. The expected density of scatterers in the planned RDE application should therefore guide the choice between the detection schemes. Also joint detection of the linear and rotational Doppler effects is possible.[153,158,169]

5.2.4 Mode filter approach

A third commonly used detection method is the use of a mode filter to extract only a certain mode m from the reflected field (*i.e.*, from Eq. 5.7) in order to detect only a single rotational Doppler shift at a time.[152,159,160] An especially interesting approach possibly relevant for RD-FTS is the one used by Gopinath *et al.*[154] The authors demonstrated simultaneous distance and rotational frequency ranging of an object by sending a pulse from a broadband light source through a spatial light modulator (SLM) to make all the optical frequencies carry (the same) OAM mode l. Upon reflection from the target (where a mode flip to $-l$ and no rotational Doppler shift would be expected for reflection from a perfect mirror), light reflected to the original mode l (corresponding to a total topological charge "change" of $2l$) is converted back to a Gaussian beam upon propagating through the SLM in the backward direction, with the result that only that mode is coupled into a single mode fiber and is beat against a reference beam to detect the rotational Doppler shift.

Figure 20c adapts this idea for the RD-FTS technique. We envision that the device in Figure 20c that generates the topological charge l for the input beam could also be a device, perhaps based on a spiral waveguide with an angular grating,[166] that generates an optical vortex comb from an input optical frequency comb such that each optical frequency would then carry distinct amounts of OAM. When the generated optical vortex comb is reflected from the rotating target, the same device could convert each reflected mode l back to the Gaussian mode. Then, upon beating the back-coupled optical frequency comb against the original comb, a down-converted beat spectrum due to the rotational Doppler-effect could be recorded. In the beat spectrum, each beat frequency would correspond to a distinct optical frequency,

allowing vortex comb spectroscopy measurements as proposed in Article V. The benefit of this new approach compared to the fringe approach would be that it could further simplify the experimental setup and relieve the current high requirements for the optical alignment, especially if only the beam interrogating the rotating target would be coupled to free space, but if the beating against the reference comb would be done in fiber. In addition, pumping the vortex comb-generating device with CW light (such that it would then emit only CW light but with a certain topological charge depending on the optical frequency) would allow optimization of the alignment and characterization of the generated beat signals as a function of the input OAM mode, allowing the study of the possible crosstalk problem discussed in Article V. This new approach should be tested and compared against the fringe approach. However, further details on this idea is left to be discussed in future work from collaborators and us; the rest of the discussion in the following sections is dedicated for discussing the fringe approach as used in Article V, starting with optimizing the target selection.

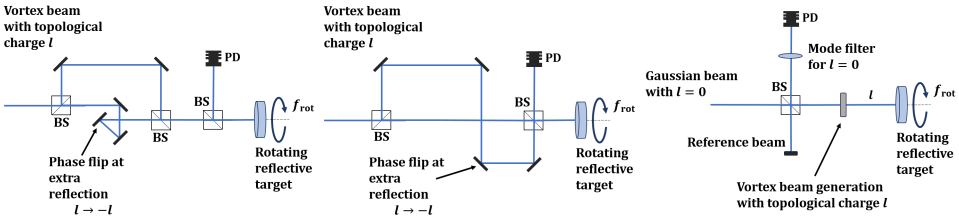

(a) Fringe approach. Incoming vortex beam (or optical vortex comb) is split into two arms and combined again such that an extra reflection in one of the arms inverts the OAM mode in that arm. The combined beams are incident on the rotating target, and reflected light modified by the rotational Doppler effect is gathered and detected on a photodetector (PD).

(b) Heterodyne approach. Only one of the input beams interrogates the rotating target. As in the fringe approach, the topological charge of the reference beam needs to be inverted to observe any rotational Doppler shift upon combining the beams.

(c) Mode filter approach. Only reflection to the original incident OAM mode will convert back to a Gaussian beam and can couple into, say, a single mode fiber, where it can be beat against a reference Gaussian beam.

Figure 20: Comparison of different detection schemes relevant to RD-FTS. Only the fringe approach (a) was used in Article V.

5.3 Target selection and modulation amplitudes

According to Equation (5.12), when an OAM-carrying beam with the topological charge l is incident, together with an OAM-inverted copy of the field ($l \rightarrow -l$), on a target rotating with an angular frequency of Ω, intensity modulation can ensue at an angular frequency of $2l\Omega$. The intuitive explanation for this result is that when combining vortex beams with opposite topological charges, the combined beams form an interference intensity pattern with $2l$ interference fringes such that the intensity modulation is generated when the target traverses this intensity distribution (see Animation 1). Importantly, whatever the shape or positioning of the target on the rotating mirror is, the *frequency* of the modulation will be the same.* However, the choice of target does affect the *amplitude* of the modulation. Indeed, some targets

*Note that while the positioning of the target on the rotating mirror does not affect the modulation frequency, the rotation axis of the mirror needs to be carefully aligned on top of the beam propagation axis to avoid the generation of modulation signals at frequencies other than the desired one.

yield signals for only certain input modes l, but not for others. For RD-FTS, one would like to choose the target such that signals of similar amplitudes are generated for each of the OAM modes in use. Here, I discuss how to choose the target properly, and what kind of modulation amplitudes one can expect.

Anderson *et al.*[151] have derived an analytic expression, reproduced here as Equation (5.13), for the generated intensity modulation signal for the fringe method in the case where the target consists of multiple reflective wedges, each with the same angular width θ_p but different angular locations θ_m.

$$I(t) \propto N\theta_p + \frac{2}{\Delta l} \sin\left(\frac{\Delta l \theta_p}{2}\right) \sum_m^N \cos(\Delta l(\Omega t + \theta_m)) \,, \tag{5.13}$$

where N is the number of reflective wedges, and $\Delta l = 2l$ in our case. The first term describes a DC level on top of which the modulation is added. From this equation, we can already draw some conclusions. The modulation can disappear 1) if the wedges are of an unsuitable width, or 2) if there are multiple wedges whose signals sum up out of phase. For example, for N evenly-spaced wedges, the signal

1) disappears if $\theta_p = \frac{2\pi}{\Delta l}$,
   is maximized when $\theta_p = \frac{\pi}{\Delta l}$,
2) and disappears unless Δl is a multiple of N (as otherwise the N signals add up out of phase).

In other words, for input beams that form an N-petal interference pattern ($N = \Delta l = 2l$), the signal is maximized using a target with N evenly spaced wedges of width π/N. However, such a target would yield no signal for any other input mode l. Examples of a few different cases are illustrated in Animation 1.

Instead of maximizing the signal for a specific OAM mode, we want to ensure similar modulation amplitudes for all the OAM modes in use. This is achieved at least with a target that has two wedges opposite to one another (Animation 1c), which doubles the signal compared to using a single wedge. As the modulation amplitude decreases as a function of the OAM mode (as seen from Eq. 5.13), it is beneficial to optimize the wedge for the largest OAM mode in use (here, $l = 11$). Figure 21 shows the modulation amplitude as a function of the wedge width for the different OAM modes. It can be seen that the easiest choice to ensure similar modulation amplitudes for all the OAM modes is indeed to choose the width to be $\theta_p = \pi/22$, *i.e.*, to optimize the signal for the $l = 11$ mode.

(a) A 4-petal pattern and a target consisting of 4 evenly spaced wedges of width $\pi/4$. This target maximizes the signal for this specific input mode ($l = 2$) but yields no signal for any other mode. However, if the wedges were narrow enough, this target would yield signals for modes $l = 4, 8, 12, ...$, *i.e.*, for multiples of 4.

(b) A 4-petal pattern and a target consisting of 2 evenly spaced wedges of width $\pi/2$. This target yields no signal for this specific input mode ($l = 2$) due to the unsuitable width of the wedges.

(c) A 22-petal pattern ($l = 11$) and a target consisting of 2 evenly spaced wedges of width $\pi/22$. This target yields signals for all the OAM modes used in the experiment ($l = 1, 2, ..., 11$). In addition, the width of the wedges is optimized here for the $l = 11$ mode.

(d) A 22-petal pattern ($l = 11$) and a target that is a 0.3 mm wide rectangle optimized for this specific beam diameter (4 mm): the width of the rectangle corresponds to half of the distance between adjacent intensity maxima, illustrating the target used in the experiments. The target yields signals for all the OAM modes ($l = 1, 2, ..., 11$), however, unlike in panel 1c, the signal amplitude depends on the beam diameter (in addition to the specific OAM mode, see the discussion related to Fig. 22).

Animation 1: Examples of different rotating targets. Note that the text discusses *reflective* wedges and rectangles. Here, the targets *block* the incident light. Using reflective or blocking particles does not affect the amplitude of the modulation, but it does affect the DC level, as seen in Eq. (5.13).

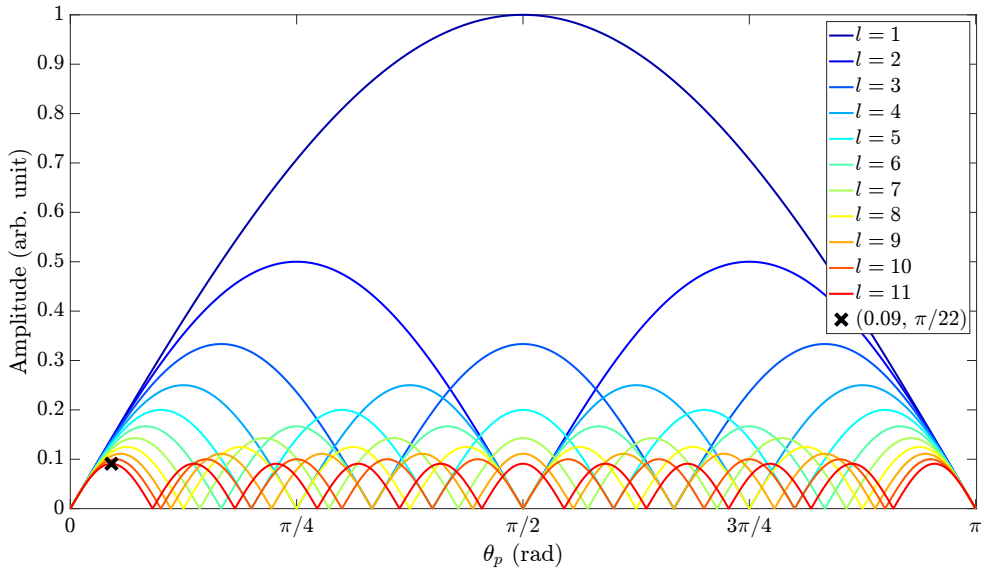

Figure 21: Modulation amplitude for different OAM modes l as a function of the target angular width θ_p. The optimum width for the $l = 11$ mode has been marked with a cross.

Instead of wedges, the target that we opted for in Article V is a rectangle whose width was chosen to be half of the distance between adjacent intensity maxima in the petal pattern when using the $l = 11$ mode (Animation 1d). This target was chosen for the simple reason that it was easier to cut out of paper and tape onto the rotating mirror surface than some other shape, while it should also yield a similar signal strength for the $l = 11$ mode as a wedge would. However, it is noteworthy that the signal amplitude for a given OAM mode is insensitive to the beam diameter when using a wedge as the target, whereas with the rectangle, the width needs to be optimized for the specific beam diameter in use. To study further how the different targets affect the signal amplitudes, I performed some numerical simulations, as presented below.

5.3.1 Modulation amplitude simulation

To simulate the resulting modulation signals when using different targets, input OAM modes and beam diameters, I evaluated the following integral numerically in Matlab at different time steps:

$$I(t,l,D_{|l|}) = \int_{-a}^{a}\int_{-b}^{b} \left|\left[\mathrm{LG}(l,p=0,D_{|l|}) + \mathrm{LG}(-l,p=0,D_{|l|})\right] \times R(t)\right|^2 \mathrm{d}x\mathrm{d}y\,, \quad (5.14)$$

where a and b are some suitable integration limits; where $\mathrm{LG}(l,p=0,D_{|l|})$ is a Laguerre–Gaussian mode with the topological charge l, with the number of radial nodes p set to zero, and with the beam diameter D that depends on l (see Appendix A7.1 for a brief review of the LG modes); and where $R(t)$ is a reflectivity mask that is rotated at each time step. Basically, $R(t)$ is the rotating target as illustrated in Animation 1. The beam diameter D for each mode l is defined as the diameter of the circle that follows the intensity maximum of the beam. The diameters in the simulation are chosen as the beam diameters in the experiment. They range from 1.7 mm for the $l = 1$ mode to 4 mm for the $l = 11$ mode (see Appendix

A7.1). It is noteworthy that in the simulations I assume the fundamental LG modes without radial nodes ($p = 0$). However, as seen in Figure 42 in Appendix A7.1, the experimental beams seem to have nonzero p. This detail is ignored here: I assume that it is still the largest intensity maxima of the petal pattern under consideration that dominate the generated signal even if p were nonzero.

Figure 22 shows the simulated signal amplitudes for each of the OAM modes l using a 2-wedge pattern (the target shown in Animation 1c), and using the rectangular target (Animation 1d). For comparison, I have included the theoretical amplitudes by Anderson *et al.*,[151] *i.e.*, the amplitudes according to Equation (5.13). I have also included the experimental results, both the "ideal" case where no sidebands are generated (meaning signals appearing at wrong modulation frequencies due to imperfect alignment of the setup), and the "realised" amplitudes defined as the height of the main peak in the experimental modulation spectra (an example modulation spectrum is given in Fig. 23; see also Fig. 3 of Article V). The "ideal" case has been considered by summing up all the peaks that emerged in the experimental modulation spectra (if sidebands appear, they redistribute the total signal that ideally should have appeared only under the main peak). We can see that the simulated wedge case matches well with the analytical result, which is expected since the derivation in [151] is based on a similar integral that I have numerically evaluated here; the discrepancies between the results are probably due to numerical imprecisions (*e.g.*, insufficient resolution for the simulated rotating target).

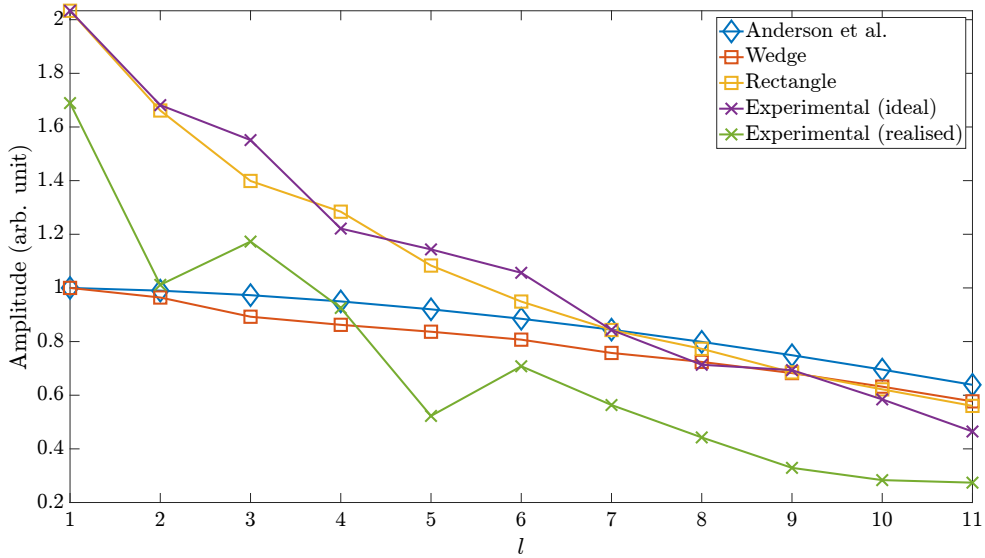

Figure 22: Theoretical (according to Anderson *et al.*[151]), simulated and experimental modulation amplitudes as a function of the OAM mode l. The simulated "wedge" and "rectangle" cases have been normalized such that the wedge case yields the same number for the OAM mode $l = 1$ as the "Anderson *et al.*" case; the experimental cases have been normalized such that the "ideal" experimental case yields the same number for the OAM mode $l = 1$ as the simulated rectangle case. The "ideal" experimental case considers the maximum experimental signal that could have been obtained if the optical alignment of the experimental setup were perfect (see the text).

One result in Figure 22 is that the rectangular target yields basically the same signal strength as the wedge for the $l = 11$ mode, as was expected. However, we can also see that using the rectangle *increases* the signal amplitude for the smaller topological

charges. This is explained by the fact that the smaller l is, the smaller the beam diameter but the wider the petals in the respective petal pattern are. This calls for a wider target to maximize the signal, which is provided by the rectangle whose width does not decrease with decreasing radial distance (unlike with a wedge target). We also see that the ideal experimental signals match very well with the simulation. Unfortunately, due to imperfect alignment of the experimental setup, the sidebands that emerged decreased the realised signals considerably compared to the ideal case.

In any case, the signal amplitudes decrease as the topological charge increases. In the experiment, we emulated an optical vortex comb spanning 11 OAM modes with 0.0078 cm^{-1} wavenumber spacing, which required 12 subsequent measurements to tune the comb across an optical bandwidth of about 1 cm^{-1} to measure the targeted acetylene absorption feature. Ideally, one would want to measure the absorption feature in a single measurement, requiring an optical vortex comb that spans 132 OAM modes to cover the whole 1 cm^{-1} optical bandwidth. According to Equation (5.13), the amplitude for the 132nd mode (when using $\theta_p = \pi/264$) would be less than one percent of the maximum signal that could be obtained when using only the $l = 1$ OAM mode (with $\theta_p = \pi/2$). This effect implies that even if the RD-FTS method based on this current fringe approach implementation (Fig. 17 or 20a) were developed further, its use may be limited to only narrow optical bandwidths. Another practical limit for the optical bandwidth is imposed by the increasing beam diameters as the topological charge increases (see Appendix A7.1).

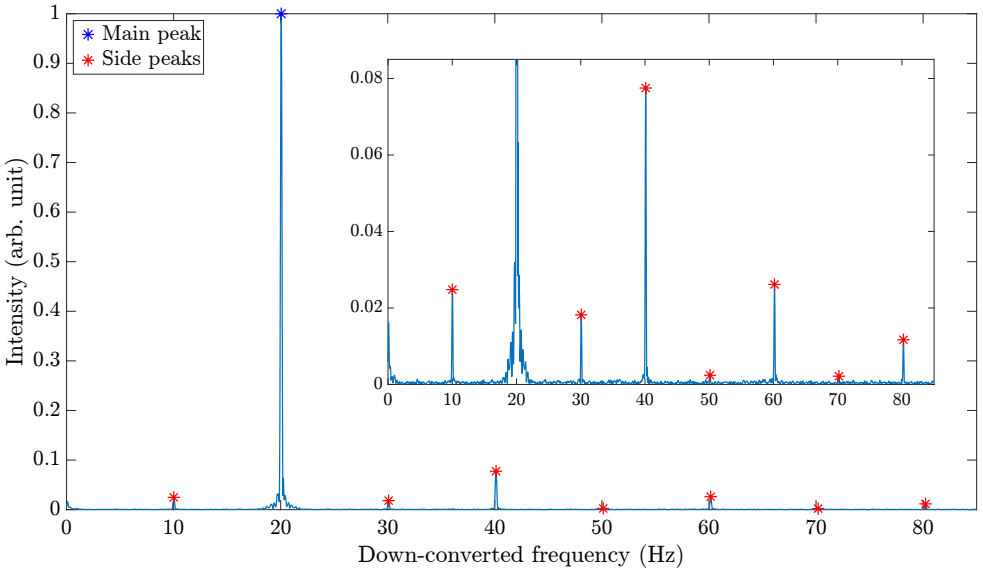

Figure 23: Example of an experimental modulation spectrum, *i.e.*, the Fourier transform of an interferogram measured with a continuous-wave laser beam and with the detection scheme based on the fringe approach (see Fig. 17 or 20a). Here, the OAM mode used is $l = 1$, in which case the modulation peak should appear at 20 Hz (given the rotational frequency of 10 Hz used in the experiments). Due to imperfect alignment of the optical system, also side peaks appear at frequencies other than 20 Hz. Referring to Fig. 22, the "realised" peak amplitude basically means the height of the main peak (blue asterisk); "ideal" means the sum of all peaks (the blue and red asterisks up to 220 Hz).

5.3.2 Modulation contrast

Another detail only briefly discussed in Article V is that also the modulation contrast decreases as a function of l: When the target is attached onto the rotating mirror, a large portion of the total incident power is blocked by the target. When the target rotates, the modulation is introduced on top of the remaining DC level. This is simulated in Figure 24. There, "remaining modulation contrast" is defined as the ratio between the peak-to-peak amplitude of the modulation and the signal maximum. This describes the signal one actually sees on an oscilloscope used to inspect the photodetector signal. "Total modulation depth" means the peak-to-peak amplitude compared against the total power that was incident on the rotating target. One can see that even though the practical modulation contrasts (that will be seen on the oscilloscope) are typically better than 75 %, a large portion of the original incident power has been wasted: the total modulation contrast is only 5 % for the $l = 11$ mode. Even though we did not have any problems with getting strong enough signals on the photodetector in the experiments, for CEPAS detection this poor efficiency is unfortunate as the sensitivity of photoacoustic detection scales with the amplitude of the modulated optical power. We therefore needed to amplify the laser output in order to ensure high enough sensitivity to detect the extremely weak acetylene absorption (~10^{-5} cm^{-1} peak absorption coefficient).

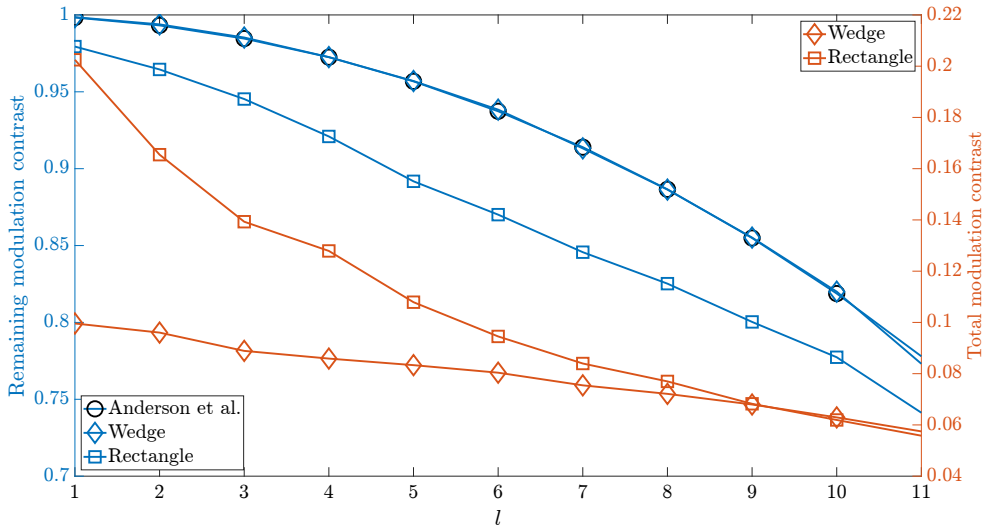

Figure 24: Theoretical (according to Anderson *et al.*[151]) and simulated modulation contrasts as a function of the OAM mode l. "Remaining modulation contrast" means the ratio between the peak-to-peak amplitude of the modulation and the signal maximum in the recorded interferograms. "Total modulation contrast" means the peak-to-peak amplitude compared against the total power that was incident on the rotating target (the target blocks a portion of the incident power on top of which remaining power the modulation is introduced).

5.4 Crosstalk

Imperfect alignment of the optical setup leads to impure down-conversion, which may distort the measured absorption feature. In this section I discuss this crosstalk problem in detail. First, I explain how the experimental setup was aligned, after

which I analyse the purity of the modulation signals observed in the experiment. Finally, I illustrate how the impure down-conversion would distort the absorption feature measured in Article V and propose a correction scheme to retrieve the true underlying absorption feature.

5.4.1 Optical alignment and signal purity

In Article V, we used a collection of spiral phase plates (SPPs) to make a continuous-wave laser beam carry different amounts of OAM: two $l = 1$, one $l = 3$ and one $l = 6$ SPPs were used to generate OAM modes from $l = 1$ up to $l = 11$. The experimental setup was based on the fringe approach and it was typically aligned first without the SPPs by overlapping the beams from the two arms of the interferometer by, on the other hand, overlapping the two spots on an infrared camera, and, on the other, maximizing the interference on the photodetector. Then, the spiral phase plates were put in place one at a time such that the xy-adjustment of each was optimized by looking at the petal pattern on the IR camera, but most importantly, by inspecting the spectrum of the modulation signal and maximizing the peak at the expected modulation frequency. Once the signal with each of the SPPs was satisfactory, I inspected the signal with different combinations of the SPPs. Once in a while, the xy-adjustment of the rotating mirror was optimized. When I managed to get satisfactory signals with all the vortex plates and their combinations, I performed the measurements with the different OAM modes without any further alignment, other than switching between the different SPP combinations: the SPPs were attached to a rack, from which they could be easily slid off and on again without changing their xy-adjustment.

Managing to get good signals (*i.e.*, maximizing the main peak appearing at the expected modulation frequency while minimizing all the side peaks appearing at other frequencies) with all the SPPs and their combinations was difficult. By far the best signals could be obtained with the separate $l = 1$ SPPs, but also with the two in succession. The worst signal was obtained with the $l = 1 + 3 + 6 = 10$ combination, while a good signal was obtained with the $l = 1 + 1 + 3 + 6 = 11$ combination. The reason for this unsystematic behaviour is somewhat unclear, but one of the most likely explanations is simply imperfect alignment of the setup and the many degrees of freedom that affect it. In particular, removing and replacing the SPPs can itself affect the alignment, while any imperfections of the underlying Gaussian beam (such as additional interference fringes from any of the optical components in the experimental setup) can affect the pristinity of the petal pattern. Interestingly, not always did a nice looking petal pattern on the infrared camera yield a good quality modulation signal, and vice versa. For example, the signal quality for the $l = 1$ mode was generally very good (see Table 5) even though the corresponding petal pattern was visually unappealing (see Fig. 42 in Appendix A7.1). Still, it is clear that the RD-FTS technique does rely on the quality of the spatial distribution of the light field, which may make the technique less robust than traditional FTIR.

In the end, I settled with some reasonably good signals with the SPPs and their combinations. This means that all the measurements with the different OAM modes exhibited varying amounts of sideband intensities. Table 5 lists all the peak heights obtained with each of the OAM modes at every even multiple of the rotational frequency.

Table 5: Heights of the main and side peaks for all the OAM modes, when the rotational frequency of the target was 10 Hz. The columns describe the OAM modes, and rows the modulation frequency. For each OAM mode, the values (in the respective column) have been normalized with the respective main peak (the value in the bottom row). All values in the cells are in percent. For example, for the spectrum measured with the OAM $l = 11$ mode (Fig. 3 d of Article V), the largest side peak (at $f_{\mathrm{mod}} = 20$ Hz) is 11.5 % of the main peak (at $f_{\mathrm{mod}} = 220$ Hz). On the other hand, that main peak is 16.2 % of the main peak measured with the OAM $l = 1$ mode.

f_{mod} (Hz)	$l = 1$	2	3	4	5	6	7	8	9	10	11
20	100.0	32.1	3.4	5.6	7.0	3.0	7.9	4.6	6.6	11.5	11.5
40	7.8	100.0	8.7	0.6	9.6	3.0	5.7	6.9	9.4	13.8	8.8
60	2.6	15.4	100.0	5.4	5.6	1.0	1.3	1.3	2.0	4.4	3.7
80	1.2	1.3	6.4	100.0	41.4	2.7	2.0	1.5	2.0	3.2	1.6
100	1.5	0.9	2.4	5.3	100.0	6.1	3.3	2.2	1.9	6.0	1.8
120	0.3	0.2	1.6	3.3	11.4	100.0	3.2	2.2	1.6	1.8	2.2
140	0.3	0.3	0.5	0.8	3.6	11.1	100.0	10.3	4.2	2.7	2.9
160	0.3	0.5	0.3	0.9	2.5	2.8	7.1	100.0	4.7	2.3	3.5
180	0.2	0.5	0.7	0.2	1.2	0.6	2.4	4.4	100.0	2.2	3.2
200	0.2	0.2	0.3	0.2	1.2	0.4	0.6	1.6	25.3	100.0	3.1
220	0.2	0.3	0.3	0.3	0.4	0.4	0.5	0.9	7.4	18.8	100.0
Main	100.0	59.9	69.4	54.8	30.9	41.9	33.4	26.2	19.5	16.8	16.2

5.4.2 Distortion of the absorption feature

The values in Table 5 can be used to simulate the distortion a measured absorption peak would exhibit due to the crosstalk. First, the values can be gathered into a matrix:

$$\begin{pmatrix} b_{l_1} & a_{f_1 l_2} b_{l_2} & a_{f_1 l_3} b_{l_3} & \cdots & a_{f_1 l_{11}} b_{l_{11}} \\ a_{f_2 l_1} b_{l_1} & b_{l_2} & a_{f_2 l_3} b_{l_3} & \cdots & a_{f_2 l_{11}} b_{l_{11}} \\ a_{f_3 l_1} b_{l_1} & a_{f_3 l_2} b_{l_2} & b_{l_3} & \cdots & a_{f_3 l_{11}} b_{l_{11}} \\ \vdots & \vdots & \vdots & \ddots & \vdots \\ a_{f_{11} l_1} b_{l_1} & a_{f_{11} l_2} b_{l_2} & a_{f_{11} l_3} b_{l_3} & \cdots & b_{l_{11}} \end{pmatrix} \tag{5.15}$$

where $a_{f_y l_x}$ describes the efficiency by which the OAM mode l_x yields signal at the modulation frequency f_y, as given in Table 5. The coefficients b_{l_x} describe the signal strength at the main peaks (the bottom row in Table 5).

Let's describe the absorption by a Voigt profile as a vector $(V_{l_1}, \cdots, V_{l_{11}})$, where V_{l_x} describes the absorption at the optical frequency corresponding to the OAM mode l_x. Then, at a given modulation frequency, the overall signal would be

$$\begin{aligned} b_{l_1} V_{l_1} + a_{f_1 l_2} b_{l_2} V_{l_2} + a_{f_1 l_3} b_{l_3} V_{l_3} + \cdots + a_{f_1 l_{11}} b_{l_{11}} V_{l_{11}} &= V_1 \\ a_{f_2 l_1} b_{l_1} V_{l_1} + b_{l_2} V_{l_2} + a_{f_2 l_3} b_{l_3} V_{l_3} + \cdots + a_{f_2 l_{11}} b_{l_{11}} V_{l_{11}} &= V_2 \\ &\vdots \\ a_{f_{11} l_1} b_{l_1} V_{l_1} + a_{f_{11} l_2} b_{l_2} V_{l_2} + a_{f_{11} l_3} b_{l_3} V_{l_3} + \cdots + b_{l_{11}} V_{l_{11}} &= V_{11}\,, \end{aligned} \tag{5.16}$$

where V_y describes the overall signal, including crosstalk, at the modulation frequency f_y. Taking the HITRAN parameters for the targeted acetylene line,[138,176] we can use the above equations to simulate how the distorted absorption line would look like when affected by the crosstalk. The result is given in Figure 25. Basically, I have calculated the vector $(V_1/b_{l_1}, \cdots, V_{11}/b_{l_{11}})$ for each "measurement window" (each

coloured diamond symbol train in the figure indicate a single measurement with the emulated vortex comb) and stitched them together to yield the orange curve. Note the element-wise normalization of the values V by the respective main peak height b. We notice that the simulated absorption peak is indeed distorted due to the crosstalk. The analysis reveals that, on average, less than a third of the total signal at a given modulation frequency $2lf_{\mathrm{rot}}$ emerges from side peaks generated by OAM modes other than the l under consideration. Note that these results correspond to the worst-case scenario, where all the side peak signals would sum up in phase. To know whether the signals in reality sum up in phase would require further theoretical analysis, which is beyond the scope of this thesis.

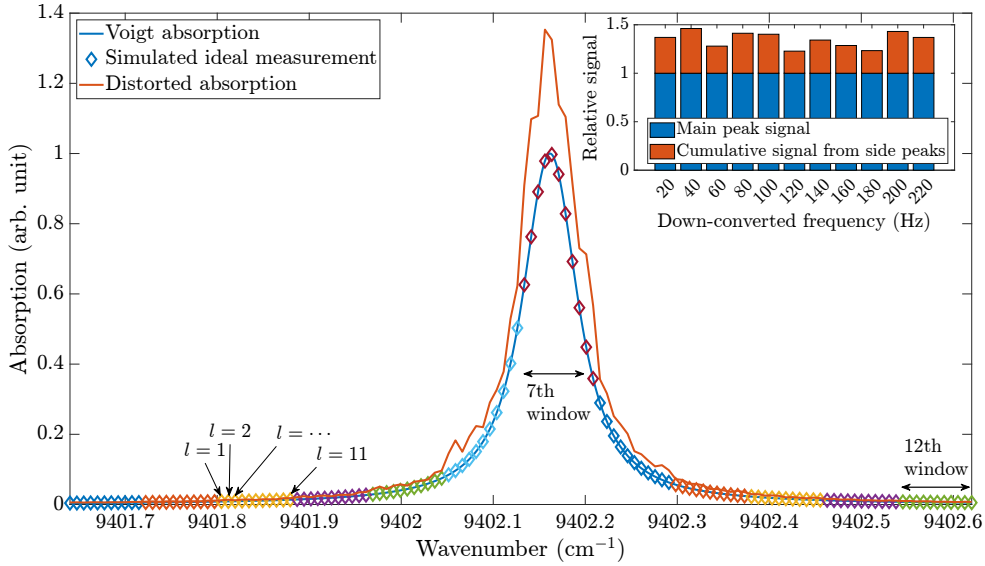

Figure 25: Illustration of how the crosstalk would distort the acetylene absorption line measured in Article V. The blue curve is the true absorption line according to the HITRAN database. The colour-coded diamond symbols indicate ideal measurements (*i.e.*, measurements where no side peaks are present) with the emulated vortex comb at 12 subsequent measurement windows (similar to Fig. 4 c of Article V). The orange curve is the distorted absorption line due to crosstalk. The inset illustrates, in relative units, how much of the total signal at a given modulation frequency is due to contribution from the unwanted side peaks.

5.4.3 Correction method

In principle, if one characterized the generated signals obtained with each of the separate OAM modes, *i.e.*, to get the information shown in Table 5, one could extract the underlying absorption line from the measured, distorted absorption line. Basically, one would simply need to solve the system of linear equations (5.16) for the values V_{l_x}. In the following, I test this approach using the experimental data from the CEPAS acetylene absorption measurements presented in Article V.

To obtain similar data as presented in Table 5, I analysed the spectra of the time domain signals measured with the different OAM modes when the laser was parked on top of the absorption line. As mentioned in the article, the modulation peaks of interest typically lie on top of a noise floor in CEPAS measurements. To consider this, I subtracted from each modulation spectrum a suitable background spectrum

measured at a wavenumber region where there was no acetylene absorption. Only after that did I pick the modulation peak heights and construct the matrix of the form given in (5.15).

Then, for each measurement window, I co-added the 11 modulation spectra measured with the different OAM modes. The co-added spectrum corresponding to the last (12th) measurement window was considered as the background spectrum that was subtracted from each co-added modulation spectra of the other measurement windows. The co-added modulation spectrum corresponding to the 7th measurement window (that corresponds to a measurement at the absorption line) is presented in Figure 26 before subtraction by the background spectrum (that is also presented in the figure).

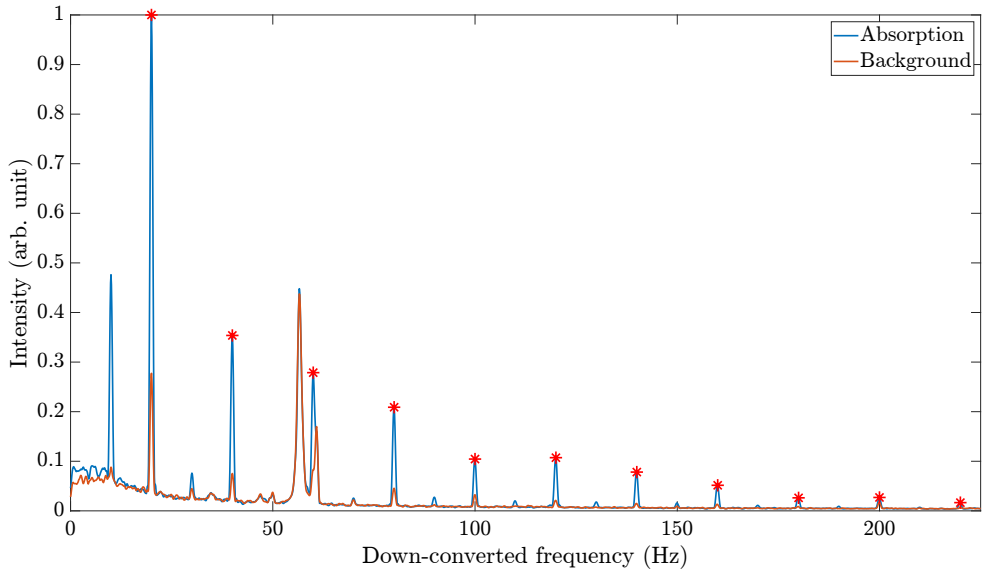

Figure 26: CEPAS modulation spectra obtained by co-adding the 11 modulation spectra measured with the different OAM modes at two different measurement windows: The blue curve corresponds to the 7th measurement window containing most of the acetylene absorption line (see Fig. 25). The orange curve corresponds to the 12th measurement window where there is no acetylene absorption. It is therefore interpreted as the background spectrum. As discussed in the text, this background spectrum was subtracted from the other co-added modulation spectra of the other measurement windows (such as from the blue curve above) before the peak analysis. We see that there is a noticeable noise floor, but also that there are background noise peaks that may leach under the modulation peaks of interest (indicated by the red asterisks). Note that in the background spectrum, there are also clear peaks at the modulation frequencies of interest. These most likely originate from constant window or wall absorption at the CEPAS cell.

Then, for each of the resulting co-added and background subtracted modulation spectra, I picked the peaks at the modulation frequencies (20, 40, ..., 220) Hz. When all such values were obtained for all the measurement windows, the data was stitched together to yield the distorted spectrum presented in Figure 27. Finally, I performed the above-explained correction for the data at each measurement window and stitched the results together to yield the corrected spectrum, also presented in Figure 27. We can see that the correction improves the shape of the absorption line to some extent but that the result is not as good as the ideal case presented in Fig. 4 of Article V, where the crosstalk had no effect in the first place.* I suspect the

*The measurements were performed a single OAM mode at a time such that for each OAM mode,

correction doesn't perform that well mostly due to the noise-floor problem: because the measurements are performed close to the sensitivity limit of the CEPAS detector, the SNRs of the modulation spectra are only modest, and there are background noise peaks leaching under the modulation peaks of interest, as is obvious from Figure 26. The corrections should be tested again with the experimental setup adapted to the 1.5 µm wavelength region where the stronger acetylene absorption would allow high SNR absorption measurements using a photodetector so that we wouldn't need to use CEPAS detection: as seen in Fig. 3 of Article V (or Fig. 23 here), the modulation spectra measured with the photodetector are of high quality, which could potentially lead to better performing corrections.

However, even in the case where the signals that generate the side peaks would sum up in phase to allow the above-discussed corrections, the required characterization measurements would be laborious, especially if larger optical bandwidths (more OAM modes) were targeted. The corrections would require that the device that generates the vortex comb could also be pumped by a tunable continuous-wave light source such that the device would emit OAM-carrying CW light to be used in the characterizations. Even if the corrections could be performed with such a device, the end goal in any case would be to get rid of the side peaks altogether. As speculated in Article V, perhaps the use of an actual vortex comb light source would yield purer signals as all the OAM modes would be emitted from the same device, as opposed to having to remove and replace the SPPs as was done here (*i.e.*, the alignment of the optical setup would remain untouched). Other steps to improve the signal purities would be to opt to use a spatial light modulator as the rotating target. In addition, I wonder if the detection scheme illustrated in Figure 20c could simplify the optical alignment further as there is only one light beam to align (unlike here where there are two beams that need to be carefully overlapped).

the corresponding main peak height was recorded as a function of the laser wavenumber. These measurements were then used to construct an absorption spectrum that mimics a measurement performed using a broadband vortex comb but without the distorting effect of the side peaks.

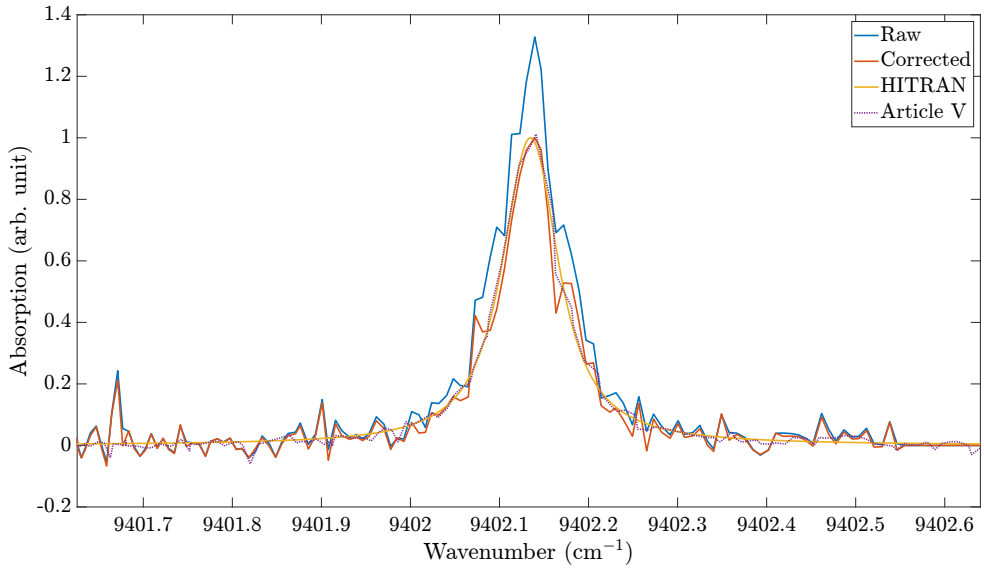

Figure 27: The distorted and corrected experimental spectra. In addition, a HITRAN reference spectrum and the "ideal" experimental spectrum from Article V (where the crosstalk had no effect in the first place) are shown.

5.5 RD-FTS: summary and outlook

Here, I have discussed the rotational-Doppler Fourier-transform spectroscopy technique developed as part of this thesis work in quite some detail. I have discussed the rotational Doppler effect, how the intensity modulation signals are generated in the different detection schemes, and how to optimize the rotating target in the fringe detection case used in Article V. In principle, the RD-FTS technique allows fast, high-resolution measurements without the distorting instrument lineshape function effect. However, it is the crosstalk problem discussed in the preceding section that can distort the measured absorption lines if not properly addressed. Another drawback of the method as implemented here is that it may be limited to only narrow optical bandwidths because the signal strengths decrease and the spot sizes increase as the OAM mode increases (for the estimation of which effects I gave tools in the preceding sections and in Appendix A7.1). Still, this is something that simply needs to be tested experimentally to find out the ultimate practical limits of the technique. To this end, the method should be tested using an actual optical vortex comb with as many OAM modes as possible. It should also be pointed out that the light source itself can limit the available optical bandwidth and even resolution (via the available comb tooth spacing). For example, based on the few articles that have demonstrated optical vortex comb light source development,[144–146] optical vortex combs with a few tens of OAM modes but with large, even THz comb teeth spacings can be currently expected. Obviously, a narrower comb tooth spacing would be desired for molecular absorption spectroscopy to eliminate the need to perform excessive interleaving measurements (meaning measurements where the comb center optical frequency is tuned in steps across several measurement windows). As is usual for science, new applications can drive new developments. To that end, the RD-FTS technique can open up a completely new research avenue to push the development of such light sources towards the needs of absorption spectroscopy.

6 Conclusions

This thesis has made several new contributions to Fourier-transform spectroscopy research either by using FTS to study new molecules, or by developing advanced FTS instrumentation to improve the measurement speed and/or spectral resolution of broadband absorption measurements. Concerning the study of new molecules, in Article II (Section 2.6) we used a traditional Fourier-transform infrared spectrometer to measure and analyse, for the first time, the absorption spectrum of the $H^{36}Cl$ molecule. Our work also inspired other research groups to produce complementary spectroscopic information on this molecule, which information together with ours enable spectroscopic detection of this molecule in future applications. Concerning the development of advanced FTS instrumentation, the new findings can be summarized as follows:

- Article III (Section 3)
  - We successfully combined the phase-controlled FTS technique with cantilever-enhanced photoacoustic spectroscopy and confirmed the results of the previous publications[21,22] that this advanced FTS method leads to fundamentally faster measurements than with conventional FTS. Until now, CEPAS measurements have been unreasonably slow if combined with FTS.
  - I analysed the PC-FTS technique in detail with respect to the design parameters and provided means to estimate its performance (measurement speed, optical bandwidth, spectral resolution, ...) under different design parameter combinations.
  - I emphasized key issues that need to be considered (requirement for a stable, continuous velocity scanner and the need for real-time interferogram corrections) and drawbacks of the technique (increased complexity of the experimental setup, limited spectral resolution) if combined with CEPAS or other detection methods.
- Article IV (Section 4)
  - In recent years, extensive amounts of research has been dedicated to dual-comb spectroscopy. Our contribution was to demonstrate a DCS system that enjoys experimental simplicity due to the use of the infrared optical frequency combs where the shared seed laser ensures inherent stability with respect to the interferogram phase; only minor instabilities needed to be corrected using a numerical post-correction algorithm that I developed.
  - Regarding our research group,[177] the development of a working dual-comb setup was required for future projects we have planned. This has now been realised as part of this thesis work (and, in particular, due to that of [133]).
- Article V (Section 5)
  - This is possibly the most impactful contribution of this thesis. We proposed a completely new approach to FTS (the rotational-Doppler FTS or vortex-comb spectroscopy technique). This technique offers a new application for orbital angular momentum-carrying light sources (interest in

fundamental photonics) but it also offers potential benefits for Fourier-transform absorption spectroscopy (compact experimental setup, fast and high-resolution measurements).

– A bulk of this thesis was used to explain the rotational Doppler effect and the working principle of the proposed spectroscopic technique in detail. Even though the experiments in Article V were based on an emulated vortex comb light source, the extensive simulations presented here support the feasibility of the proposed technique. In addition to the potential benefits of the technique, I also emphasized key issues and limitations that can arise and that need to be studied experimentally in more detail in the future. These include the potential crosstalk problem and the potential optical bandwidth limitations due to the decreasing (increasing) modulation strengths (beam sizes) when using large topological charges.

– To stress the previous point, the proposition of the RD-FTS technique opens up new research avenues or the possibility for future research with respect to the RD-FTS technique itself in terms of its practical limits but also with respect to developing vortex comb light sources that now enjoy from a new application for which they can be used.

References

1. P. J. Brewer, J. S. Kim, S. Lee, O. A. Tarasova, J. Viallon, E. Flores, R. I. Wielgosz, T. Shimosaka, S. Assonov, C. E. Allison, A. M. H. van der Veen, B. Hall, A. M. Crotwell, G. C. Rhoderick, J. T. Hodges, J. Mohn, C. Zellweger, H. Moossen, V. Ebert and D. W. T. Griffith, "Advances in reference materials and measurement techniques for greenhouse gas atmospheric observations", *Metrologia* **56** (2019) 3, 034006, doi:10.1088/1681-7575/ab1506.

2. M. Schmidt, P. Bernath, C. Boone, M. Lecours and J. Steffen, "Trends in atmospheric composition between 2004–2023 using version 5 ACE-FTS data", *J. Quant. Spectrosc. Radiat. Transf.* **325** (2024), 109088, doi:10.1016/j.jqsrt.2024.109088.

3. C. Voigt, P. Jessberger, T. Jurkat, S. Kaufmann, R. Baumann, H. Schlager, N. Bobrowski, G. Giuffrida and G. Salerno, "Evolution of CO_2, SO_2, HCl, and HNO_3 in the volcanic plumes from Etna", *Geophys. Res. Lett.* **41** (2014) 6, 2196–2203, doi:10.1002/2013GL058974.

4. M. Marć, M. Tobiszewski, B. Zabiegała, M. de la Guardia and J. Namieśnik, "Current air quality analytics and monitoring: A review", *Anal. Chim. Acta* **853** (2015), 116–126, doi:10.1016/j.aca.2014.10.018.

5. A. R. J. S. Florentina Villanueva, Milagros Ródenas and M. F. Gabriel, "Sampling and analysis techniques for inorganic air pollutants in indoor air", *Appl. Spectrosc. Rev.* **57** (2022) 7, 531–579, doi:10.1080/05704928.2021.2020807.

6. R. Peng, H. Yoshida, R. A. Chamberlin, T. G. Phillips, D. C. Lis and M. Gerin, "A COMPREHENSIVE SURVEY OF HYDROGEN CHLORIDE IN THE GALAXY", *Astrophys. J.* **723** (2010) 1, 218, doi:10.1088/0004-637X/723/1/218.

7. G. Villanueva, M. Mumma, R. Novak, Y. Radeva, H. Käufl, A. Smette, A. Tokunaga, A. Khayat, T. Encrenaz and P. Hartogh, "A sensitive search for organics (CH_4, CH_3OH, H_2CO, C_2H_6, C_2H_2, C_2H_4), hydroperoxyl (HO_2), nitrogen compounds (N_2O, NH_3, HCN) and chlorine species (HCl, CH_3Cl) on Mars using ground-based high-resolution infrared spectroscopy", *Icarus* **223** (2013) 1, 11–27, doi:10.1016/j.icarus.2012.11.013.

8. B. Henderson, A. Khodabakhsh, M. Metsälä, I. Ventrillard, F. M. Schmidt, D. Romanini, G. A. D. Ritchie, S. te Lintel Hekkert, R. Briot, T. Risby, N. Marczin, F. J. M. Harren and S. M. Cristescu, "Laser spectroscopy for breath analysis: towards clinical implementation", *Appl. Phys. B* **124** (2018) 8, 161, doi:10.1007/s00340-018-7030-x.

9. R. Gorji, J. Skvaril and M. Odlare, "Applications of optical sensing and imaging spectroscopy in indoor farming: A systematic review", *Spectrochim. Acta, Part A* **322** (2024), 124820, doi:10.1016/j.saa.2024.124820.

10. P.-L. Luo, "Long-wave mid-infrared time-resolved dual-comb spectroscopy of short-lived intermediates", *Opt. Lett.* **45** (2020) 24, 6791–6794, doi:10.1364/OL.413754.

11. C. Krafft, I. W. Schie, T. Meyer, M. Schmitt and J. Popp, "Developments in spontaneous and coherent Raman scattering microscopic imaging for biomedical applications", *Chem. Soc. Rev.* **45** (2016), 1819–1849, doi:10.1039/C5CS00564G.

12. J. Lehmuskoski, H. Vasama, J. Hämäläinen, J. Hokkinen, T. Kärkelä, K. Heiskanen, M. Reinikainen, S. Rautio, M. Hirvelä and G. Genoud, "On-Line Monitoring of Radiocarbon Emissions in a Nuclear Facility with Cavity Ring-Down Spectroscopy", *Anal. Chem.* **93** (2021) 48, 16096–16104, doi:10.1021/acs.analchem.1c03814.

13. Z. Wang, Q. Wang, H. Zhang, S. Borri, I. Galli, A. Sampaolo, P. Patimisco, V. L. Spagnolo, P. De Natale and W. Ren, "Doubly resonant sub-ppt photoacoustic gas detection with eight decades dynamic range", *Photoacoustics* **27** (2022), 100387, doi:10.1016/j.pacs.2022.100387.

14. A. D'Arco, T. Mancini, M. C. Paolozzi, S. Macis, L. Mosesso, A. Marcelli, M. Petrarca, F. Radica, G. Tranfo, S. Lupi and G. Della Ventura, "High Sensitivity Monitoring of VOCs in Air through FTIR Spectroscopy Using a Multipass Gas Cell Setup", *Sensors* **22** (2022) 15, doi:10.3390/s22155624.

15. M. Rutkauskas, M. Asenov, S. Ramamoorthy and D. T. Reid, "Autonomous multi-species environmental gas sensing using drone-based Fourier-transform infrared spectroscopy", *Opt. Express* **27** (2019) 7, 9578–9587, doi:10.1364/OE.27.009578.

16. T. Mikkonen, T. Hieta, G. Genty and J. Toivonen, "Sensitive multi-species photoacoustic gas detection based on mid-infrared supercontinuum source and miniature multipass cell", *Phys. Chem. Chem. Phys.* **24** (2022), 19481–19487, doi:10.1039/D2CP01731H.

17. R. Krebbers, N. Liu, K. E. Jahromi, M. Nematollahi, O. Bang, G. Woyessa, C. R. Petersen, G. van Rooij, F. J. M. Harren, A. Khodabakhsh and S. M. Cristescu, "Mid-infrared supercontinuum-based Fourier transform spectroscopy for plasma analysis", *Sci. Rep.* **12** (2022) 1, 9642, doi:10.1038/s41598-022-13787-w.

18. N. Hoghooghi, P. Chang, S. Egbert, M. Burch, R. Shaik, S. A. Diddams, P. Lynch and G. B. Rieker, "GHz repetition rate mid-infrared frequency comb spectroscopy of fast chemical reactions", *Optica* **11** (2024) 6, 876–882, doi:10.1364/OPTICA.521655.

19. M. J. Norahan, R. Horvath, N. Woitzik, P. Jouy, F. Eigenmann, K. Gerwert and C. Kötting, "Microsecond-Resolved Infrared Spectroscopy on Non-repetitive Protein Reactions by Applying Caged Compounds and Quantum Cascade Laser Frequency Combs", *Anal. Chem.* **93** (2021) 17, 6779–6783, doi:10.1021/acs.analchem.1c00666.

20. P. Cacciani, P. Čermák, J. Vander Auwera and A. Campargue, "The ammonia absorption spectrum between 3900 and 4700 cm^{-1}", *J. Quant. Spectrosc. Radiat. Transf.* **277** (2022), 107961, doi:10.1016/j.jqsrt.2021.107961.

21. K. Hashimoto and T. Ideguchi, “Phase-controlled Fourier-transform spectroscopy”, *Nat. Commun* **9** (2018) 1, 4448, doi:10.1038/s41467-018-06956-x.

22. K. Hashimoto, V. R. Badarla and T. Ideguchi, “High-Speed Fourier-Transform Infrared Spectroscopy with Phase-Controlled Delay Line”, *Laser Photonics Rev.* **15** (2021) 1, 2000374, doi:10.1002/lpor.202000374.

23. Y. Yin, D. Ren, C. Li, R. Chen and J. Shi, “Cantilever-enhanced photoacoustic spectroscopy for gas sensing: A comparison of different displacement detection methods”, *Photoacoustics* **28** (2022), 100423, doi:10.1016/j.pacs.2022.100423.

24. J. Karhu, T. Tomberg, F. S. Vieira, G. Genoud, V. Hänninen, M. Vainio, M. Metsälä, T. Hieta, S. Bell and L. Halonen, “Broadband photoacoustic spectroscopy of $^{14}CH_4$ with a high-power mid-infrared optical frequency comb”, *Opt. Lett.* **44** (2019) 5, 1142–1145, doi:10.1364/OL.44.001142.

25. I. Coddington, N. Newbury and W. Swann, “Dual-comb spectroscopy”, *Optica* **3** (2016) 4, 414–426, doi:10.1364/OPTICA.3.000414.

26. M. Roiz and M. Vainio, “Versatile optical frequency combs based on multi-seeded femtosecond optical parametric generation”, *Opt. Express* **30** (2022) 11, 17789–17805, doi:10.1364/OE.456763.

27. O. Emile and J. Emile, “Rotational Doppler Effect: A Review”, *Ann. Phys.* **535** (2023) 11, 2300250, doi:10.1002/andp.202300250.

28. J. M. Hollas, *Modern Spectroscopy*, John Wiley & Sons, 2004, 4th edn.

29. G. Herzberg, *Molecular Spectra and Molecular Structure II. Infrared and Raman Spectra of Polyatomic Molecules*, D. Van Nostrand Company, 1951, 5th edn.

30. P. F. Bernath, *Spectra of Atoms and Molecules*, Oxford University Press, 1995.

31. R. K. Cole, A. S. Makowiecki, N. Hoghooghi and G. B. Rieker, “Baseline-free quantitative absorption spectroscopy based on cepstral analysis”, *Opt. Express* **27** (2019) 26, 37920–37939, doi:10.1364/OE.27.037920.

32. M. Šimečková, D. Jacquemart, L. S. Rothman, R. R. Gamache and A. Goldman, “Einstein A-coefficients and statistical weights for molecular absorption transitions in the HITRAN database”, *J. Quant. Spectrosc. Radiat. Transf.* **98** (2006) 1, 130–155, doi:10.1016/j.jqsrt.2005.07.003.

33. W. Demtröder, *Laser Spectroscopy*, Springer, 1998, 2nd edn.

34. X. Huang and Y. L. Yung, “A Common Misunderstanding about the Voigt Line Profile”, *J. Atmos. Sci.* **61** (2004) 13, 1630–1632, doi:10.1175/1520-0469(2004)061<1630:ACMATV>2.0.CO;2.

35. S. Abrarov and B. Quine, “Efficient algorithmic implementation of the Voigt/-complex error function based on exponential series approximation”, *Appl. Math. Comput.* **218** (2011) 5, 1894–1902, doi:10.1016/j.amc.2011.06.072.

36. J. Tennyson, P. F. Bernath, A. Campargue, A. G. Császár, L. Daumont, R. R. Gamache, J. T. Hodges, D. Lisak, O. V. Naumenko, L. S. Rothman, H. Tran, N. F. Zobov, J. Buldyreva, C. D. Boone, M. D. D. Vizia, L. Gianfrani, J.-M. Hartmann, R. McPheat, D. Weidmann, J. Murray, N. H. Ngo and O. L. Polyansky, "Recommended isolated-line profile for representing high-resolution spectroscopic transitions (IUPAC Technical Report)", *Pure Appl. Chem.* **86** (2014) 12, 1931–1943, doi:10.1515/pac-2014-0208.

37. N. Ngo, D. Lisak, H. Tran and J.-M. Hartmann, "An isolated line-shape model to go beyond the Voigt profile in spectroscopic databases and radiative transfer codes", *J. Quant. Spectrosc. Radiat. Transf.* **129** (2013), 89–100, doi:10.1016/j.jqsrt.2013.05.034.

38. D. Benner, C. P. Rinsland, V. Devi, M. A. H. Smith and D. Atkins, "A multispectrum nonlinear least squares fitting technique", *J. Quant. Spectrosc. Radiat. Transf.* **53** (1995) 6, 705–721, doi:10.1016/0022-4073(95)00015-D.

39. E. M. Adkins and J. T. Hodges, "Assessment of the precision, bias and numerical correlation of fitted parameters obtained by multi-spectrum fits of the Hartmann-Tran line profile to simulated absorption spectra", *J. Quant. Spectrosc. Radiat. Transf.* **280** (2022), 108100, doi:10.1016/j.jqsrt.2022.108100.

40. G. Herzberg, *Molecular Spectra and Molecular Structure I. Spectra of Diatomic Molecules*, D. Van Nostrand Company, 1950, 2nd edn.

41. S. Tashkun, "Global modeling of the $^{12}C^{32}S_2$ line positions within the framework of the non-polyad model of effective Hamiltonian", *J. Quant. Spectrosc. Radiat. Transf.* **279** (2022), 108072, doi:10.1016/j.jqsrt.2022.108072.

42. D. H. Rank, D. P. Eastman, B. S. Rao and T. A. Wiggins, "Rotational and Vibrational Constants of the HCl^{35} and DCl^{35} Molecules*", *J. Opt. Soc. Am.* **52** (1962) 1, 1–7, doi:10.1364/JOSA.52.000001.

43. V. Boudon, C. Richard and L. Manceron, "High-Resolution spectroscopy and analysis of the fundamental modes of $^{28}SiF_4$. Accurate experimental determination of the Si-F bond length", *J. Mol. Spectrosc.* **383** (2022), 111549, doi:10.1016/j.jms.2021.111549.

44. P. Atkins and J. de Paula, *Atkins' Physical Chemistry*, Oxford University Press, 2014, 10th edn.

45. P. Atkins and R. Friedman, *Molecular Quantum Mechanics*, Oxford University Press, 2011, 5th edn.

46. J. A. Coxon and P. G. Hajigeorgiou, "Improved direct potential fit analyses for the ground electronic states of the hydrogen halides: HF/DF/TF, HCl/DCl/TCl, HBr/DBr/TBr and HI/DI/TI", *J. Quant. Spectrosc. Radiat. Transf.* **151** (2015), 133–154, doi:10.1016/j.jqsrt.2014.08.028.

47. J. A. Coxon and P. G. Hajigeorgiou, "The Radial Hamiltonians for the $X1\Sigma^+$ and $B1\Sigma^+$ States of HCl", *J. Mol. Spectrosc.* **203** (2000) 1, 49–64, doi:10.1006/jmsp.2000.8155.

48. T. I. Velichko and S. N. Mikhailenko, "Calculation of the Frequencies of Vibration-Rotation Transitions of the $H^{36}Cl$ Molecule", *Atmos. Oceanic Opt.* **35** (2022) 6, 626–633, doi:10.1134/S1024856022060264.

49. G. Li, I. E. Gordon, R. J. Le Roy, P. G. Hajigeorgiou, J. A. Coxon, P. F. Bernath and L. S. Rothman, "Reference spectroscopic data for hydrogen halides. Part I: Construction and validation of the ro-vibrational dipole moment functions", *J. Quant. Spectrosc. Radiat. Transf.* **121** (2013), 78–90, doi:10.1016/j.jqsrt.2013.02.005.

50. T. I. Velichko and S. N. Mikhailenko, "Analysis of Rotational–Vibrational Transition Frequencies of the HCl Molecule and Its RKR Potentials in the Ground Electronic State", *Opt. Spectrosc.* **125** (2018) 2, 163–172, doi:10.1134/S0030400X18080234.

51. J. L. Dunham, "The Energy Levels of a Rotating Vibrator", *Phys. Rev.* **41** (1932), 721–731, doi:10.1103/PhysRev.41.721.

52. A. A. Marinina, T. I. Velichko and V. I. Perevalov, "The Spectral Line Intensities of the Radioactive Isotopologue $H^{36}Cl$ of the Hydrogen Chloride Molecule", *Atmos. Oceanic Opt.* **36** (2023) 1, 1–6, doi:10.1134/S1024856023020112.

53. R. W. Boyd, *Nonlinear Optics*, Academic Press, 2008, 3rd edn.

54. P. Kluczynski, J. Gustafsson, Åsa M. Lindberg and O. Axner, "Wavelength modulation absorption spectrometry – an extensive scrutiny of the generation of signals", *Spectrochim. Acta Part B At. Spectrosc.* **56** (2001) 8, 1277–1354, doi:10.1016/S0584-8547(01)00248-8.

55. D. Dumitras, D. Dutu, C. Matei, A. Magureanu, M. Petrus and C. Popa, "Laser photoacoustic spectroscopy: principles, instrumentation, and characterization", *J. Optoelectron. Adv. Mater.* **9** (2007), 3655–3701.

56. J. Kauppinen, K. Wilcken, I. Kauppinen and V. Koskinen, "High sensitivity in gas analysis with photoacoustic detection", *Microchem. J.* **76** (2004) 1, 151–159, doi:10.1016/j.microc.2003.11.007.

57. K. Wilcken and J. Kauppinen, "Optimization of a Microphone for Photoacoustic Spectroscopy", *Appl. Spectrosc.* **57** (2003) 9, 1087–1092, https://opg.optica.org/as/abstract.cfm?URI=as-57-9-1087.

58. T. Tomberg, M. Vainio, T. Hieta and L. Halonen, "Sub-parts-per-trillion level sensitivity in trace gas detection by cantilever-enhanced photo-acoustic spectroscopy", *Sci. Rep.* **8** (2018) 1, 1848, doi:10.1038/s41598-018-20087-9.

59. T. Mikkonen, Z. Eslami, G. Genty and J. Toivonen, "Supercontinuum intensity noise coupling in Fourier transform photoacoustic spectroscopy", *Opt. Lett.* **47** (2022) 7, 1713–1716, doi:10.1364/OL.454461.

60. A. A. Kosterev, Y. A. Bakhirkin, R. F. Curl and F. K. Tittel, "Quartz-enhanced photoacoustic spectroscopy", *Opt. Lett.* **27** (2002) 21, 1902–1904, doi:10.1364/OL.27.001902.

61. A. Sampaolo, P. Patimisco, M. Giglio, A. Zifarelli, H. Wu, L. Dong and V. Spagnolo, "Quartz-enhanced photoacoustic spectroscopy for multi-gas detection: A review", *Anal. Chim. Acta* **1202** (2022), 338894, doi:10.1016/j.aca.2021.338894.

62. G. Berden and R. Engeln, eds., *Cavity Ring-Down Spectroscopy: Techniques and Applications*, Blackwell Publishing, 2009.

63. T. P. Hua, Y. R. Sun, J. Wang, A. W. Liu and S. M. Hu, "Frequency metrology of molecules in the near-infrared by NICE-OHMS", *Opt. Express* **27** (2019) 5, 6106–6115, doi:10.1364/OE.27.006106.

64. I. Galli, S. Bartalini, R. Ballerini, M. Barucci, P. Cancio, M. D. Pas, G. Giusfredi, D. Mazzotti, N. Akikusa and P. D. Natale, "Spectroscopic detection of radiocarbon dioxide at parts-per-quadrillion sensitivity", *Optica* **3** (2016) 4, 385–388, doi:10.1364/OPTICA.3.000385.

65. H.-K. Fu, Y.-L. Liu, T.-T. Chen, C.-P. Wang and P.-T. Chou, "The Study of Spectral Correction Algorithm of Charge-Coupled Device Array Spectrometer", *IEEE Trans. Electron Devices* **61** (2014) 11, 3796–3802, doi:10.1109/TED.2014.2358677.

66. S. P. Davis, M. C. Abrams and J. W. Brault, *Fourier Transform Spectrometry*, Academic Press, 2001.

67. W. Herres and J. Gronholz, "Understanding FT-IR Data Processing", *California Institute of Technology, Molecular Materials Resource Center*, https://mmrc.caltech.edu/FTIR/Literature/General/Understanding%20FTIR.pdf, 4.9.2024.

68. P. R. Griffiths, "Fourier Transform Infrared Spectrometry", *Science* **222** (1983) 4621, 297–302, doi:10.1126/science.6623077.

69. A. P. Thorne, "Fourier transform spectrometry in the ultraviolet", *Anal. Chem.* **63** (1991) 2, 57A–65A, doi:10.1021/ac00002a001.

70. P. Connes, "Early history of fourier transform spectroscopy", *Infrared Phys.* **24** (1984) 2, 69–93, doi:10.1016/0020-0891(84)90052-6.

71. H. Ziadi, O. B. Fathallah, I. B. Chouikha, F. K. Tchana, X. Landsheere and H. Aroui, "Line-by-line intensity measurements of methyl fluoride in the ν_2 and ν_5 bands", *J. Quant. Spectrosc. Radiat. Transf.* **286** (2022), 108218, doi:10.1016/j.jqsrt.2022.108218.

72. P. Hardy, C. Richard, V. Boudon, M. V. Khan, L. Manceron and N. Dridi, "High-resolution far-infrared spectroscopy and analysis of the ν_3 and ν_6 bands of chloromethane", *J. Quant. Spectrosc. Radiat. Transf.* **311** (2023), 108779, doi:10.1016/j.jqsrt.2023.108779.

73. J. Mandon, G. Guelachvili and N. Picqué, "Fourier transform spectroscopy with a laser frequency comb", *Nat. Photonics* **3** (2009) 2, 99–102, doi:10.1038/nphoton.2008.293.

74. F. Adler, P. Masłowski, A. Foltynowicz, K. C. Cossel, T. C. Briles, I. Hartl and J. Ye, "Mid-infrared Fourier transform spectroscopy with a broadband frequency comb", *Opt. Express* **18** (2010) 21, 21861–21872, doi:10.1364/OE.18.021861.

75. F. Keilmann, C. Gohle and R. Holzwarth, "Time-domain mid-infrared frequency-comb spectrometer", *Opt. Lett.* **29** (2004) 13, 1542–1544, doi:10.1364/OL.29.001542.

76. P. R. Griffiths and J. A. de Haseth, "Fourier Transform Infrared Spectrometry", in *Chemical Analysis: A Series of Monographs on Anal. Chem. and Its Applications*, eds. P. J. Elving, J. D. Winefordner and I. M. Kolthoff, John Wiley & Sons, 1986, vol. 83.

77. J. Kauppinen and J. Partanen, *Fourier Transforms in Spectroscopy*, Wiley-VCH, 2001, 1st edn.

78. P. Guay, N. B. Hébert, A. Tourigny-Plante, V. Michaud-Belleau and J. Genest, "Correcting photodetector nonlinearity in dual-comb interferometry", *Opt. Express* **29** (2021) 18, 29165–29174, doi:10.1364/OE.435701.

79. R. C. M. Learner, A. P. Thorne and J. W. Brault, "Ghosts and artifacts in Fourier-transform spectrometry", *Appl. Opt.* **35** (1996) 16, 2947–2954, doi:10.1364/AO.35.002947.

80. "resolution", *International Union of Pure Appl. Chem. (IUPAC)*, V.3.0.1, 2019, `https://doi.org/10.1351/goldbook.R05319`, 23.9.2024.

81. R. H. Norton and R. Beer, "New apodizing functions for Fourier spectrometry", *J. Opt. Soc. Am.* **66** (1976) 3, 259–264, doi:10.1364/JOSA.66.000259.

82. R. H. Norton and R. Beer, "Errata: New Apodizing Functions For Fourier Spectrometry", *J. Opt. Soc. Am.* **67** (1977) 3, 419–419, doi:10.1364/JOSA.67.000419.

83. M. L. Forman, W. H. Steel and G. A. Vanasse, "Correction of Asymmetric Interferograms Obtained in Fourier Spectroscopy*", *J. Opt. Soc. Am.* **56** (1966) 1, 59–63, doi:10.1364/JOSA.56.000059.

84. J. W. Brault, "High precision fourier transform spectrometry: The critical role of phase corrections", *Mikrochim. Acta* **93** (1987) 1, 215–227, doi:10.1007/BF01201691.

85. R. C. M. Learner, A. P. Thorne, I. Wynne-Jones, J. W. Brault and M. C. Abrams, "Phase correction of emission line Fourier transform spectra", *J. Opt. Soc. Am. A* **12** (1995) 10, 2165–2171, doi:10.1364/JOSAA.12.002165.

86. N. Picqué and T. W. Hänsch, "Frequency comb spectroscopy", *Nat. Photonics* **13** (2019) 3, 146–157, doi:10.1038/s41566-018-0347-5.

87. A. Foltynowicz, T. Ban, P. Masłowski, F. Adler and J. Ye, "Quantum-Noise-Limited Optical Frequency Comb Spectroscopy", *Phys. Rev. Lett.* **107** (2011), 233002, doi:10.1103/PhysRevLett.107.233002.

88. J. Mandon, G. Guelachvili, N. Picqué, F. Druon and P. Georges, "Femtosecond laser Fourier transform absorption spectroscopy", *Opt. Lett.* **32** (2007) 12, 1677–1679, doi:10.1364/OL.32.001677.

89. H. Timmers, A. Kowligy, A. Lind, F. C. Cruz, N. Nader, M. Silfies, G. Ycas, T. K. Allison, P. G. Schunemann, S. B. Papp and S. A. Diddams, "Molecular fingerprinting with bright, broadband infrared frequency combs", *Optica* **5** (2018) 6, 727–732, doi:10.1364/OPTICA.5.000727.

90. S. Okubo, K. Iwakuni, H. Inaba, K. Hosaka, A. Onae, H. Sasada and F.-L. Hong, "Ultra-broadband dual-comb spectroscopy across 1.0–1.9 µm", *Appl. Phys. Express* **8** (2015) 8, 082402, doi:10.7567/APEX.8.082402.

91. T. W. Hänsch, "Nobel Lecture: Passion for precision", *Rev. Mod. Phys.* **78** (2006), 1297–1309, doi:10.1103/RevModPhys.78.1297.

92. R. Holzwarth, T. Udem, T. W. Hänsch, J. C. Knight, W. J. Wadsworth and P. S. J. Russell, "Optical Frequency Synthesizer for Precision Spectroscopy", *Phys. Rev. Lett.* **85** (2000), 2264–2267, doi:10.1103/PhysRevLett.85.2264.

93. M. Roiz, K. Kumar, J. Karhu and M. Vainio, "Simple method for mid-infrared optical frequency comb generation with dynamic offset frequency tuning", *APL Photonics* **6** (2021) 2, 026103, doi:10.1063/5.0038496.

94. A. Hjältén, M. Germann, K. Krzempek, A. Hudzikowski, A. Głuszek, D. Tomaszewska, G. Soboń and A. Foltynowicz, "Optical frequency comb Fourier transform spectroscopy of $^{14}N_2{}^{16}O$ at 7.8 µm", *J. Quant. Spectrosc. Radiat. Transf.* **271** (2021), 107734, doi:10.1016/j.jqsrt.2021.107734.

95. P. Maslowski, K. F. Lee, A. C. Johansson, A. Khodabakhsh, G. Kowzan, L. Rutkowski, A. A. Mills, C. Mohr, J. Jiang, M. E. Fermann and A. Foltynowicz, "Surpassing the path-limited resolution of Fourier-transform spectrometry with frequency combs", *Phys. Rev. A* **93** (2016), 021802, doi:10.1103/PhysRevA.93.021802.

96. L. Rutkowski, A. C. Johansson, G. Zhao, T. Hausmaninger, A. Khodabakhsh, O. Axner and A. Foltynowicz, "Sensitive and broadband measurement of dispersion in a cavity using a Fourier transform spectrometer with kHz resolution", *Opt. Express* **25** (2017) 18, 21711–21718, doi:10.1364/OE.25.021711.

97. L. Rutkowski, P. Masłowski, A. C. Johansson, A. Khodabakhsh and A. Foltynowicz, "Optical frequency comb Fourier transform spectroscopy with sub-nominal resolution and precision beyond the Voigt profile", *J. Quant. Spectrosc. Radiat. Transf.* **204** (2018), 63–73, doi:10.1016/j.jqsrt.2017.09.001.

98. A. Pine and J. Looney, "N_2 and air broadening in the fundamental bands of HF and HCl", *J. Mol. Spectrosc.* **122** (1987) 1, 41–55, doi:10.1016/0022-2852(87)90217-7.

99. R. Asfin, A. Domanskaya and C. Maul, "Broadening and shifting coefficients of rotation–vibrational lines in the fundamental and first overtone bands of HCl and HBr induced by oxygen and air", *J. Quant. Spectrosc. Radiat. Transf.* **130** (2013), 296–303, doi:10.1016/j.jqsrt.2013.07.014.

100. G. Genoud, J. Lehmuskoski, S. Bell, V. Palonen, M. Oinonen, M.-L. Koskinen-Soivi and M. Reinikainen, "Laser Spectroscopy for Monitoring of Radiocarbon in Atmospheric Samples", *Anal. Chem.* **91** (2019) 19, 12315–12320, doi:10.1021/acs.analchem.9b02496.

101. M. G. Delli Santi, S. Bartalini, P. Cancio, I. Galli, G. Giusfredi, C. Haraldsson, D. Mazzotti, A. Pesonen and P. De Natale, "Biogenic Fraction Determination in Fuel Blends by Laser-Based $^{14}CO_2$ Detection", *Adv. Photonics Res.* **2** (2021) 3, 2000069, doi:10.1002/adpr.202000069.

102. M. G. D. Santi, G. Insero, S. Bartalini, P. Cancio, F. Carcione, I. Galli, G. Giusfredi, D. Mazzotti, A. Bulgheroni, A. I. M. Ferri, R. Alvarez-Sarandes, L. A. de Las Heras, V. Rondinella and P. D. Natale, "Precise radiocarbon determination in radioactive waste by a laser-based spectroscopic technique", *Proc. Natl. Acad. Sci.* **119** (2022) 28, e2122122119, doi:10.1073/pnas.2122122119.

103. K.-H. Ko, Y. Kim, T.-S. Kim, L. Lee and H. Park, "Measurement of $^{14}CO_2$ using off-axis integrated cavity output spectroscopy", *Appl. Phys. B* **128** (2022) 8, 149, doi:10.1007/s00340-022-07864-1.

104. K. Jiao, J. Gao, J. Yang, G. Zhao, Z. Shi, X. Wang, D. Zhu, H. He, J. Qing, X. Yan, W. Ma and S. Jia, "Spectroscopic detection of radiocarbon dioxide based on optical feedback linear cavity enhanced absorption spectroscopy", *Microw. Opt. Technol. Lett.* **66** (2024) 1, e33946, doi:10.1002/mop.33946.

105. W. Kutschera, "Applications of accelerator mass spectrometry", *Int. J. Mass Spectrom.* **349-350** (2013), 203–218, doi:10.1016/j.ijms.2013.05.023.

106. S. Sheppard, L. Johnson, B. Goodwin, J. Tait, D. Wuschke and C. Davison, "Chlorine-36 in nuclear waste disposal – 1. Assessment results for used fuel with comparison to 129I and 14C", *Waste Manag.* **16** (1996) 7, 607–614, doi:10.1016/S0956-053X(97)00001-9.

107. T. Mikkonen, *Fourier Transform Photoacoustic Spectroscopy with Broadband Lasers*, Ph.D. thesis, Tampere University, Tampere, 2023, https://urn.fi/URN:ISBN:978-952-03-2845-0, 20.9.2024.

108. X. Ren, M. Yan, Z. Wen, H. Ma, R. Li, K. Huang and H. Zeng, "Dual-comb quartz-enhanced photoacoustic spectroscopy", *Photoacoustics* **28** (2022), 100403, doi:10.1016/j.pacs.2022.100403.

109. K. Hashimoto, M. Takahashi, T. Ideguchi and K. Goda, "Broadband coherent Raman spectroscopy running at 24,000 spectra per second", *Sci. Rep.* **6** (2016) 1, 21036, doi:10.1038/srep21036.

110. K. D. Thurmond and J. M. Bowlan, "Analysis of Phase-Controlled Fourier Transform Spectroscopy Operation in the Mid- and Far-Infrared", in *Optical Sensors and Sensing Congress 2022 (AIS, LACSEA, Sensors, ES)*, Optica Publishing Group, 2022, LTu3B.2, https://opg.optica.org/abstract.cfm?URI=LACSEA-2022-LTu3B.2.

111. J. Peatross and M. Ware, *Physics of Light and Optics*, Brigham Young University, 2014, https://optics.byu.edu/, 21.9.2024.

112. I. Coddington, W. C. Swann and N. R. Newbury, "Coherent dual-comb spectroscopy at high signal-to-noise ratio", *Phys. Rev. A* **82** (2010), 043817, doi:10.1103/PhysRevA.82.043817.

113. J. W. Brault, "New approach to high-precision Fourier transform spectrometer design", *Appl. Opt.* **35** (1996) 16, 2891–2896, doi:10.1364/AO.35.002891.

114. P. Giaccari, J.-D. Deschênes, P. Saucier, J. Genest and P. Tremblay, "Active Fourier-transform spectroscopy combining the direct RF beating of two fiber-based mode-locked lasers with a novel referencing method", *Opt. Express* **16** (2008) 6, 4347–4365, doi:10.1364/OE.16.004347.

115. J.-D. Deschênes, P. Giaccari and J. Genest, "Optical referencing technique with CW lasers as intermediate oscillators for continuous full delay range frequency comb interferometry", *Opt. Express* **18** (2010) 22, 23358–23370, doi:10.1364/OE.18.023358.

116. S. Markmann, M. Franckié, M. Bertrand, M. Shahmohammadi, A. Forrer, P. Jouy, M. Beck, J. Faist and G. Scalari, "Frequency chirped Fourier-Transform spectroscopy", *Commun. Phys* **6** (2023) 1, 53, doi:10.1038/s42005-023-01157-5.

117. L. A. Sterczewski and M. Bagheri, "Sub-Nominal Resolution Fourier Transform Spectrometry with Chip-Based Combs", *Laser Photonics Rev.* **18** (2024) 4, 2300724, doi:10.1002/lpor.202300724.

118. S. Schiller, "Spectrometry with frequency combs", *Opt. Lett.* **27** (2002) 9, 766–768, doi:10.1364/OL.27.000766.

119. I. Coddington, W. C. Swann and N. R. Newbury, "Coherent Multiheterodyne Spectroscopy Using Stabilized Optical Frequency Combs", *Phys. Rev. Lett.* **100** (2008), 013902, doi:10.1103/PhysRevLett.100.013902.

120. A. V. Muraviev, D. Konnov and K. L. Vodopyanov, "Broadband high-resolution molecular spectroscopy with interleaved mid-infrared frequency combs", *Sci. Rep.* **10** (2020) 1, 18700, doi:10.1038/s41598-020-75704-3.

121. Z. Chen, M. Yan, T. W. Hänsch and N. Picqué, "A phase-stable dual-comb interferometer", *Nat. Commun* **9** (2018) 1, 3035, doi:10.1038/s41467-018-05509-6.

122. C. R. Phillips, B. Willenberg, A. Nussbaum-Lapping, F. Callegari, S. L. Camenzind, J. Pupeikis and U. Keller, "Coherently averaged dual-comb spectroscopy with a low-noise and high-power free-running gigahertz dual-comb laser", *Opt. Express* **31** (2023) 5, 7103–7119, doi:10.1364/OE.479356.

123. T. Ideguchi, T. Nakamura, Y. Kobayashi and K. Goda, "Kerr-lens mode-locked bidirectional dual-comb ring laser for broadband dual-comb spectroscopy", *Optica* **3** (2016) 7, 748–753, doi:10.1364/OPTICA.3.000748.

124. S. Mehravar, R. A. Norwood, N. Peyghambarian and K. Kieu, "Real-time dual-comb spectroscopy with a free-running bidirectionally mode-locked fiber laser", *Appl. Phys. Lett.* **108** (2016) 23, 231104, doi:10.1063/1.4953400.

125. F. C. Cruz, D. L. Maser, T. Johnson, G. Ycas, A. Klose, F. R. Giorgetta, I. Coddington and S. A. Diddams, "Mid-infrared optical frequency combs based on difference frequency generation for molecular spectroscopy", *Opt. Express* **23** (2015) 20, 26814–26824, doi:10.1364/OE.23.026814.

126. S. Vasilyev, A. Muraviev, D. Konnov, M. Mirov, V. Smolski, I. Moskalev, S. Mirov and K. Vodopyanov, "Longwave infrared (6.6–11.4 µm) dual-comb spectroscopy with 240,000 comb-mode-resolved data points at video rate", *Opt. Lett.* **48** (2023) 9, 2273–2276, doi:10.1364/OL.477346.

127. C. Gu, Z. Zuo, D. Luo, Z. Deng, Y. Liu, M. Hu and W. Li, "Passive coherent dual-comb spectroscopy based on optical-optical modulation with free running lasers", *PhotoniX* **1** (2020) 1, 7, doi:10.1186/s43074-020-0005-2.

128. J. Roy, J.-D. Deschênes, S. Potvin and J. Genest, "Continuous real-time correction and averaging for frequency comb interferometry", *Opt. Express* **20** (2012) 20, 21932–21939, doi:10.1364/OE.20.021932.

129. T. Ideguchi, A. Poisson, G. Guelachvili, N. Picqué and T. W. Hänsch, "Adaptive real-time dual-comb spectroscopy", *Nat. Commun* **5** (2014) 1, 3375, doi:10.1038/ncomms4375.

130. N. B. Hébert, J. Genest, J.-D. Deschênes, H. Bergeron, G. Y. Chen, C. Khurmi and D. G. Lancaster, "Self-corrected chip-based dual-comb spectrometer", *Opt. Express* **25** (2017) 7, 8168–8179, doi:10.1364/OE.25.008168.

131. A. V. Muraviev, V. O. Smolski, Z. E. Loparo and K. L. Vodopyanov, "Massively parallel sensing of trace molecules and their isotopologues with broadband subharmonic mid-infrared frequency combs", *Nat. Photonics* **12** (2018) 4, 209–214, doi:10.1038/s41566-018-0135-2.

132. A. V. Gorbach, M. Roiz, M. Vainio and D. V. Skryabin, "Trapping of ultrashort pulses in nondegenerate parametric conversion", *Phys. Rev. A* **107** (2023), 063515, doi:10.1103/PhysRevA.107.063515.

133. M. Roiz, *Optical frequency comb based light sources for advanced spectroscopy applications*, Ph.D. thesis, University of Helsinki, Helsinki, 2024, `http://hdl.handle.net/10138/574198`, 17.9.2024.

134. H. Tian, R. Li, T. Endo, T. Kato, A. Asahara, L. A. Sterczewski and K. Minoshima, "Dual-comb spectroscopy using free-running mechanical sharing dual-comb fiber lasers", *Appl. Phys. Lett.* **121** (2022) 21, 211104, doi:10.1063/5.0125689.

135. S. M. Bresler, D. A. Long, B. J. Reschovsky, Y. Bao, T. W. LeBrun and J. J. Gorman, "GPU-enabled real-time optical frequency comb spectroscopy and a photonic readout", *Opt. Lett.* **48** (2023) 22, 5887–5890, doi:10.1364/OL.501847.

136. P. Guay, M. Walsh, A. Tourigny-Plante and J. Genest, "Linear dual-comb interferometry at high power levels", *Opt. Express* **31** (2023) 3, 4393–4404, doi:10.1364/OE.481671.

137. M. Vainio, J. Peltola, S. Persijn, F. J. M. Harren and L. Halonen, "Thermal effects in singly resonant continuous-wave optical parametric oscillators", *Appl. Phys. B* **94** (2009) 3, 411–427, doi:10.1007/s00340-008-3287-9.

138. I. Gordon, L. Rothman, R. Hargreaves, R. Hashemi, E. Karlovets, F. Skinner, E. Conway, C. Hill, R. Kochanov, Y. Tan, P. Wcisło, A. Finenko, K. Nelson, P. Bernath, M. Birk, V. Boudon, A. Campargue, K. Chance, A. Coustenis, B. Drouin, J. Flaud, R. Gamache, J. Hodges, D. Jacquemart, E. Mlawer, A. Nikitin, V. Perevalov, M. Rotger, J. Tennyson, G. Toon, H. Tran, V. Tyuterev, E. Adkins, A. Baker, A. Barbe, E. Canè, A. Császár, A. Dudaryonok, O. Egorov, A. Fleisher, H. Fleurbaey, A. Foltynowicz, T. Furtenbacher, J. Harrison, J. Hartmann, V. Horneman, X. Huang, T. Karman, J. Karns, S. Kassi, I. Kleiner, V. Kofman, F. Kwabia–Tchana, N. Lavrentieva, T. Lee, D. Long, A. Lukashevskaya, O. Lyulin, V. Makhnev, W. Matt, S. Massie, M. Melosso, S. Mikhailenko, D. Mondelain, H. Müller, O. Naumenko, A. Perrin, O. Polyansky, E. Raddaoui, P. Raston, Z. Reed, M. Rey, C. Richard, R. Tóbiás, I. Sadiek, D. Schwenke, E. Starikova, K. Sung, F. Tamassia, S. Tashkun, J. Vander Auwera, I. Vasilenko, A. Vigasin, G. Villanueva, B. Vispoel, G. Wagner, A. Yachmenev and S. Yurchenko, "The HITRAN2020 molecular spectroscopic database", *J. Quant. Spectrosc. Radiat. Transf.* **277** (2022), 107949, doi:10.1016/j.jqsrt.2021.107949.

139. A. Parriaux, K. Hammani, C. Thomazo, O. Musset and G. Millot, "Isotope ratio dual-comb spectrometer", *Phys. Rev. Res.* **4** (2022), 023098, doi:10.1103/PhysRevResearch.4.023098.

140. Z. Zuo, C. Gu, D. Peng, X. Zou, Y. Di, L. Zhou, D. Luo, Y. Liu and W. Li, "Broadband mid-infrared molecular spectroscopy based on passive coherent optical–optical modulated frequency combs", *Photon. Res.* **9** (2021) 7, 1358–1368, doi:10.1364/PRJ.422397.

141. T. Voumard, J. Darvill, T. Wildi, M. Ludwig, C. Mohr, I. Hartl and T. Herr, "1-GHz dual-comb spectrometer with high mutual coherence for fast and broadband measurements", *Opt. Lett.* **47** (2022) 6, 1379–1382, doi:10.1364/OL.448575.

142. T. Uotila, *Passively coherent dual-comb spectrometer for gas thermometry*, Master's thesis, University of Helsinki, Helsinki, 2024, `http://hdl.handle.net/10138/577540`, 18.9.2024.

143. M. P. J. Lavery, S. M. Barnett, F. C. Speirits and M. J. Padgett, "Observation of the rotational Doppler shift of a white-light, orbital-angular-momentum-carrying beam backscattered from a rotating body", *Optica* **1** (2014) 1, 1–4, doi:10.1364/OPTICA.1.000001.

144. Y. Liu, C. Lao, M. Wang, Y. Cheng, Y. Wang, S. Fu, C. Gao, J. Wang, B.-B. Li, Q. Gong, Y.-F. Xiao, W. Liu and Q.-F. Yang, "Integrated vortex soliton microcombs", *Nat. Photonics* (2024), doi:10.1038/s41566-024-01418-x.

145. B. Chen, Y. Zhou, Y. Liu, C. Ye, Q. Cao, P. Huang, C. Kim, Y. Zheng, L. K. Oxenløwe, K. Yvind, J. Li, J. Li, Y. Zhang, C. Dong, S. Fu, Q. Zhan, X. Wang, M. Pu and J. Liu, "Integrated optical vortex microcomb", *Nat. Photonics* (2024), doi:10.1038/s41566-024-01415-0.

146. J. Li, S. Zeng, Y. Xie, Z. Wu, S. Lin, Y. Zhang and S. Yu, "Coherent Optical Comb Generation in the Joint Space of Frequency and Topological Charge", *Laser Photonics Rev.* **18** (2024) 4, 2300837, doi:10.1002/lpor.202300837.

147. Y. Li, E. Dieussaert and R. Baets, "Miniaturization of Laser Doppler Vibrometers–A Review", *Sensors* **22** (2022) 13, doi:10.3390/s22134735.

148. J. W. Czarske, "Laser Doppler velocimetry using powerful solid-state light sources", *Meas. Sci. Technol.* **17** (2006) 7, R71, doi:10.1088/0957-0233/17/7/R01.

149. D. Zhang, H. Zhao and J. Yang, "A high precision signal processing method for laser Doppler velocimeter", *Optik* **186** (2019), 155–164, doi:10.1016/j.ijleo.2019.04.066.

150. Z. Li, T. Liu, Y. Ren, S. Qiu, C. Wang and H. Wang, "Direction-sensitive detection of a spinning object using dual-frequency vortex light", *Opt. Express* **29** (2021) 5, 7453–7463, doi:10.1364/OE.418192.

151. A. Q. Anderson, E. F. Strong, B. M. Heffernan, M. E. Siemens, G. B. Rieker and J. T. Gopinath, "Detection technique effect on rotational Doppler measurements", *Opt. Lett.* **45** (2020) 9, 2636–2639, doi:10.1364/OL.390425.

152. H. Zhou, D. Fu, J. Dong, P. Zhang and X. Zhang, "Theoretical analysis and experimental verification on optical rotational Doppler effect", *Opt. Express* **24** (2016) 9, 10050–10056, doi:10.1364/OE.24.010050.

153. B. Liu, H. Chu, H. Giddens, R. Li and Y. Hao, "Experimental Observation of Linear and Rotational Doppler Shifts from Several Designer Surfaces", *Sci. Rep.* **9** (2019) 1, 8971, doi:10.1038/s41598-019-45516-1.

154. A. Q. Anderson, E. F. Strong, S. C. Coburn, G. B. Rieker and J. T. Gopinath, "Orbital angular momentum-based dual-comb interferometer for ranging and rotation sensing", *Opt. Express* **30** (2022) 12, 21195–21210, doi:10.1364/OE.457238.

155. R. Tang, X. Li, S. Qiu, X. Zhu, T. Liu, Z. Liu, X. Chen and Y. Ren, "Simultaneous measurement of spin and precession based on light's orbital angular momentum", *Opt. Express* **31** (2023) 24, 39995–40004, doi:10.1364/OE.503038.

156. W. Zhang, J. Gao, D. Zhang, Y. He, T. Xu, R. Fickler and L. Chen, "Free-Space Remote Sensing of Rotation at the Photon-Counting Level", *Phys. Rev. Appl.* **10** (2018), 044014, doi:10.1103/PhysRevApplied.10.044014.

157. D. B. Phillips, M. P. Lee, F. C. Speirits, S. M. Barnett, S. H. Simpson, M. P. J. Lavery, M. J. Padgett and G. M. Gibson, "Rotational Doppler velocimetry to probe the angular velocity of spinning microparticles", *Phys. Rev. A* **90** (2014), 011801, doi:10.1103/PhysRevA.90.011801.

158. R. Neo, S. Leon-Saval, J. Bland-Hawthorn and G. Molina-Terriza, "OAM interferometry: the detection of the rotational Doppler shift", *Opt. Express* **25** (2017) 18, 21159–21170, doi:10.1364/OE.25.021159.

159. O. Emile, J. Emile, C. Brousseau, T. l. Guennic, P. Jian and G. Labroille, "Rotational Doppler shift of the light transmitted behind a rotating object with rotational symmetries: rotational Doppler shift of the transmitted light", *Eur. Phys. J. D* **76** (2022) 1, 8, doi:10.1140/epjd/s10053-022-00338-1.

160. O. Emile, J. Emile, C. Brousseau, T. le Guennic, P. Jian and G. Labroille, "Rotational Doppler shift from a rotating rod", *Opt. Lett.* **46** (2021) 15, 3765–3768, doi:10.1364/OL.435058.

161. H.-L. Zhou, D.-Z. Fu, J.-J. Dong, P. Zhang, D.-X. Chen, X.-L. Cai, F.-L. Li and X.-L. Zhang, "Orbital angular momentum complex spectrum analyzer for vortex light based on the rotational Doppler effect", *Light: Sci. Appl.* **6** (2017) e16251, doi:10.1038/lsa.2016.251.

162. J. Courtial, K. Dholakia, D. A. Robertson, L. Allen and M. J. Padgett, "Measurement of the Rotational Frequency Shift Imparted to a Rotating Light Beam Possessing Orbital Angular Momentum", *Phys. Rev. Lett.* **80** (1998), 3217–3219, doi:10.1103/PhysRevLett.80.3217.

163. Modified from work by E-karimi (CC BY-SA 3.0), *Wikimedia Commons*, https://en.wikipedia.org/wiki/Optical_vortex#/media/File:Helix_oam.png, 10.1.2025.

164. Modified from work by E-karimi (CC BY-SA 3.0), *Wikimedia Commons*, https://en.m.wikipedia.org/wiki/Angular_momentum_of_light#/media/File%3ASpiral-phase-plate.png, 17.1.2025.

165. X. Wang, Z. Nie, Y. Liang, J. Wang, T. Li and B. Jia, "Recent advances on optical vortex generation", *Nanophotonics* **7** (2018) 9, 1533–1556, doi:10.1515/nanoph-2018-0072.

166. S. Li, W. Yu, L. Meriggi, Q. Xiao, Z. Nong, X. Cai, M. Sorel and S. Yu, "High-directional vortex beam emitter based on Archimedean spiral adiabatic waveguides", *Opt. Lett.* **42** (2017) 5, 975–978, doi:10.1364/OL.42.000975.

167. M. Beijersbergen, R. Coerwinkel, M. Kristensen and J. Woerdman, "Helical-wavefront laser beams produced with a spiral phaseplate", *Opt. Commun.* **112** (1994) 5, 321–327, doi:10.1016/0030-4018(94)90638-6.

168. M. P. J. Lavery, F. C. Speirits, S. M. Barnett and M. J. Padgett, "Detection of a Spinning Object Using Light's Orbital Angular Momentum", *Science* **341** (2013) 6145, 537–540, doi:10.1126/science.1239936.

169. L. Fang, M. J. Padgett and J. Wang, "Sharing a Common Origin Between the Rotational and Linear Doppler Effects", *Laser Photonics Rev.* **11** (2017) 6, 1700183, doi:10.1002/lpor.201700183.

170. J. Leach, S. Keen, M. J. Padgett, C. Saunter and G. D. Love, "Direct measurement of the skew angle of the Poynting vector in a helically phased beam", *Opt. Express* **14** (2006) 25, 11919–11924, doi:10.1364/OE.14.011919.

171. N. A. Chaitanya, A. Aadhi, M. V. Jabir and G. K. Samanta, "Frequency-doubling characteristics of high-power, ultrafast vortex beams", *Opt. Lett.* **40** (2015) 11, 2614–2617, doi:10.1364/OL.40.002614.

172. O. Emile, J. Emile and C. Brousseau, "Rotational Doppler shift upon reflection from a right angle prism", *Appl. Phys. Lett.* **116** (2020) 22, 221102, doi:10.1063/5.0009396.

173. J. Courtial, D. A. Robertson, K. Dholakia, L. Allen and M. J. Padgett, "Rotational Frequency Shift of a Light Beam", *Phys. Rev. Lett.* **81** (1998), 4828–4830, doi:10.1103/PhysRevLett.81.4828.

174. M. Hautakorpi, J. Lindberg, T. Setälä and M. Kaivola, "Rotational frequency shifts in partially coherent optical fields", *J. Opt. Soc. Am. A* **23** (2006) 5, 1159–1163, doi:10.1364/JOSAA.23.001159.

175. O. Emile and J. Emile, "Naked eye picometer resolution in a Michelson interferometer using conjugated twisted beams", *Opt. Lett.* **42** (2017) 2, 354–357, doi:10.1364/OL.42.000354.

176. "HITRANonline: The HITRAN Database", *HITRANonline*, https://hitran.org/, 4.10.2024.

177. "Laser Spectroscopy Group", https://www.helsinki.fi/en/researchgroups/laser-spectroscopy, 26.9.2024.

178. E. W. Weisstein, "Lorentzian Function", *Wolfram MathWorld*, https://mathworld.wolfram.com/LorentzianFunction.html, 20.9.2024.

179. E. W. Weisstein, "Gaussian Function", *Wolfram MathWorld*, https://mathworld.wolfram.com/GaussianFunction.html, 20.9.2024.

180. "Definitions and Units: Line-by-line Parameters", *HITRANonline*, https://hitran.org/docs/definitions-and-units/, 20.9.2024.

181. S. Abrarov, "The Voigt/complex error function", V.2.0.0.0, 2016, *MathWorks*, https://se.mathworks.com/matlabcentral/fileexchange/47801-the-voigt-complex-error-function-second-version, 20.9.2024.

182. R. Shankar, *Fundamentals of physics I: mechanics, relativity, and thermodynamics*, Yale University Press, New Haven CT, 2019, expanded edition.

183. N. R. Newbury, I. Coddington and W. Swann, "Sensitivity of coherent dual-comb spectroscopy", *Opt. Express* **18** (2010) 8, 7929–7945, doi:10.1364/OE.18.007929.

184. A. Sieghard, K. A. Keppler and M. Quack, "High-resolution Fourier Transform Infrared Spectroscopy", in *Handbook of High-resolution Spectroscopy*, eds. M. Quack and F. Merkt, John Wiley & Sons, 2011, vol. 2.

185. C. Palmer and E. Loewen, *Diffraction Grating Handbook*, Newport Corporation, 2005, 6th edn.

186. R. Kochanov, I. Gordon, L. Rothman, P. Wcisło, C. Hill and J. Wilzewski, "HITRAN Application Programming Interface (HAPI): A comprehensive approach to working with spectroscopic data", *J. Quant. Spectrosc. Radiat. Transf.* **177** (2016), 15–30, doi:10.1016/j.jqsrt.2016.03.005.

187. "HAPI: The HITRAN Application Programming Interface", V.1.2.2.0, 2021, *HITRANonline*, https://hitran.org/hapi/, 18.9.2024.

188. S. Dohe, V. Sherlock, F. Hase, M. Gisi, J. Robinson, E. Sepúlveda, M. Schneider and T. Blumenstock, "A method to correct sampling ghosts in historic near-infrared Fourier transform spectrometer (FTS) measurements", *Atmos. Meas. Tech.* **6** (2013) 8, 1981–1992, doi:10.5194/amt-6-1981-2013.

189. L. Shao and P. R. Griffiths, "Correcting Nonlinear Response of Mercury Cadmium Telluride Detectors in Open Path Fourier Transform Infrared Spectrometry", *Anal. Chem.* **80** (2008) 13, 5219–5224, doi:10.1021/ac800522w.

190. I. Sadiek, A. J. Fleisher, J. Hayden, X. Huang, A. Hugi, R. Engeln, N. Lang and J.-P. H. van Helden, "Dual-comb spectroscopy of ammonia formation in non-thermal plasmas", *Commun. Chem.* **7** (2024) 1, 110, doi:10.1038/s42004-024-01190-7.

191. L. A. Kranendonk, A. W. Caswell and S. T. Sanders, "Robust method for calculating temperature, pressure, and absorber mole fraction from broadband spectra", *Appl. Opt.* **46** (2007) 19, 4117–4124, doi:10.1364/AO.46.004117.

192. P. H. C. Eilers, "A Perfect Smoother", *Anal. Chem.* **75** (2003) 14, 3631–3636, doi:10.1021/ac034173t.

193. G. Vallone, "On the properties of circular beams: normalization, Laguerre–Gauss expansion, and free-space divergence", *Opt. Lett.* **40** (2015) 8, 1717–1720, doi:10.1364/OL.40.001717.

194. Y. Shen, X. Wang, Z. Xie, C. Min, X. Fu, Q. Liu, M. Gong and X. Yuan, "Optical vortices 30 years on: OAM manipulation from topological charge to multiple singularities", *Light: Sci. Appl.* **8** (2019) 90, doi:10.1038/s41377-019-0194-2.

195. M. A. Bandres and J. C. Gutiérrez-Vega, "Circular beams", *Opt. Lett.* **33** (2008) 2, 177–179, doi:10.1364/OL.33.000177.

196. M. Babiker, D. L. Andrews and V. E. Lembessis, "Atoms in complex twisted light", *J. Opt.* **21** (2018) 1, 013001, doi:10.1088/2040-8986/aaed14.

197. S. G. Reddy, C. Permangatt, S. Prabhakar, A. Anwar, J. Banerji and R. P. Singh, "Divergence of optical vortex beams", *Appl. Opt.* **54** (2015) 22, 6690–6693, doi:10.1364/AO.54.006690.

198. M. J. Padgett, F. M. Miatto, M. P. J. Lavery, A. Zeilinger and R. W. Boyd, "Divergence of an orbital-angular-momentum-carrying beam upon propagation", *New J. Phys.* **17** (2015) 2, 023011, doi:10.1088/1367-2630/17/2/023011.

199. S. Saghafi and C. Sheppard, "The beam propagation factor for higher order Gaussian beams", *Opt. Commun.* **153** (1998) 4, 207–210, doi:10.1016/S0030-4018(98)00256-9.

Appendices

A1 Absorption lineshapes

The area-normalized Lorentzian absorption lineshape function centered at ν_0 is given by[178]

$$L(\nu-\nu_0,\delta\nu_{\mathrm{L}})=\frac{1}{\pi}\frac{\delta\nu_{\mathrm{L}}}{(\nu-\nu_0)^2+\delta\nu_{\mathrm{L}}^2}\,, \tag{A1.1}$$

where $\delta\nu_{\mathrm{L}}$ is the half-width-at-half-maximum (HWHM) of the line.

The area-normalized Doppler (Gaussian) absorption lineshape function centered at ν_0 is given by[179]

$$G(\nu-\nu_0,\delta\nu_{\mathrm{G}})=\frac{1}{\sigma\sqrt{2\pi}}\exp\left(-\frac{1}{2}\frac{(\nu-\nu_0)^2}{\sigma^2}\right),\quad \sigma=\frac{\delta\nu_{\mathrm{G}}}{\sqrt{2\ln 2}}\,, \tag{A1.2}$$

where the HWHM is given by[180]

$$\delta\nu_{\mathrm{G}}=\frac{\nu_0}{c}\sqrt{\frac{2k_{\mathrm{B}}T\ln 2}{m}}\,, \tag{A1.3}$$

where k_{B} is the Boltzmann constant, T the temperature, c the speed of light and m the mass of a single molecule.

The Voigt profile is the convolution of the above two such that[34]

$$V(\nu-\nu_0)=\int_{-\infty}^{\infty}G\left(\nu',\delta\nu_{\mathrm{G}}\right)L\left(\nu-\nu_0-\nu',\delta\nu_{\mathrm{L}}\right)\mathrm{d}\nu'\,. \tag{A1.4}$$

Another way to define the Voigt profile is through[35]

$$V(\nu-\nu_0)=\frac{\mathrm{Real}[\mathrm{F}(z)]}{\sigma\sqrt{2\pi}},\quad z=\frac{\nu-\nu_0+\mathrm{i}\delta\nu_{\mathrm{L}}}{\sigma\sqrt{2}}\,, \tag{A1.5}$$

which definition I have used for implementing the Voigt profile in Matlab; the Faddeeva function F has been implemented by S. Abrarov.[181]

A2 Intensity modulation in FTIR and the linear Doppler effect

To show that the interference between the combined electric fields in an FTIR instrument indeed results in an intensity modulation signal, we start with an incident electric field $E_0\exp(\mathrm{i}2\pi\nu t)$ and define the corresponding incident intensity as $I_0\equiv|E_0\exp(\mathrm{i}2\pi\nu t)|^2=|E_0|^2$. In addition, let the beam splitter have a transmittance T and reflectivity R, with (intensity) efficiency in the delay and reference arm denoted by η_{del} and η_{ref}, respectively. As a reminder, in an FTIR instrument (Fig. 4), the incoming light beam is split into two arms, where, for example, the light beam entering the delay arm is first transmitted (or reflected) through the beam splitter, after which it accumulates a phase $\phi_\nu(t)=2\pi\times 2ut\nu/c$ due to the translating mirror, and finally it reflects from (or is transmitted through) the beam splitter, such that

the total (intensity) efficiency is given by η_{del}. The resulting intensity at the detector when the two beams are combined is

$$\begin{aligned} I(t) &= \left| E_0\sqrt{T}\sqrt{R}\sqrt{\eta_{\mathrm{del}}}\exp(\mathrm{i}[2\pi\nu t + \phi_\nu(t)]) + E_0\sqrt{R}\sqrt{T}\sqrt{\eta_{\mathrm{ref}}}\exp(\mathrm{i}2\pi\nu t)\right|^2 \\ &= |E_0|^2 RT\eta_{\mathrm{del}} + |E_0|^2 RT\eta_{\mathrm{ref}} \\ &+ |E_0|^2 RT\sqrt{\eta_{\mathrm{del}}}\sqrt{\eta_{\mathrm{ref}}}\exp(\mathrm{i}[2\pi\nu t + \phi_\nu(t)])\exp(-\mathrm{i}2\pi\nu t) + c.c. \\ &= I_0 RT\left[\eta_{\mathrm{del}} + \eta_{\mathrm{ref}} + 2\sqrt{\eta_{\mathrm{del}}}\sqrt{\eta_{\mathrm{ref}}}\cos(\phi_\nu(t))\right] , \end{aligned} \tag{A2.1}$$

which is the result given in Supplement 1 of Article II, and which result was used to analyse the interferogram quality in the PC-FTS work. We see that the interferogram consists of a DC component (which can be filtered out), and of the AC component of interest (the intensity modulation). With the ideal case $R = T = 0.5$ and $\eta_{\mathrm{ref}} = \eta_{\mathrm{del}} = 1$,

$$I(t) = \frac{I_0}{2}\left[1 + \cos(\phi_\nu(t))\right] , \tag{A2.2}$$

so we get the expected result that at perfect constructive interference $I = I_0$ and at perfect destructive interference $I = 0$.

The above derivation also reveals another way to explain FTS. Basically, the linear time-dependent phase accumulation in the delay arm means that the translational motion of the moving mirror changes the optical frequency by the amount $\Delta f = \mathrm{d}\phi_\nu(t)/\mathrm{d}t/(2\pi) = 2u\nu/c$, which is exactly the amount expected based on the linear Doppler effect.[182] This equivalent explanation of FTS through the Doppler effect is important for explaining the rotational-Doppler spectroscopy technique proposed in Article V and discussed in Section 5. The above derivation also illustrates the basic result that when combining electric fields with slightly different optical frequencies, beating (meaning intensity modulation) emerges at their difference frequency.

A3 Signal-to-noise ratio in FTS

Noise in FTIR and in dual-comb spectroscopy has been discussed in many pieces of literature.[66,76,183] Combining the conclusions from those and from numerical simulations I have performed to verify the results, the spectral signal-to-noise ratio in FTS is proportional to:

$$\mathrm{SNR_s} \propto \frac{\frac{P}{\Delta\nu}\delta\nu\sqrt{t}\sqrt{F_\mathrm{s}}}{\sigma_{\mathrm{noise}}} , \tag{A3.1}$$

where P is the total optical power at the detector, $\Delta\nu$ the optical bandwidth, $P/\Delta\nu$ then the power spectral density, $\delta\nu$ the resolution, t the measurement time, F_s the sampling rate and σ_{noise} some general source of white noise such as the noise equivalent power of the detector – I only consider here the simple case of only white noise without considering its specific source; a more rigorous analysis with distinctions between different noise types has been considered, in the context of dual-comb spectroscopy, in [183].

When reading noise literature one needs to be careful with the assumptions and meanings behind the different parameters. For example, does increasing the optical bandwidth assume constant total optical power, or will the total optical power

simultaneously increase to keep the power spectral density constant. The following list is an attempt to intuitively explain the result (A3.1). Hereafter, it is assumed that the noise standard deviation σ_{noise} is kept constant.

- Increasing the total optical power while keeping the optical bandwidth constant leads to a linearly increasing SNR because the height of each frequency component in the spectrum increases compared to the noise that is assumed here to stay unchanged. Note, however, that increasing the optical power usually does also increase the noise due to laser intensity noise.
- Increasing the optical bandwidth while keeping the total optical power constant leads to a linearly decreasing SNR because the optical power per frequency component decreases.
- Improving the resolution (smaller $\delta\nu$ value) leads to a linearly decreasing SNR because the "power per resolution element" is decreased; the "number of resolution elements" is defined in FTIR literature by $M = \Delta\nu/\delta\nu$. **However**, in FTIR, increasing resolution usually also means measuring a longer interferogram (assuming the mirror scan velocity is kept constant). Then, while the resolution improves, the measurement time simultaneously increases. In this case, the overall effect is to **decrease** the SNR to the **square root** of the resolution.
  - Interestingly, the SNR worsens in DCS to the square root of the resolution *until* the comb teeth are resolved. After this, the SNR again *increases* to the square root of the resolution (measurement time, *i.e.*, the length of the measured time window). This may be explained by noting that after a mode resolved measurement is achieved, the number of spectral elements per resolution element no longer decreases but is capped to one.
- Increasing the measurement time always increases the SNR to the square root (assuming white noise). This is because the more one samples the noise, the more it is effectively averaged. Interestingly, keeping all other parameters constant but increasing, say, the scan velocity, the SNR *decreases* to the square root.[76] The same goes for changing the FTS modality from traditional FTIR to a PC-FTS-type measurement: only the measurement time (assuming fixed resolution) is decreased, which is seen as worsened SNR.
- In a similar way, increasing the sampling frequency also increases the SNR to the square root because the noise is then sampled more.

The conclusions here were all verified by numerical simulations that I performed, but I omit their illustration. Note, however, that in reality the behaviour of noise can be more complex. The most obvious example is the 1/f noise, the mitigation of which usually requires one to prefer high down-converted frequencies (*e.g.*, to increase the scan velocities, contradictory to the above case of only white noise). In addition, the response of different detectors can vary as a function of the down-converted frequency.[76]

A4 Appendices to the HCl work

A4.1 Lorentzian fit model assumption

As summarized in Supplementary information of Article II, the pressure broadened half-widths of the HCl absorption lines are, on average, 1.4 GHz in the experimental conditions of the measurements. The Doppler half-widths are less than 0.1 GHz, whereas the half-width-at-half-maximum (HWHM) of the expected instrument lineshape function (ILS) from the Norton–Beer medium apodization function is 0.3 GHz (the corresponding nominal resolution according to the full sinc base width definition 2.3 is 0.7 GHz). The absorption features were fitted assuming a Lorentzian lineshape, and the measured pressure broadenings were reported as the HWHMs of the fitted Lorentzians; the inaccuracy from assuming negligible Doppler and instrument broadening was considered by estimating the corresponding uncertainty based on an assumption that the total observed absorption linewidth is given by the square root of the sum of squares of these three broadening types, a result exactly valid only for the convolution of Gaussian functions.[184] In Article II, it was said that if the instrumental broadening (HWHM of the ILS) is less than a third of the HWHM of the absorption line, it can be deemed negligible. However, I did not define what "negligible" means in the quantitative sense. Here, I consider the effect of trying to fit a Lorentzian function to a partly Doppler and Norton–Beer medium ILS broadened absorption line to arrive at a rule-of-thumb to estimate the required resolution for a desired linewidth accuracy level.

Figure 28 shows a simulated Voigtian HCl absorption spectrum in the experimental conditions of Article II. It also shows a simulated spectrum that additionally has instrumental broadening. The lower panel shows the difference of these, but also the fit residuals from fitting pure Lorentzians to the simulated spectra. We can see that the Lorentzian functions can represent both simulated spectra with reasonable accuracy, while the difference between the two simulated spectra themselves is much larger than the fit residuals in either case.

As seen in Supplementary information of Article II, the pressure broadened linewidths of the HCl transitions depend on the specific line in question. This means that there are lines with varying degrees of Gaussianity but also with varying HWHM-to-ILS width ratios. Gathering the data from the above fits, Figure 29a plots the difference of the fitted Lorentzian HWHM to the true underlying Lorentzian HWHM in the case without intrumental broadening, as a function of the Gaussianity. Similarly, Figure 29b plots it in the case with instrumental broadening but as a function of the HWHM of the fitted line to the HWHM of the ILS function. In the latter case, we see that if the HWHM of the ILS is limited to less than 30 % of the HWHM of the fitted line, the deviation of the fitted HWHM is less than 5 % of the true pressure broadening. Interestingly, in the case without instrumental broadening, the 5 % inaccuracy level requires less than 25 % Gaussianity, in other words, the requirement is even stricter, even though there are fewer broadening effects in this case. This result is probably explained by the fact that whether the HWHM of the fitted Lorentzian represents well the actual HWHM of the broadenend line, let alone the true underlying pressure broadening, depends in a complex way on the different convoluting functions.

Of course, these simulations here are specific to the environmental conditions of the measurements in Article II. For example, the results surely change if one were to use

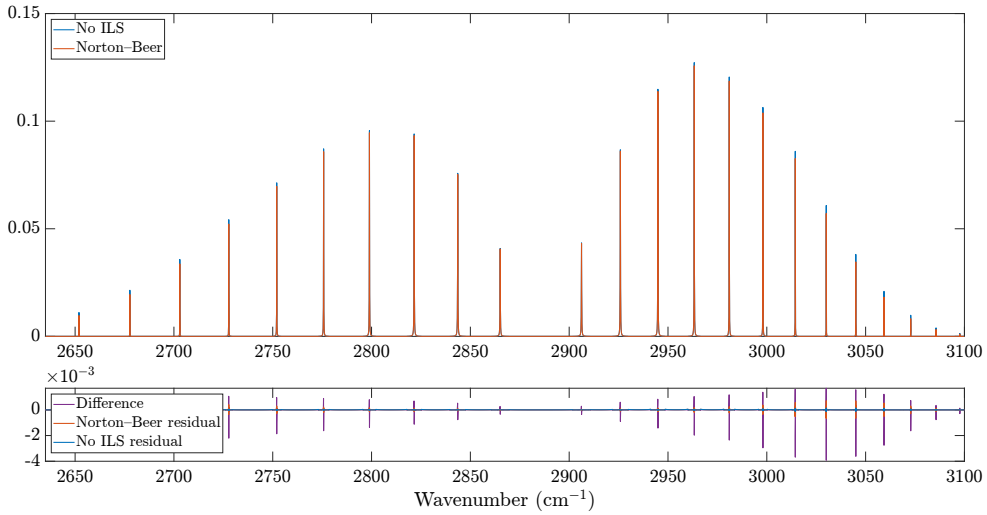

Figure 28: Simulated $H^{35}Cl$ absorption spectrum without and with instrumental broadening. The lower panel shows the difference of these, but also the fit residuals for both when using a Lorentzian fit model.

different apodization functions but also if one changed, say, the concentration. This is because the ILS function convolutes the transmission spectrum, which means that the lineshapes change as a function of the concentration because the absorption and transmission spectra are separated by the exponent/logarithm function of the Beer–Lambert law. Still, these simulations should provide a nice rule of thumb for the required instrumental resolution versus the true absorption linewidth. In addition, similar simulations can be easily set up to study some other conditions.

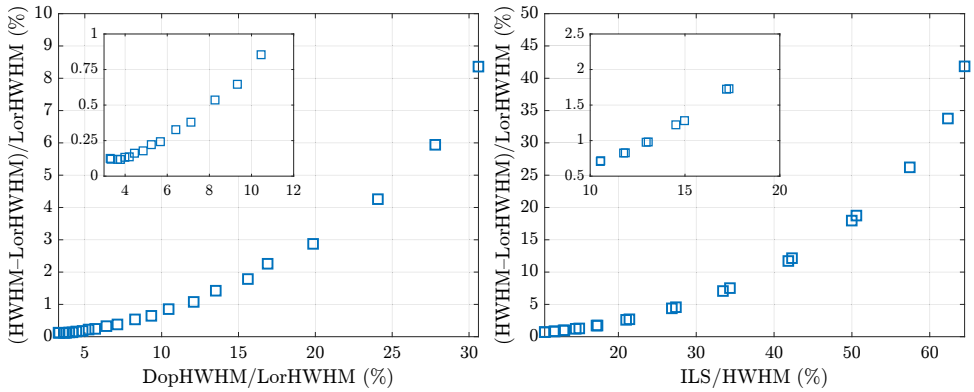

(a) Voigt lineshapes without instrumental broadening.

(b) With instrumental broadening.

Figure 29: Deviations of the fitted Lorentzian HWHMs ("HWHM") from the true underlying Lorentzian pressure broadenings ("LorHWHM") in two cases: without and with instrumental broadening. The horizontal axis in (a) describes the Gaussianity of the absorption line (the Doppler broadening relative to the Lorentzian pressure broadening). The "ILS" in the horizontal axis definition of (b) refers to the HWHM of the Norton–Beer medium instrument lineshape function. That value is 285 MHz, which is 1.4 times greater than the HWHM of a corresponding sinc ILS (whereas the corresponding half-width sinc base is obtained from the sinc HWHM by dividing by 0.603).

A5 Appendices to PC-FTS

A5.1 Derivation of the down-conversion relation

The down-conversion relation in PC-FTS has been derived in Supplementary Information of [21]. For completeness, I have included a similar derivation here. To start, we determine the increased distance L that a given optical frequency (dispersed by the grating onto the scanning mirror surface) experiences in the delay arm when the scanning mirror angle is opened by an angle $\theta = \omega_{\mathrm{rot}} t$, where ω_{rot} is the angular velocity of the mirror. All the necessary geometry arguments are presented in Figure 30, which lead to the result

$$L(t) \approx l_{\mathrm{f}} N (\lambda - \lambda_0) \omega_{\mathrm{rot}} t \,. \tag{A5.1}$$

The corresponding phase delay is obtained from this result by noting that due to the 4f-geometry, the optical frequency travels four times this distance L in the delay arm and that the corresponding phase is obtained by dividing the result by the wavelength (to obtain the number of optical cycles that the optical frequency is delayed by) and by multiplying by 2π. Finally, the corresponding down-converted frequency is given by the derivative

$$\begin{aligned} f &= -\frac{1}{2\pi}\frac{\mathrm{d}\phi_\lambda(t)}{\mathrm{d}t} = -\frac{4L(t)}{\lambda t} \approx -\frac{4 l_{\mathrm{f}} N}{\lambda}(\lambda - \lambda_0)\omega_{\mathrm{rot}} = -4 l_{\mathrm{f}} N \nu \left(\frac{1}{\nu} - \frac{1}{\nu_0}\right) \omega_{\mathrm{rot}} \\ &= \frac{4 l_{\mathrm{f}} N \omega_{\mathrm{rot}}}{\nu_0}(\nu - \nu_0) = \frac{8 l_{\mathrm{f}} N \Delta\theta f_{\mathrm{scan}}}{\nu_0}(\nu - \nu_0) \,, \end{aligned} \tag{A5.2}$$

where, like in Article III, I have defined $\omega_{\mathrm{rot}} = \Delta\theta / \Delta T = 2\Delta\theta f_{\mathrm{scan}}$, where f_{scan} is the scan frequency of the rotating mirror, $\Delta\theta$ the maximum mechanical scan angle of the mirror and ΔT the length of the time window. The factor of two considers the fact that two interferograms are obtained in a time $1/f_{\mathrm{scan}}$ (there are two scan directions during one full scan cycle). Note that the derivation relies heavily on approximations of small angles. However, as illustrated by the many numerical values calculated in Article III and its Supplement, the experimental results match nicely the calculated ones. In any case, one performs the phase- and group delay corrections to determine the true down-conversion factor and the frequency ν_0.

Let's also estimate the down-conversion relation in the case where the grating would be replaced with a planar mirror (normal FTIR mode) and where all the optical frequencies would strike the edge of the mirror of width W. Then, the down-converted frequency would be

$$f = \frac{4L(t)}{\lambda t} \approx \frac{4 W \omega_{\mathrm{rot}}}{\lambda} = \frac{8 W \Delta\theta f_{\mathrm{scan}}}{c} \nu \,, \tag{A5.3}$$

which comes from $L(t) \approx W \omega_{\mathrm{rot}} t$, as seen in Figure 30. Assuming the largest optical frequency of 90.7 THz used in Article III, the fact that it was down-converted to 630 Hz and that the interferogram lengths were about 1.82 s, the resulting optical resolution (Eq. 2.3) would be 158 GHz, a value that is a factor of 13 poorer than in the PC-FTS measurement mode (12 GHz). Note that this corresponds to a maximum mechanical scan length of $W\Delta\theta = 1$ mm (assuming $f_{\mathrm{scan}} = 0.25$ Hz).

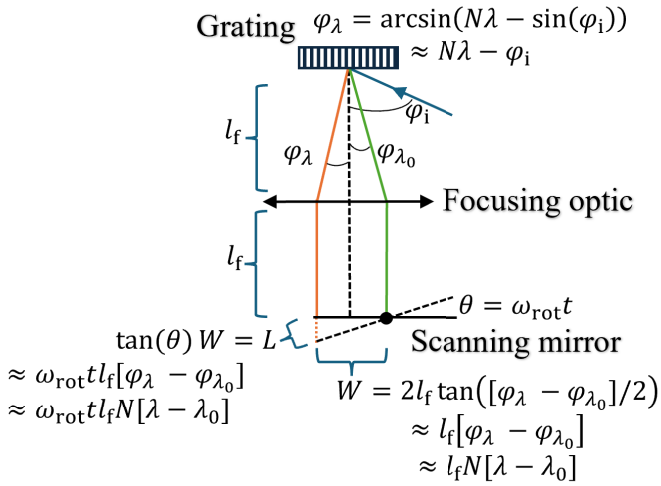

Figure 30: Geometry arguments to derive the down-conversion relation in PC-FTS. When a light beam with wavelength λ strikes the grating with a grating groove density N, it is dispersed to an angle φ_λ given by the grating equation.[185] θ is the mechanical scan angle swept in time t when the mirror is tilted with an angular frequency ω_{rot}. l_f is the focal length of the focusing optic. The goal is to solve for the mechanical path difference L, which is found by using the distance W that the dispersed wavelength experiences compared to the one that hits the pivot point of the mirror. Note that the derivations make use of the small angle approximation.

A5.2 Numerical simulations

To show that the poor matching between the measured methane absorption spectrum and the HITRAN reference spectrum in Article III is most likely due to the irreproducibility of the rotating mirror scans that lead to imperfect interferogram corrections, I simulated synthetic interferograms by summing up cosines, as given by Equation (A5.4).

$$I(t) = \sum_i^N \mathrm{T}(f_i)\mathrm{E}(f_i)\cos\left(2\pi f_i[t + \delta t(t)] + \phi_i\right) , \tag{A5.4}$$

where $\mathrm{T}(f)$ is a methane transmission spectrum simulated using the HITRAN API,[186,187] down-converted using Equation (3.1) and evaluated at a down-converted frequency f. $\mathrm{E}(f)$ is a function used to shape the envelope of the spectrum (it is basically a rectangle with height 1, but with the corners at the start and end of the down-converted frequency bandwidth smoothed with a sine ramp). ϕ_i is a frequency dependent phase chosen as shape resembling a distorted parabola: I wanted to make the simulations more interesting by making the interferograms asymmetrical. Other values used in the simulation are listed in Table 6.

The $\delta t(t)$ in Equation (A5.4) is timing jitter added to the interferogram. Basically, I analysed a few subsequent experimental single-frequency interferograms and determined that on average when the interferograms cross zero, the exact zero-crossing locations can vary with a standard deviation of about 0.2 ms. I chose one such experimental interferogram and stored the deviations of the zero-crossing locations from the average zero-crossing locations (see Fig. 31). Finally, I interpolated the

jitter versus average zero-crossing location vector to the full sampling density of the time axis used in the simulation. The result is basically the function $\delta t(t)$.

Table 6: Settings used in the numerical simulations. These mimic the experimental settings used in Article III.

Number of cosines	10000
Pivot point frequency	83.8 THz
Optical bandwidth of interest	84.9–90.7 THz (5.8 THz)
Down-converted bandwidth	100–631.6 Hz (531.6 Hz)
Down-conversion factor	9.1505×10^{-11}
Optical resolution	13.2 GHz
Length of interferogram	1.65 s
Sampling frequency	50 kHz
Pressure	1000 mbar
Concentration	1 %
Absorption path length	10 cm
Temperature	296 K

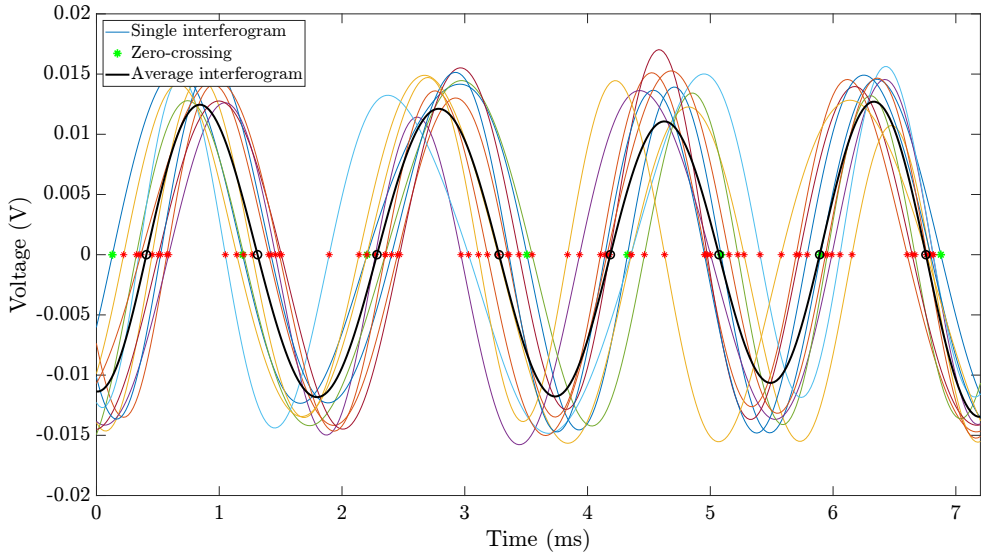

Figure 31: Example of ten successive experimental single-frequency interferograms and their average with their zero-crossings marked. The function $\delta t(t)$ discussed in the text is obtained by calculating the deviations of the green asterisks' time locations from the corresponding time locations of the circles, which gives the deviation (jitter) as a function of the time locations of the circles.

I then simulated both an interferogram with and without the timing jitter, and for both, I simulated a corresponding background interferogram (an interferogram without the multiplicative factor $\mathrm{T}(f)$). I Fourier-transformed the interferograms, which yielded the spectra shown in Figure 32. We can see that the spectrum with timing jitter is majorly distorted, noisy, and shows nonzero intensity at optical frequencies where there shouldn't be any light emission. In particular, note how the emerged "noise pedestal" at the start of the optical bandwidth resembles that of the experimental spectrum shown Fig. 5 of Article III. It is noteworthy that the fact that different sampling errors or other distortions of the interferogram can result in erroneous spectra is well known in FTIR literature.[79, 188, 189]

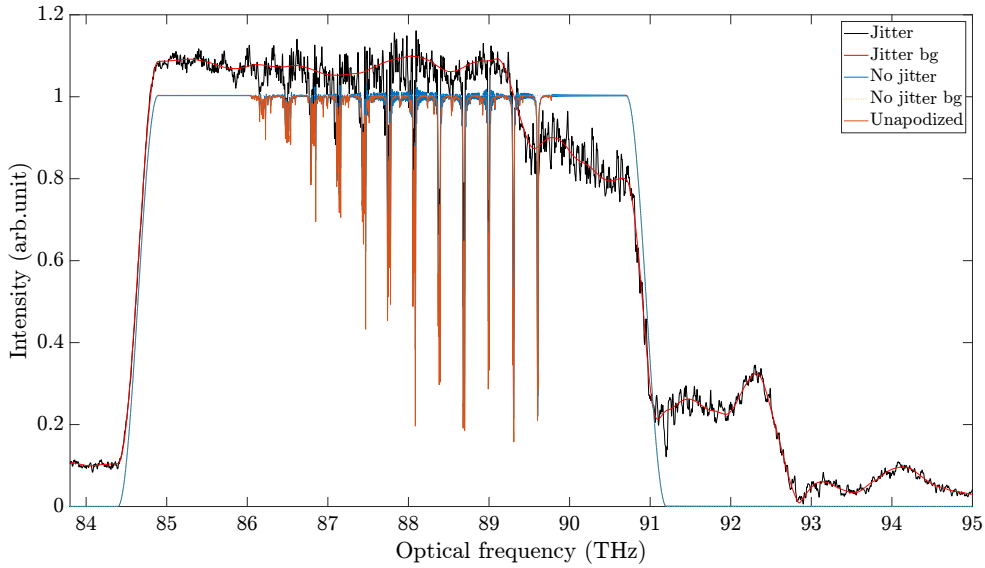

Figure 32: The simulated methane and background spectra with and without timing jitter, together with a full resolution HITRAN reference spectrum.

The resemblance between the simulated spectrum with jitter and the experimental spectra shown in Article III is even more evident when I process the simulated spectra into the corresponding absorption spectra, shown in Figure 33. Indeed, we can see that the effective resolution of the jittery spectrum is degraded such that, just like in Fig. 6 of Article III, it matches reasonably well with a simulated spectrum that assumes a Lorentzian instrument lineshape function. These results prove that the "residual phase noise" from the imperfect interferogram corrections is most likely the reason for the degraded quality of the experimental spectra, as was claimed in Article III.

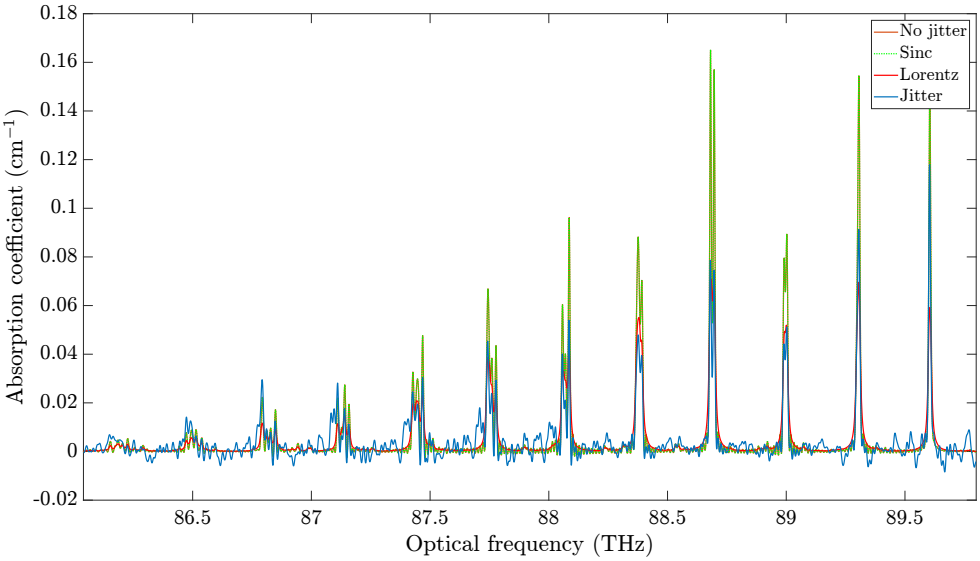

Figure 33: The corresponding absorption spectra derived from the simulated spectra shown in Fig. 32. "Sinc" is a reference spectrum simulated via the inverse Fourier transform of a HITRAN transmission spectrum, apodized with a boxcar function, and Fourier-transformed back to the absorption spectrum. This spectrum serves as a sanity check against the simulated spectra obtained as the FT of the summed-up cosine functions. "Lorentz" is the reference spectrum that provided the best match with the experimental spectrum in Article III.

A6 Appendices to DCS

A6.1 Numerical algorithm on synthetic interferograms

Here, I want to illustrate further the correction algorithm used in Article IV and show that it works. To that end, I generated synthetic interferograms with carrier envelope phase and repetition rate fluctuations and with absorption information encoded into them. The interferograms are generated according to Equation (A6.1).

$$I(t) = \sum_{i}^{N} \mathrm{T}(\Delta f_\mathrm{r} \times i)\mathrm{E}(\Delta f_\mathrm{r} \times i) \cos\left(2\pi \left[\Delta f_\mathrm{r} + \delta f_\mathrm{r}(t)\right] \times i \times t + \phi_i + \phi(t)\right) . \quad \text{(A6.1)}$$

So basically I summed up cosines, each with a distinct radiofrequency and with an amplitude modified by absorption: $\mathrm{T}(f)$ is an acetylene transmission spectrum simulated using the HITRAN API,[186,187] down-converted using Equation (4.1) and evaluated at a radiofrequency f. $\mathrm{E}(f)$ is a function used to shape the envelope of the radiofrequency spectrum. This envelope function is basically a rectangle (with height 1), but with the corners at the start and end of the radiofrequency bandwidth smoothed with a sine ramp (see, *e.g.*, Fig. 37). ϕ_i is frequency (not time) dependent phase. This function was chosen as shape resembling a distorted parabola to make the simulations more interesting (the resulting interferograms will be asymmetrical). The values for the repetition rate, the repetition rate difference, the optical and radiofrequency bandwidths, and so on, were chosen to resemble the experiment. The values are listed in Table 7.

Table 7: Settings used in the numerical simulations.

Number of cosines	6631
Repetition rate	250 MHz
Repetition rate difference	11.734 kHz
Optical bandwidth of interest	194–195.66 THz (1.66 THz)
Radiofrequency bandwidth	0–77.8 MHz
Sampling rate	200 MHz
Time window length	40 ms
Number of bursts in a segment	469
Pressure	301.4 mbar
Concentration	6.2 %
Absorption path length	10 cm
Temperature	295.5 K

The $\delta f_r(t)$ in Equation (A6.1) is the drift induced for the repetition rate difference.* Two examples of repetition rates with such drifts induced are shown in Figure 34; the right axis of said figure describes the corresponding "time of arrival" drift of the interferogram bursts in the resulting time windows (segments), as retrieved by the numerical algorithm by analysing the burst locations in the segments and calculating their difference from the case where they would appear equidistant in the segments. Note that these time of arrival curves are similar to the ones in Fig. 3 c of Article IV but that the overall drift here is more than an order of magnitude larger. The retrieved repetition rate difference is obtained by calculating the inverse of the time location difference between adjacent bursts in the segment as a function of time.

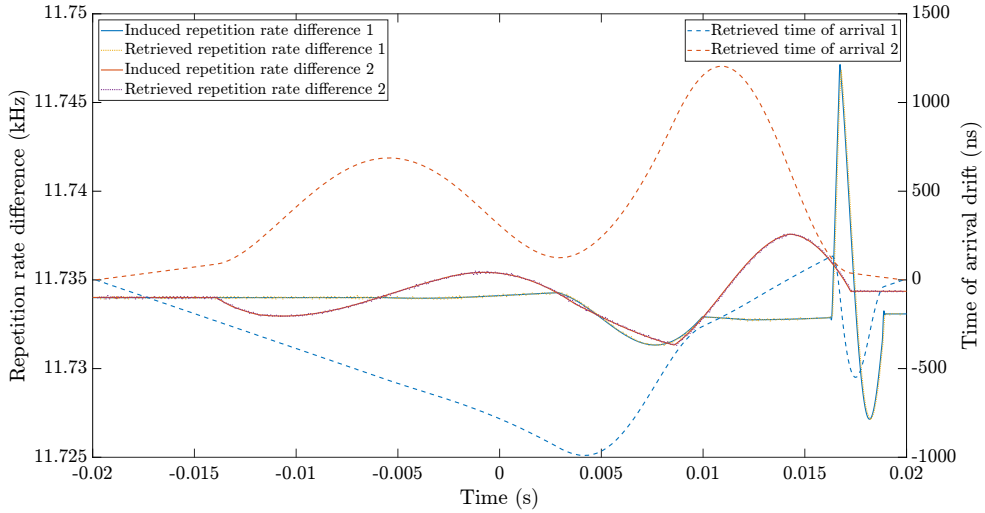

Figure 34: Two examples of induced repetition rate difference drifts and the corresponding interferogram time of arrival curves, as obtained by the numerical algorithm.

Similarly, $\phi(t)$ in Equation (A6.1) is the drift induced for the interferogram phase. Figure 35 shows two examples of such drifts, including the corresponding curves as extracted using the numerical algorithm. We can see that the extracted curves nicely follow the induced ones but that the extracted curves are noisy. This implies that

*Note that the resulting repetition rate difference is obtained by calculating the derivative $\frac{\mathrm{d}}{\mathrm{d}t}\left[(\Delta f_r + \delta f_r(t)) \times t\right]$, *i.e.*, it is not simply $\Delta f_r + \delta f_r(t)$.

the precision of the current correction implementation is limited, which should be addressed in the future.

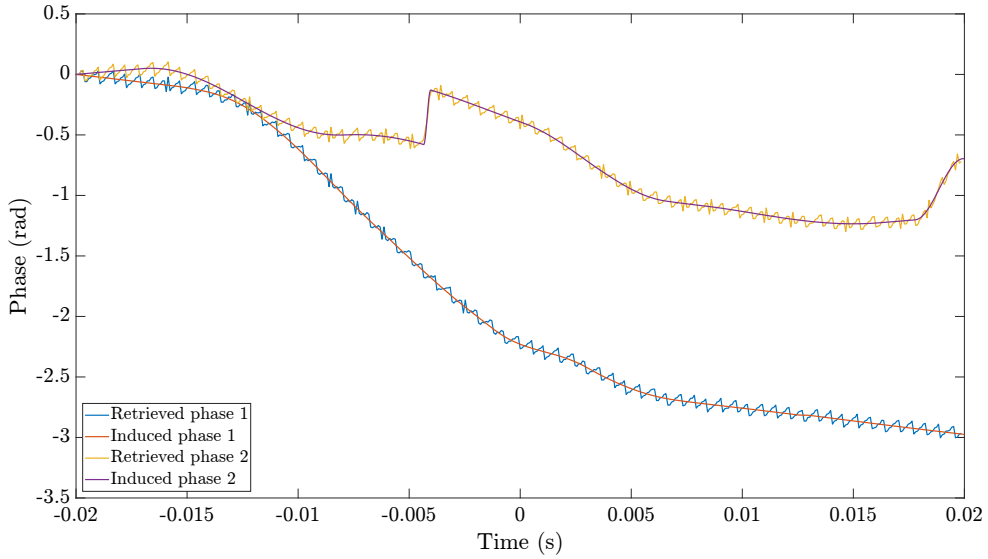

Figure 35: Two examples of induced interferogram phase drifts and the corresponding phase curves retrieved by the numerical algorithm.

Animation 2 illustrates how the corrections try to match the burst shapes in a segment to the shape of the very first burst in that segment. I wanted to include this animation to append Figure S5 in Supplement 1 of Article IV that illustrates the corrections. On the other hand, Figure 36 shows 5 uncorrected segments, and the 5 corrected segments and their average, as simulated here. Each of these segments have different repetition rate difference and interferogram phase drifts. We can see that, at least qualitatively, the corrections seem to work. Of course, the Fourier transforms of such segments should reveal more quantitatively if this is truly the case.

Figure 37 shows the FT of the five corrected and averaged segments with and without acetylene absorption. Note that without the corrections, the resulting spectra would have been completely degraded, for which reason they are not shown. We can see that the corrected spectra match each other nicely but that they also match reasonably well with an ideal case where no repetition rate difference or interferogram phase drifts were induced. However, at higher frequencies, the envelopes of the corrected spectra start to decline compared to the ideal case, which would decrease the SNR in actual measurements for those dual comb peaks. This implies that the repetition rate difference correction is not perfectly accurate,* the study and possible improvement of which are not included in this thesis. Fortunately, this decline in the spectral envelope behaves in a similar way for both the acetylene and the background spectrum, which then still results in accurate transmission spectra, as shown in Figure 38. There is only slight drift in the residual background and some noise, but, overall, the residuals are orders of magnitude smaller than in the experiments.

*Any inaccuracy in the repetition rate difference correction will be seen more drastically with higher frequency dual-comb peaks, as the frequency of a dual-comb peak is defined as the repetition rate difference multiplied by the corresponding mode number.

Animation 2: Illustration of the correction procedure. Each burst in a segment is compared against the very first burst in that segment. The left panel shows the current burst against the very first burst before any corrections, and the right panel the current burst after phase shifting it such that its shape matches the shape of the very first burst as precisely as possible.

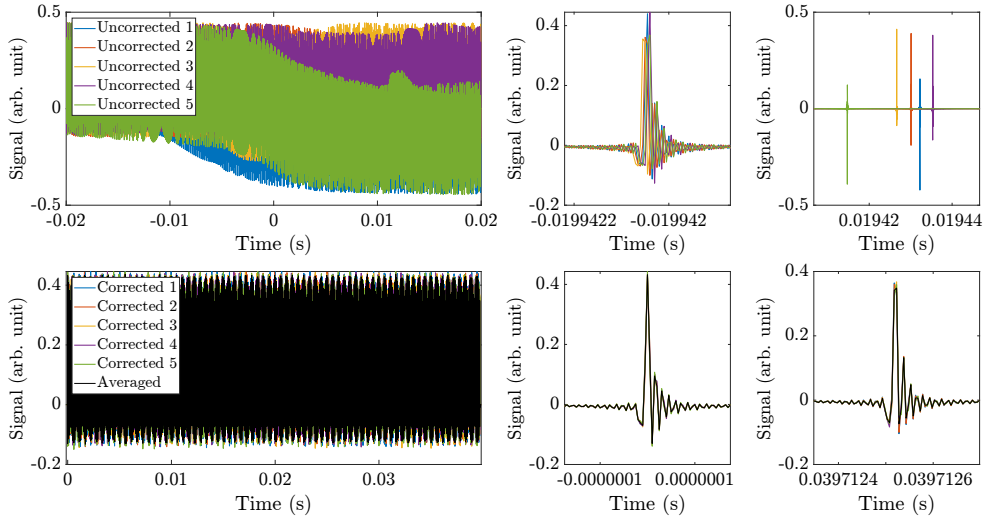

Figure 36: Examples of five segments with both repetition rate difference and interferogram phase drifts induced. The upper left panel shows the segments before corrections, and the bottom left panel shows them after corrections together with their average (the black trace). The four panels on the right show zoomed in views to the first and to the last bursts in the segments before corrections (top row) and after corrections (bottom row).

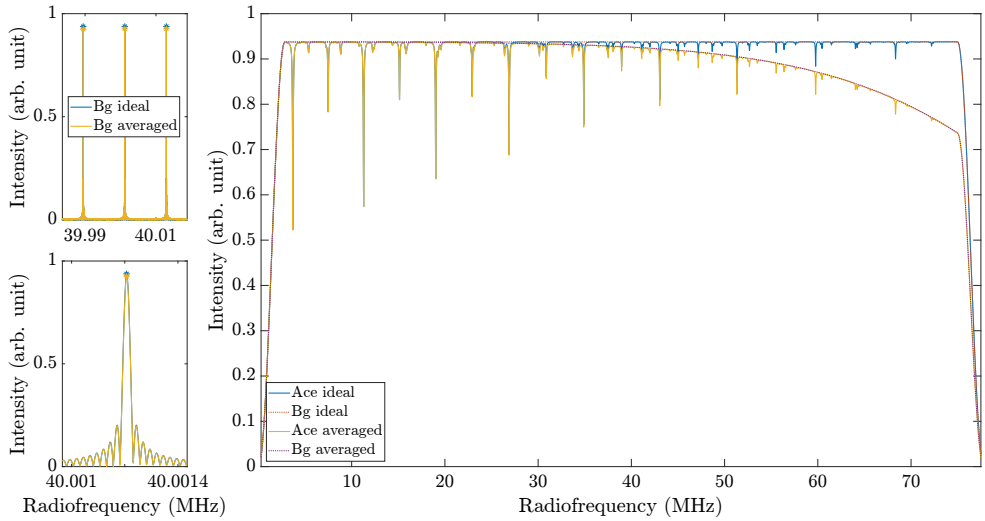

Figure 37: Emission spectra corresponding to the five corrected and averaged segments in Fig. 36. "Ace" refers to a spectrum with acetylene absorption and "Bg" to the corresponding background spectrum. "Ideal" refers to a case where no repetition rate difference or phase drifts were induced. The left panels show zoomed-in views to the dual-comb peaks prior to picking the peaks (the right panel is after peak picking).

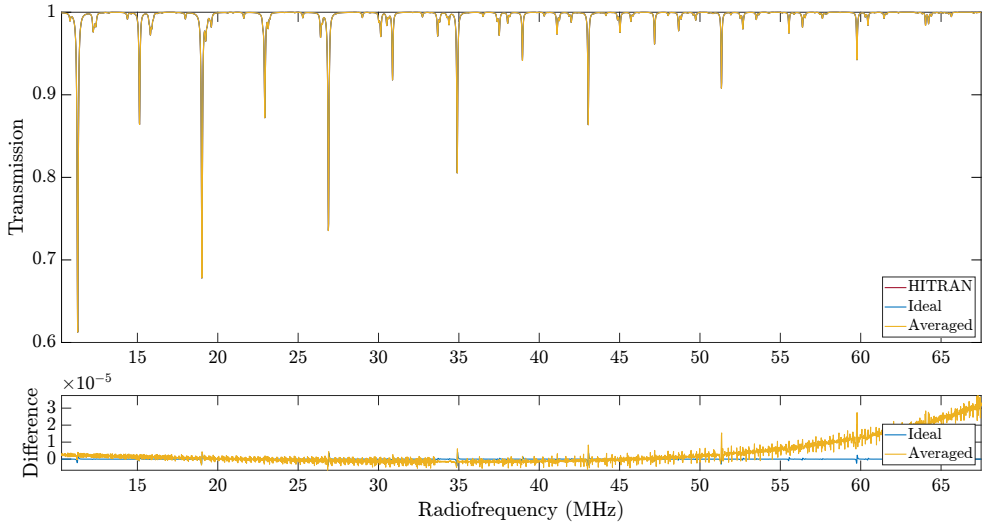

Figure 38: Transmission spectra calculated from the emission spectra in Fig. 37. "HITRAN" is the true HITRAN transmission spectrum I started with to produce the simulated interferograms: if the interferogram generation, Fourier-transformation and dual-comb peak picking were successful, this spectrum and the "Ideal" one (obtained from an interferogram simulation without any repetition rate difference or phase drifts induced) should match perfectly. The lower panel shows differences of the spectra obtained from the interferogram simulations against the true HITRAN spectrum.

Note, however, that the simulations above have ignored the fact that if the frequencies of the two combs have drifted in the absolute sense during measurements, they have sampled the absorption in a time dependent manner, even if the mutual coherence is restored by the corrections. Furthermore, even if the mutual coherence was perfect by chance during the measurements or without any corrections, the optical frequencies may still have drifted in concert during the measurements, possibly leading to distortion of the retrieved absorption lineshapes. Ignoring this latter, more

drastic case, but considering the case where one of the combs would be stabilized in the absolute manner but where the second comb would drift similarly to Figures 34 and 35, we can estimate the resulting optical frequency drift, which is done below.

As seen in Figure 34, the repetition rate difference drift is in the order of 10 Hz for the less drastic example in the figure. We can estimate what such drift would correspond to in the optical domain by solving ν from Equation (4.1) and by differentiating with respect to Δf_r:

$$\delta\nu = \left| \frac{\partial \nu}{\partial \Delta f_\mathrm{r}} \delta(\Delta f_\mathrm{r}) \right| = f \frac{f_\mathrm{r}}{(\Delta f_\mathrm{r})^2} \delta(\Delta f_\mathrm{r}) \,. \tag{A6.2}$$

For a radiofrequency at 40 MHz, which is approximately in the middle of the radiofrequency bandwidth used, the change of 10 Hz in the repetition rate frequency difference would result in an optical frequency change of as much as 730 MHz! On the other hand, the drift in the interferogram phase has a much lesser effect: the drift during the 40 ms long segment is in the order of a few radians, corresponding to a radiofrequency shift of a few tens of hertz, which in turn corresponds to an optical frequency shift in the order of 1 MHz (obtained by dividing the radiofrequency drift by the down-conversion factor $\Delta f_\mathrm{r}/f_\mathrm{r}$). However, keep in mind that the drifts induced in the simulations here are much more drastic than the drifts in the mutual coherence found in the experiments. Furthermore, recall Section 4 where I estimated the absolute optical frequency drift of a single optical frequency comb to be a few tens of MHz. Still, these types of drifts could already result in the distortion of the retrieved absorption spectra. Indeed, perhaps the residual structure seen in the experimental spectra presented in Article IV could partly be explained by these types drifts during measurements. On the other hand, the residuals in the article are still excellent and for sure sufficient for the proof-of-concept demonstration that the article is. However, the observations here, namely, that the precision of the numerical corrections could potentially be improved and that the drift of the optical frequencies in the absolute sense could distort absorption lines, should be addressed in the future if our approach were to be used, say, for trace gas analysis that targets to detect extremely weak absorption, or for linelist measurements that targets to determine accurate absorption lineshapes.

A6.2 Absorption in asymmetric DCS

Unfortunately, there is a mistake in Article V where we stated that the acetylene concentration is 6 % instead of 12 %. The experimental setup is currently constructed in the asymmetric configuration[25] where only one of the frequency combs propagates through the gas sample. Due to absorption, the electric field $E_1(\nu)$ of this comb is attenuated to $E_1(\nu) \times \exp(-\alpha(\nu)L/2)$, where $\alpha(\nu)$ is the absorption coefficient for the optical frequency ν and L is the length of the sample cell. When this electric field is combined with the electric field E_2 of the other comb, the observed intensity

$$I = E_1 \exp(-\alpha L/2) \times E_2^* \equiv I_0 \times \exp(-\alpha L/2) \,, \tag{A6.3}$$

whereas in the symmetric case where both combs propagate through the sample, the intensity

$$I = E_1 \exp(-\alpha L/2) \times E_2^* \exp(-\alpha L/2) \equiv I_0 \times \exp(-\alpha L) \,, \tag{A6.4}$$

where $E_1 \times E_2^* = I_0$ is interpreted as the resulting intensity of the combined beams when no absorbing sample is present.

The above shows that the asymmetric case corresponds to a measurement where the absorption attenuates the intensity of the combined beams like the combined beams propagated through a sample of effective absorption path length of $L/2$. This means that the absorption peaks in the transmission spectra shown in Article IV (and in the transmission spectra shown in this thesis) appear approximately two times weaker than expected based on the true sample gas concentration and absorption path length. To yield transmission spectra where the absorption peak strengths would obey the Beer–Lambert law (1.1), the transmission spectra should be raised to the power of two.[190] Alternatively, as justified by Equation (A6.3), one could simply process the transmission spectra to the absorption spectra in the usual way by using the Beer–Lambert law (1.1), but consider the extra factor of two when eliminating the absorption path length to yield the absorption coefficient. Regarding the results of Article IV, the absorption line fitting was done for the transmission spectra (without raising them to the power of two). This does not affect the results or the conclusions in the article, apart from that the stated value for the acetylene concentration is two times lower than it should: the fitting routine used to get those results compensated the omitted factor of two by scaling the concentration instead of the absorption path length.

A6.3 Background correction

One of the simplest ways to consider a residual background that can emerge despite dividing a spectrum with absorption by a separately measured background spectrum is to include a polynomial to the fitting routine. However, because the fitted optical bandwidth in Article IV is quite large and the match between the acetylene and the background spectra is somewhat poor, a simple polynomial is not flexible enough. Inspired by the review of different background consideration approaches in [31] and the derivative approach in [191], I considered the residual background in Article IV in the following interesting way.

Figure 39 shows the raw transmission spectrum obtained by dividing the acetylene spectrum by the background spectrum (see Fig. 15). To consider the residual background, I first calculated the derivative of the experimental spectrum, shown in Figure 40. Then, I masked the absorption lines by fitting a HITRAN derivative spectrum (derived from a simulation using the HITRAN API[186,187]), and used the Whittaker smoother[120,192] on the residuals. Then I calculated the integral function of the Whittaker smoother. What remains is to determine a constant offset (the integration constant whose value is close to 1) that needs to be added to the result before dividing the raw transmission spectrum by the determined refined background. This offset was considered as part of the fitting routine. In addition to the offset, a constant frequency axis shift and the acetylene concentration was included into the fitting routine (the pressure was fixed to the experimental value of 300 mbar). The resulting refined background and the resulting final transmission spectrum are also shown in Figure 39.

The idea of this derivative approach is that due to the increased noise in the derivative spectrum and due to the masking of the absorption features, the Whittaker

smoother considers only slow variations in the spectrum that are mainly caused by the imperfect background correction. Indeed, as seen in Figure 39, the determined refined background is smooth and slowly varying and ignores the finer residual structure under the absorption peaks. On the other hand, the Whittaker smoother could have been used directly in the fitting routine without the derivative step, but the derivative approach seemed slightly less sensitive to the finer residual structure under the absorption peaks. I want to stress that using this kind of a smoother on the residuals is risky and calls for careful decision making from the user to reasonably tell apart the variation in the background that is due to imperfect background correction versus actual absorption signal, as also pointed out in [31]. Because, if one uses a smoother that is too flexible, it can smooth out the residual structure completely, which then basically would correspond to plotting the simulated spectrum one started with. It is left for the reader to decide whether they agree with me that the result shown in Figure 39 is justified.

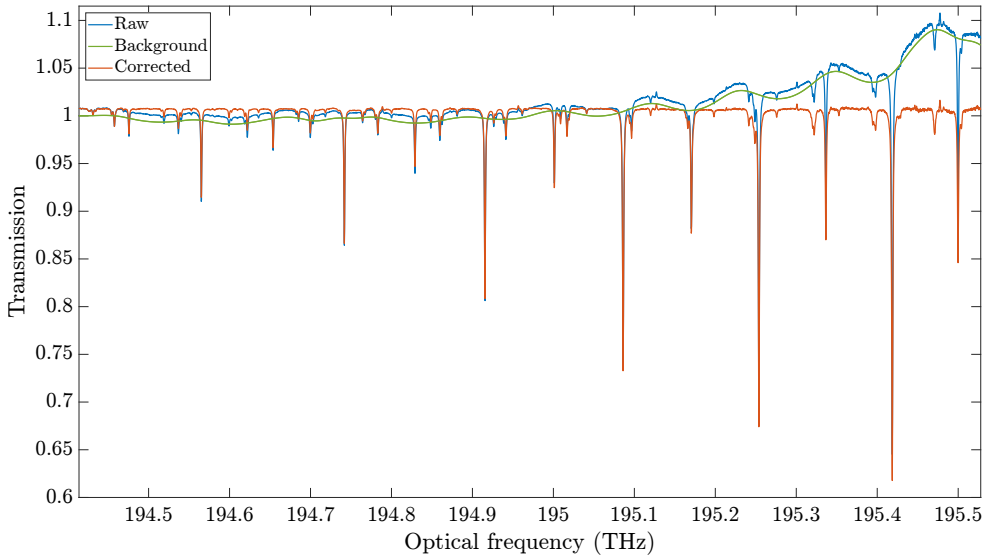

Figure 39: The raw transmission spectrum obtained by dividing the acetylene spectrum by the raw background spectrum, both shown in Fig. 15. The green trace is the refined background obtained using the derivative approach explained in the text. The orange trace is the final absorption spectrum obtained by dividing the raw transmission spectrum by the refined background.

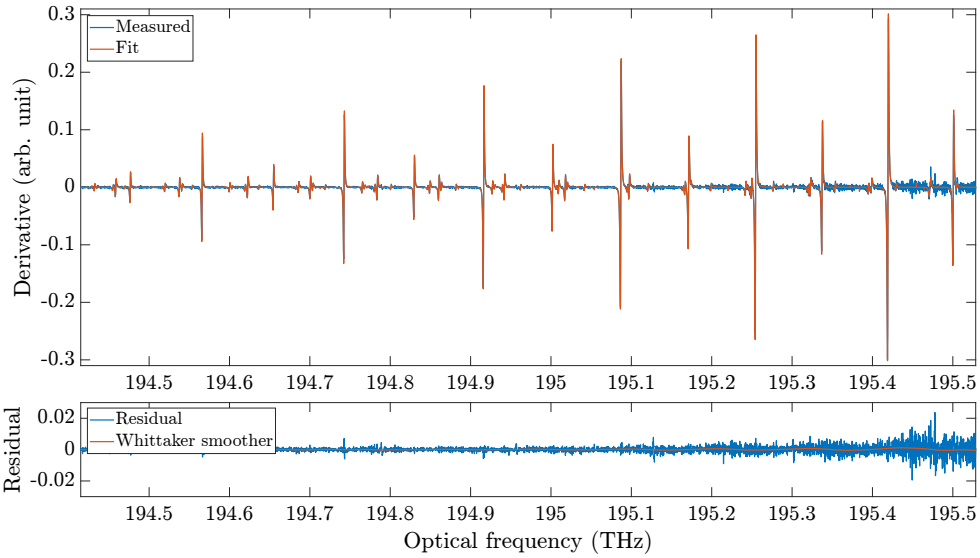

Figure 40: The derivative spectrum of the raw transmission spectrum in Fig. 39 together with a derivative HITRAN spectrum fit. The lower panel shows the fit residual, to which I have used the Whittaker smoother whose integral function results in the refined background shown in Fig. 39.

A7 Appendices to RD-FTS

A7.1 Laguerre–Gaussian modes

There are many mode families that describe electric fields carrying orbital angular momentum (OAM), such as the hypergeometric–Gaussian modes, Bessel–Gauss beams, Laguerre–Gaussian modes, and others.[193,194] Many of these mode families overlap in the sense that some of them are a special case of another in their definition. For example, all of the above-mentioned mode families can be defined as special cases of the more general "circular beams".[195] That said, one of the most used mode families to describe OAM beams is the Laguerre–Gaussian modes. These beams are defined according to Equation (A7.2), and are used in this thesis for the simulations presented in Section 5.

An electric field with an angular frequency ω and wavenumber k can be defined as

$$E(r,\theta,z,t) = E_0 u_p^{|l|} \mathrm{e}^{\mathrm{i}kz} \mathrm{e}^{-\mathrm{i}\omega t}\,, \tag{A7.1}$$

where the amplitude distribution function u in the case of a Laguerre-Gaussian mode is defined as[193,196]

$$u_p^{|l|}(r,\theta,z) = \frac{C_{|l|p}}{w(z)} \left(\frac{\sqrt{2}r}{w(z)}\right)^{|l|} L_p^{|l|}\left[\frac{2r^2}{w^2(z)}\right] \mathrm{e}^{-\frac{r^2}{w^2(z)}} \mathrm{e}^{-\mathrm{i}\frac{kr^2}{2R(z)}} \mathrm{e}^{\mathrm{i}l\theta} \mathrm{e}^{\mathrm{i}\psi(z)}\,, \tag{A7.2}$$

where $L_p^{|l|}[\cdots]$ is the generalized Laguerre polynomial,

$$C_{|l|p} = \sqrt{\frac{2p!}{\pi(p+|l|)!}} \tag{A7.3}$$

is a normalization constant*, and

$$\begin{cases} \psi(z) = (|l| + 2p + 1)\arctan(z/z_\mathrm{R}) \\ z_\mathrm{R} = \pi w_0^2/\lambda \\ w(z) = w_0\sqrt{1 + (z/z_\mathrm{R})^2} \\ R(z) = z\left(1 + (z_\mathrm{R}/z)^2\right) \end{cases}, \tag{A7.4}$$

where λ is the wavelength, and w_0 is the radius of the "underlying Gaussian" beam at focus. The integer l denotes the number of quanta of OAM that the beam carries via the factor $\exp(\mathrm{i}l\theta)$. The integer p governs the number of radial nodes.

To simplify Equation (A7.2), let's assume a beam at focus and a fundamental beam with no radial nodes (for which $L_0^{|l|}[\cdots] = 1$). Then,

$$u_0^{|l|}(r,\theta,0) = \frac{1}{w_0}\sqrt{\frac{2}{\pi}}\sqrt{\frac{1}{|l|!}}\left(\frac{\sqrt{2}r}{w_0}\right)^{|l|} \mathrm{e}^{-\frac{r^2}{w_0^2}} \mathrm{e}^{\mathrm{i}l\theta}, \tag{A7.5}$$

which yields the fundamental Gaussian mode when $l = 0$.

For the fundamental Gaussian beam, the beam diameter $2w_0$ is defined as the diameter of a circle where the intensity of the beam has declined to $1/\mathrm{e}^2$ from the maximum intensity at the beam center (Figure 41a); intensity is proportional to the absolute square of the electric field, as given by

$$I(r,\theta) = I_0 \frac{2}{w_0^2 \pi |l|!}\left(\frac{\sqrt{2}r}{w_0}\right)^{2|l|} \mathrm{e}^{-\frac{2r^2}{w_0^2}}, \tag{A7.6}$$

which describes the intensity of a Laguerre–Gaussian beam (with no radial nodes) at focus.

For an LG beam with $l \neq 0$, the beam diameter has to be defined in some other way than for the fundamental Gaussian beam. One way is to define the so-called inner and outer diameters where, similarly, the intensity drops to $1/\mathrm{e}^2$ from the maximum.[197] Another approach is to define the beam diameter (also for the Gaussian beam) via the standard deviation of the spatial distribution of the beam.[198] Both approaches can be used to define the beam divergence, which, like the beam size for a given underlying Gaussian diameter $2w_0$, increases as the topological charge l increases. One can also derive the so-called M^2 parameter, which is a convenient and often used way to describe the propagation of any beam whose divergence differs from the pure Gaussian case.[199]

Here, and in Article V, I define the beam diameter simply as the diameter of a circle that follows the intensity maximum of the beam. For an LG mode at focus and with $p = 0$, it is given by[198]

$$D_{|l|} = 2r(I_\mathrm{max}) = 2\sqrt{\frac{|l|}{2}}w_0\,. \tag{A7.7}$$

Figure 41 illustrates this diameter definition for a few different cases.

*Pay attention to the normalization constant. In some references it is written as $C_{|l|p} = \sqrt{2p!/\pi(p! + |l|!)}$, which I believe is a mistake.

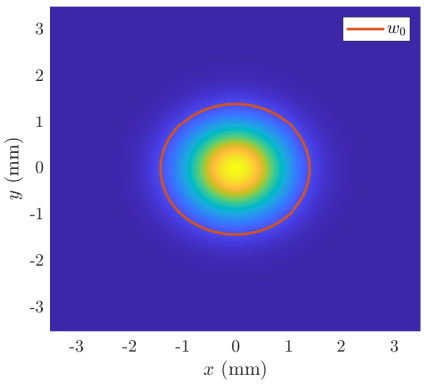

(a) Fundamental Gaussian beam.

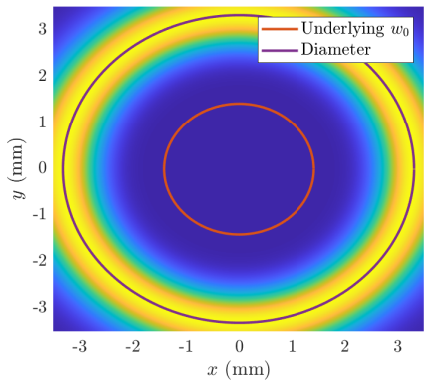

(b) LG10 beam with no radial nodes.

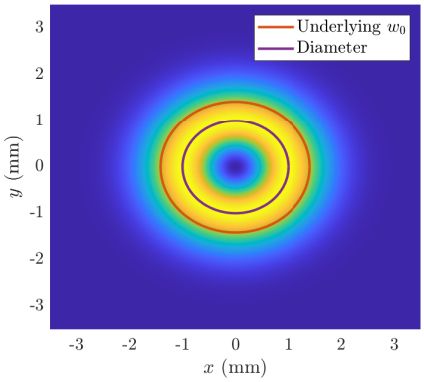

(c) LG1 beam with no radial nodes.

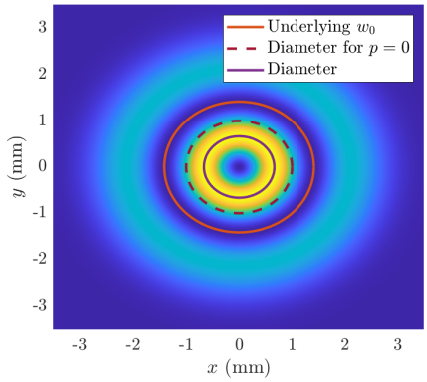

(d) LG1 beam with one radial node ($p = 1$).

Figure 41: Illustration of different Laguerre–Gaussian beams with 1.4 mm underlying Gaussian beam diameter. The beam diameter definition used in this thesis for the LG modes with $l \neq 0$ means the diameter of a circle that follows the intensity maximum of the beam. We can see that the beam diameter as defined here is affected by the topological charge and the number of radial nodes even if the underlying Gaussian waist remains the same.

Throughout this thesis and the simulations in Section 5, I always assume an LG mode with no radial nodes ($p = 0$), even though Figure 42 reveals that the experimental beams do not consist of the fundamental LG modes only. This is due to that the beams are prepared using spiral phase plates (SPPs). A spiral phase plate is an optical component whose thickness varies as a function of the azimuthal angle θ, such that after one whole cycle, the thickness has changed by Δl times the wavelength, thus modifying the phase of the input beam by $\exp(\mathrm{i}\Delta l\theta)$, *i.e.*, changing the OAM content of the incident beam by Δl. However, it has been shown that an SPP is not a pure mode converter between the Laguerre–Gaussian modes.[167] For example, for an input fundamental Gaussian beam and an SPP with $\Delta l = +1$, approximately 80 % of the intensity goes to the LG($l = 1$,$p = 0$) mode, and the rest to the higher order $l = 1$ modes that have radial nodes. In this thesis, I am more interested in trends and rules-of-thumb, for which reason the simulations ignore this detail: it is assumed that it is still the strongest intensity circle that dominates the generated signals so that the simulations that are based only on the fundamental LG beams provide accurate enough results as long as their diameters have been chosen as the experimental beam diameters.

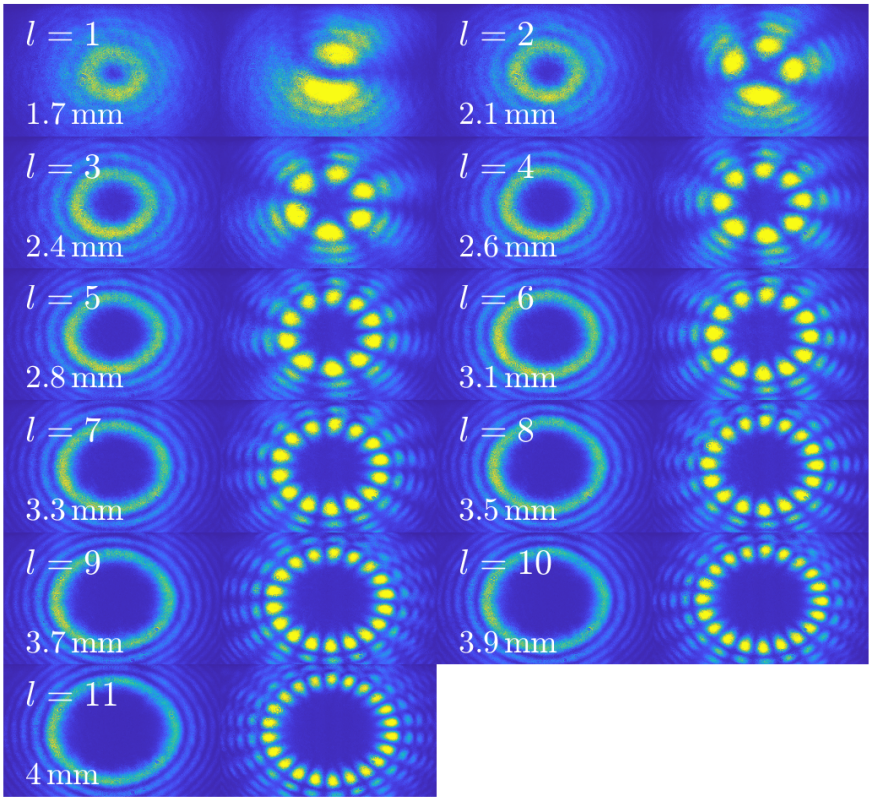

Figure 42: Experimental vortex beam intensity distributions and the corresponding interference petal patterns (from combining beams with the respective l and $-l$ topological charges) measured with an infrared camera. The white text indicates the experimental beam diameter value for each respective OAM mode.

In the experiment, a Gaussian beam with $2w_0 = 2.2\,\text{mm}$ was converted to different OAM-carrying beams with different combinations of SPPs placed in succession within a few centimeters from one another. We used a total of four plates with OAMs $l = 1, 1, 3, \text{and}\, 6$, generating OAM modes up to the topological charge $l = 11$. The chosen OAM-carrying beam then propagated approximately 92 cm before it hit the rotating target. Just before the rotating mirror, the beam diameters ranged from 1.7 mm (for the $l = 1$ mode) to 4 mm ($l = 11$). Figure 43 shows the experimentally determined beam diameters as a function of l in logarithmic scale. We see that the increase in the beam diameters follow reasonably well a linear trend. We can then estimate that if we had used an optical vortex comb spanning a total of 132 OAM modes (to measure the acetylene absorption feature in a single measurement), the largest beam diameter (for $l = 132$) would be 1.3 cm. This fact that the beam diameter increases as a function of the OAM mode may impose an additional practical limitation to the largest optical bandwidth that can be used, in addition to the limitations discussed in Section 5.3.

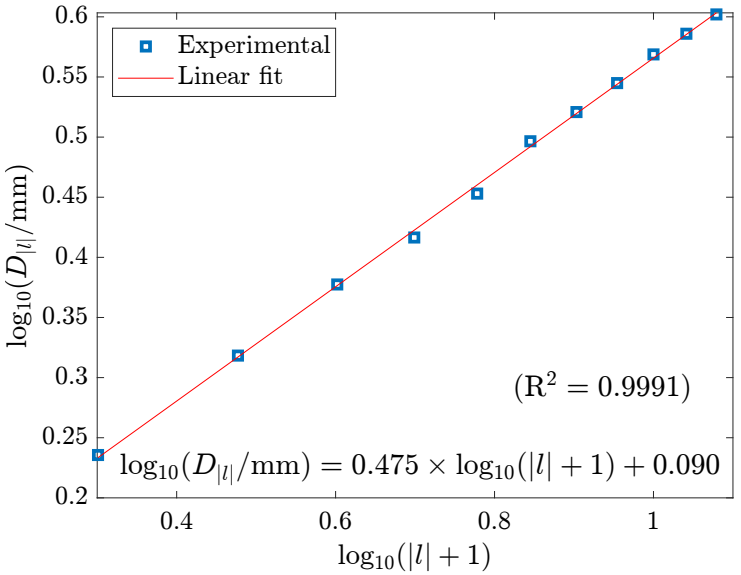

Figure 43: The experimental beam diameters in logarithmic scale, including a linear fit. This fit can be used to estimate the beam diameters if higher topological charge values were to be targeted. Note that the fit agrees reasonably well with the result that the divergence of a Laguerre–Gaussian beam (though with $p = 0$) is proportional to $\sqrt{|l|+1}$.[198]

A7.2 Modal decomposition

Here, I use Equations (5.3) and (5.4) to perform the modal decomposition analysis for the reflective rectangular target used in the experiments in Article V. A simulation of the target is shown in Figure 44a. Basically, I have simply written a matrix with elements with the value 1 at the rectangle and 0 elsewhere. Then, to perform the modal decomposition, I have calculated another matrix representing an LG mode with a chosen topological charge k and number of radial nodes p. I multiplied the target matrix in an element-wise manner with the element-wise complex conjugate of the LG matrix. Finally, I summed up all the elements in the resulting matrix to yield the complex amplitude $A_{k,p}$. I repeated this process for a few different k and p values, as seen in Figure 45. We can see that due to the 2-fold symmetry of the target, only the even-valued topological charges contribute to the target. The fundamental Gaussian mode dominates, but we also have respectable contribution from other topological charges, mostly with $p = 0$.

Note, however, that the modal decomposition of the target does not necessarily mean that the target would reflect only into these modes. Instead, Equation (5.7) shows that for an illumination mode, say, $l = +1$, the reflected field comprises modes $m = k-1$, which are odd (because k is known to be even); the reflected field contains mostly $m = -1$ ($k = 0$), which, interestingly, doesn't experience any rotational Doppler shift (see Eq. 5.7). To experimentally probe the modal composition of some target, one can either illuminate with a Gaussian beam ($l = 0$) and use a modal filter to detect one $m = k$ at a time, as is done in [159]. Or, one can use the fringe approach (Eq. 5.12) and illuminate with a beam with two input modes l_1 and l_2: while scanning the topological charge of one of the input modes, one can measure

the modal amplitudes by detecting reflection only to the fundamental mode $m = 0$ by using a modal filter such as a single mode fiber, as is done in [152].

Figures 44b and 44c show the reconstructed target based on the modal decomposition performed here. We can see that the shape of the real part of the reconstruction already resembles the original target, while the imaginary part tends to zero, as expected, because the original target is a real function (for a pure phase-modulator target, like the one in Appendix A7.3, the panels would be the other way around). To improve the reconstruction, more modes should be included in the decomposition calculations.

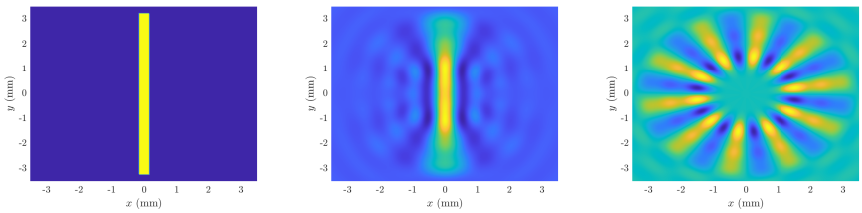

(a) Original target (b) Real part of reconstruction (c) Imaginary part of reconstruction

Figure 44: Reconstruction of a 0.3 mm wide reflective rectangle as a sum of the Laguerre–Gaussian modes spanning $l = -11, -10, ..., +11$ and $p = 0, ..., 1 ..., 10$, with weights whose absolute values squared are shown in Fig. 45.

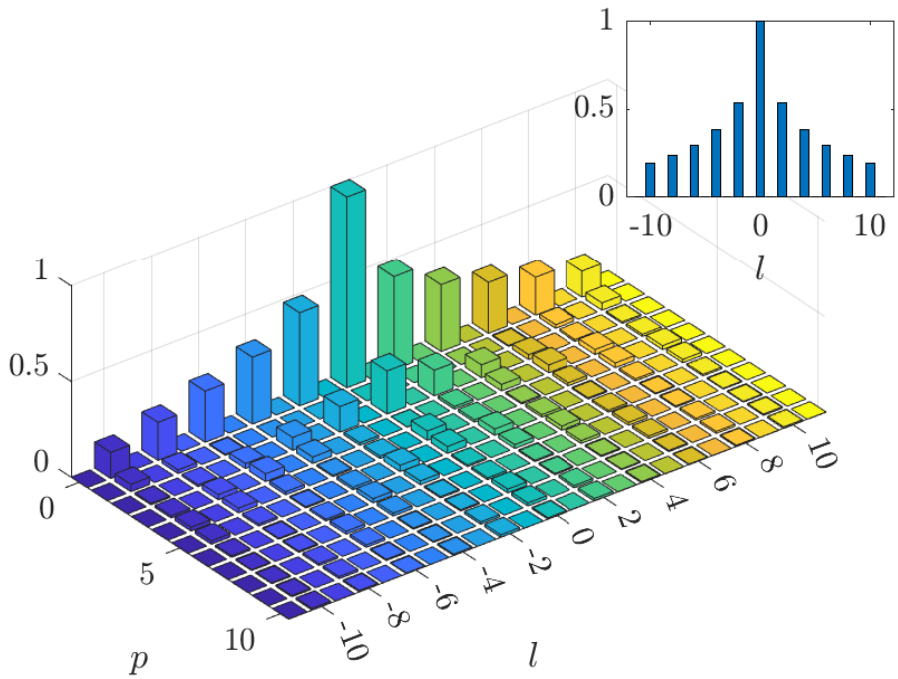

Figure 45: Modal decomposition of the reflective rectangular target given in Fig. 44a. The heights of the bars reflect the relative intensity of the respective Laguerre–Gaussian mode in the decomposition, obtained as the square modulus of the determined complex expansion coefficient and normalized by the largest such value. The inset shows the total contribution by a given topological charge l, obtained by summing along the respective p column. Due to the 2-fold rotational symmetry of the target, only the even-valued topological charges contribute.

A7.3 Phase modulation

In this thesis, and in Article V, I have mainly discussed the RD-FTS technique from the viewpoint of amplitude modulation, meaning that the rotating target modifies the reflectivity of the rotating mirror without modulating the phase (via varying the depth of the surface). In particular, all simulations in this thesis have illustrated amplitude modulation. For completeness, and because the results are interesting, I want here to show also an example of a target that modulates only the phase. Similar to Animation 1d, let's use a rectangular target. In Animation 1d, the reflectivity of the rectangle is 0, but 1 elsewhere. Here, let's have the values at the rectangle to be $\exp(\mathrm{i}\phi)$, but 1 elsewhere. This means that the rectangle will reflect the incident beam but simultaneously advance its phase by ϕ. Otherwise, the simulations have been performed similarly as explained in Section 5.3. The main difference is that only one of the beams strike the rotating target, after which the reflected field is beat against a reference beam:

$$I(t,l) = \int_{-a}^{a}\int_{-b}^{b} \left|\mathrm{LG}(l,p=0) \times R(t) + \mathrm{LG}(-l,p=0)\right|^2 \mathrm{d}x\mathrm{d}y\,, \tag{A7.8}$$

where the symbols have been explained when explaining Equation (5.14).

The result of this simulation is shown in Animation 3. In 3a, the input field consists of the OAM mode $l_1 = +2$, and the reference mode is $l_2 = -2$, meaning that the modes have opposite signs.* In 3b, the modes have the same sign. In the former case, intensity modulation at an angular frequency of $2l\Omega$ ensues. In the latter case, no change in the average intensity at the detector would be observed even though the pattern rotates. This exemplifies that even in the heterodyne case, the combined beams need to generate a petal pattern that the rotating target then traverses, as was claimed in Section 5.1.

Another way to view this result is that in the case of Animation 3a, the reference mode l_2 probes light reflected to this specific mode by the rotating target, with the strongest possible intensity modulation signal obtained by a rotating pure mode converter to this specific mode (such as a suitable rotating spiral phase plate). In the case of 3b, the reference mode probes light unaffected by the rotating target; a pure "mode converter" to this mode would be a rotating perfect mirror that consequently wouldn't modulate the phase of the incoming beam and therefore wouldn't lead to a rotational Doppler frequency shift.

*Strictly speaking, the simulations here describe transmission, which means that the topological charges of the incident beams need to have opposite signs (or generally be unequal). In Section 5.1, the derivations describe reflection from a rotating target. In that framework, the incident beams need to have the same topological charges so that the combined beams will form the petal pattern as the reflection at the rotating mirror flips the phase of the other beam.

(a) Reference and reflected beams have opposite topological charges, which creates a petal pattern that the rotating target traverses, leading to intensity modulation.

(b) Reference and reflected beams have the same topological charges. In this case, no intensity modulation is observed.

Animation 3: Simulation of a phase-modulating rectangular target with a phase value of $\phi = \pi/2$.

A7.4 Broadband simulation

In Supplement 1 of Article V it was derived that when an electric field consisting of two optical angular frequencies ω_1 and ω_2 with the topological charges l_1 and l_2, respectively, is incident on a rotating target, one can expect intensity modulation at the down-converted frequencies $2l_1\Omega$ and $2l_2\Omega$, where Ω is the angular frequency of the rotating target. In addition, peaks are expected around the difference frequency of the two optical frequencies, *i.e.*, at $\Delta\omega \pm [l_1 - l_2]\Omega$ and at $\Delta\omega \pm [l_1 + l_2]\Omega$. However, these latter peaks around $\Delta\omega$ are not always present, which seems to depend on the symmetry of the rotating target. Animation 4 shows two types of targets: a short rectangle (4a) and a long rectangle (4b).

To simulate the generated modulation signals for the targets in Animation 4, I calculate

$$I(t,l,D_{|l|}) = \int_{-a}^{a}\int_{-b}^{b} \mathrm{d}x\mathrm{d}y \left| \sum_l [\mathrm{LG}(l,p=0) + \mathrm{LG}(-l,p=0)] \times \exp(-2\pi\nu_l t) \times R(t) \right|^2 , \quad \text{(A7.9)}$$

where explicitly writing out $\exp(-2\pi\nu_l t)$ emphasises that each of the OAM modes l are carried by different optical frequencies. Rest of the symbols have been explained when explaining Equation (5.14).

Figure 46 shows both the resulting time domain signal (interferogram) and the corresponding spectrum for a simulation with two input modes $l_1 = 1$ and $l_2 = 2$, with 1 Hz rotational frequency of the target, and with an "optical" frequency difference of 100 Hz. We see that in the case of a short rectangle, all the expected frequency components at 2 Hz and 4 Hz, but also at $\Delta\omega/(2\pi) \pm [l_1 - l_2]\Omega/(2\pi) = 100 \pm 1$ Hz and $\Delta\omega/(2\pi) \pm [l_1 + l_2]\Omega/(2\pi) = 100 \pm 3$ Hz, are present. However, in the case of the long rectangle, only the frequencies at 2 Hz and 4 Hz are present. It must be that in the

case of the long rectangle (two short rectangles with π angular distance), two signals are generated such that they sum up out of phase, eliminating the signals around the optical difference frequencies. This probably could be derived analytically in a similar manner as is done in [151], but it is out of scope for the present thesis.

(a) A long rectangular target. (b) A short rectangular target

Animation 4: Simulation with two types of targets for an input field consisting of two distinct optical frequencies carrying respective topological charges $l = 1$ and $l = 2$. Note the oscillatory motion of the underlying intensity pattern, which is due to beating between the different optical frequencies in the field.*

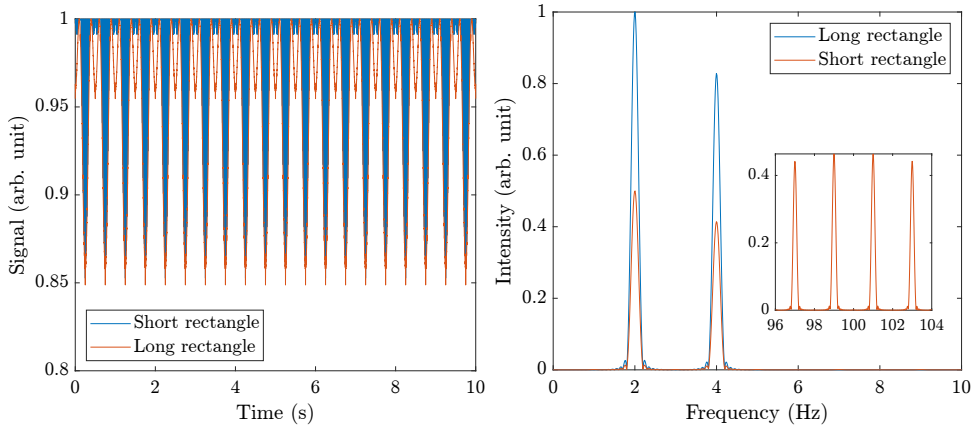

(a) The interferograms. (b) The corresponding spectra.

Figure 46: Results for the simulation in Animation 4. It can be seen that for the long rectangle case, the only peaks generated are the ones at 2 and 4 Hz. For the short rectangle case, also the peaks around 100 Hz appear.

*The intensity of the incident electric field (before it impinges on the rotating target)

$$E(r,\theta,t) = B_1(r)\exp(-\mathrm{i}\omega_1 t)\left[\exp(\mathrm{i}l_1\theta) + \exp(-\mathrm{i}l_1\theta)\right] + B_2(r)\exp(-\mathrm{i}\omega_2 t)\left[\exp(\mathrm{i}l_2\theta) + \exp(-\mathrm{i}l_2\theta)\right]$$

can be derived to be

$$\begin{aligned} I(r,\theta,t) = {} & 2|B_1(r)|^2 + 2|B_2(r)|^2 + 2|B_1(r)|^2\cos(2l_1\theta) + 2|B_2(r)|^2\cos(2l_2\theta) \\ & + 2|B_1(r)B_2(r)|\cos(\Delta\omega t + [l_2 - l_1]\theta) + 2|B_1(r)B_2(r)|\cos(-\Delta\omega t + [l_2 - l_1]\theta) \\ & + 2|B_1(r)B_2(r)|\cos(\Delta\omega t + [l_2 + l_1]\theta) + 2|B_1(r)B_2(r)|\cos(-\Delta\omega t + [l_2 + l_1]\theta)\,. \end{aligned}$$

From this we see that the intensity pattern consists of two pairs of counter-rotating petal patterns, leading to the oscillatory motion seen in the animation.

To consider an even more complex case, let's use a total of 11 OAM modes but with the 5th mode excluded, and let's again use a long rectangular target (Animation 5). Figure 47 shows the results for this simulation. One can see the expected result that peaks appear at the down-converted frequencies $2lf_{\mathrm{rot}} = (2, ..., 4, ..., 8, 12, ..., 22)$ Hz, *i.e.*, that the peak at 10 Hz is absent as the OAM mode $l = 5$ is not present. In addition, the peaks around the "optical" frequency separation of 100 Hz are absent due to the even symmetry of the target. Instead, additional signals appear around the even multiples of the optical frequency difference, such as around 200 Hz (with further peaks appearing also around 400 Hz, 800 Hz, ..., which is not illustrated in the figure).

All in all, the broadband simulations presented here further validate that the RD-FTS technique should work also when using an actual broadband optical vortex comb light source (in addition to the emulated one in Article V). I am excited for an experimental verification of this.

Animation 5: Simulation of a rectangular target rotating in an optical field consisting of 11 OAM modes (and their mode inverted counterparts), each carried by a unique optical frequency. The field itself oscillates due to beating between the different optical frequencies.

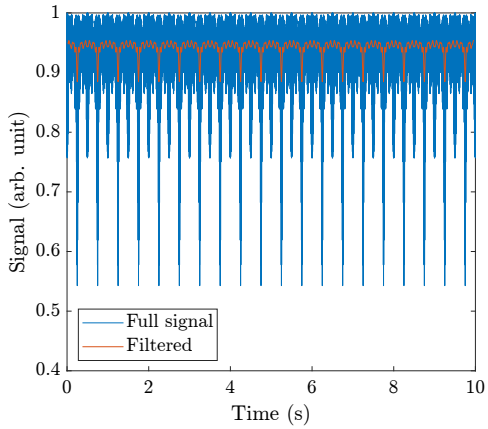

(a) The time domain signal (interferogram). The orange curve is the same as blue, but the frequencies above 100 Hz have been filtered out.

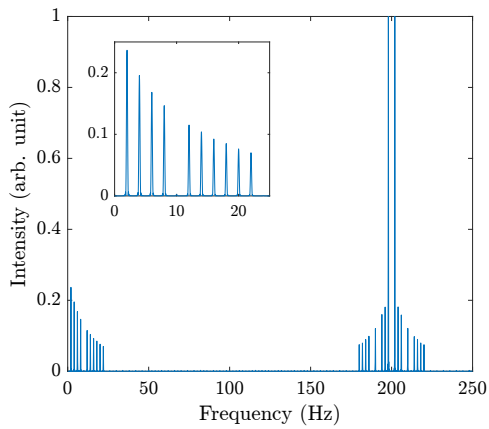

(b) The corresponding spectrum (Fourier transform) of the blue trace in (a). We see that the peak at 10 Hz (corresponding to $l = 5$) is not present, as expected. We also see that the additional peaks around the "optical" frequency difference (100 Hz) are absent while they appear around the even multiples of 100 Hz due to the 2-fold symmetry of the target.

Figure 47: Interferogram and the corresponding spectrum from the broadband simulation in Animation 5.